The Dissertation Committee for Hua Gu
certifies that this is the approved version of the following dissertation:

Numerical Modeling of Flow around Ducted Propellers

Committee:

Spyros A. Kinnas, Supervisor

Howard M. Liljestrand

Ronald L. Panton

Ben R. Hodges

David B. Goldstein

Hanseong Lee

Numerical Modeling of Flow around Ducted Propellers

by

Hua Gu, B.S.; M.S.

Dissertation

Presented to the Faculty of the Graduate School of

The University of Texas at Austin

in Partial Fulfillment

of the Requirements

for the Degree of

Doctor of Philosophy

The University of Texas at Austin
August 2006

To my parents, wife and unborn baby

Acknowledgments

The past six years at the University of Texas at Austin are filled with mixed memories of the sweetness of achievements and bitterness of frustrations during the academic study. It has been an exciting and challenging period and has definitely taught me how to face the difficulties in life.

First of all, I want to express sincere gratitude to my advisor, Professor Spyros A. Kinnas, for his continuous advise and insightful comments during the entire period of my research. Without his support and faith, I would not have the chance to pursue my doctoral program in the United States. I also admire his patience, inspiration and advice in both my academic and personal life.

I have had the honor of having committee members from diverse backgrounds. I would like to thank Professor Ronald L. Panton, Professor Howard M. Liljestrand, Professor Ben R. Hodges and Professor David B Goldstein, for the passing on knowledge and expertise in their respective fields to me during classes and committee meetings. Discussion with them and their inputs have helped me refine my work. I am also in debt of Dr. Hanseong Lee, for his expert and valuable advice during the course of research, and for passing on his knowledge and wisdom on life.

I would like to thank my former supervisor at the Huazhong University of Science and Technology, Professor Guangwu Zeng for his encouragement to pursue higher studies abroad and for his kind help both in my academic and personal life.

I would also express my thanks for the staff and fellows in the Computational Hydrodynamics Laboratory (CHL) and the Offshore Technology Research Center (OTRC), for the joy and knowledge they brought me. I would especially thank Hong Sun and Vimal Vinayan, for their kind help in proofreading my writing.

Finally, I would like to thank my family members. I am in debts of my parents – Jinlin Gu and Jifang Yuan. Without their love, support and encourage, everything now is impossible. I also owe much to my wife, Lei Chen. Her love and sacrifice are the power to push me forward. I would also thanks my unborn baby, your arrival is the surprising gift in my life. I am also very grateful to my relatives and friends for the happiness and support they bring.

This research was supported by Phase III/IV of the "*University/Navy/Industry Consortium on Cavitation Performance of High Speed Propulsors*" with the following members: AB Volvo Penta, Sweden, American Bureau of Shipping, USA, Daewoo Shipbuilding and Marine Engineering Co. Ltd., Korea, Kawasaki Heavy Industries Ltd., Japan, Michigan Wheel Corporation, USA, Naval Surface Warfare Center Carderock Division and Office of Naval Research (contracts N00014-01-1-0225 and N00014-04-1-0287), USA, Rolls-Royce Marine AS, Norway, Rolls-Royce Marine AB, Sweden, VA Tech Escher Wyss GMBH, Germany, Wärtsilä Propulsion AS, Norway, Wärtsilä Propulsion BV, The Netherlands and Wärtsilä Propulsion CME, Zhenjiang Propeller Co. Ltd., P. R. China. Partial support of this work was also provided by Office of Naval Research under the NNRI program,

through Florida Atlantic University (TRD67). I enjoyed all those productive consortium meetings I had together with the representatives from above institutions. I want to thank to each of them for their interests on my research and their feedback from industries points of view.

Numerical Modeling of Flow around Ducted Propellers

Publication No. ____________________

Hua Gu, Ph.D.
The University of Texas at Austin, 2006

Supervisor: Spyros A. Kinnas

An iterative method, coupling a vortex lattice method (VLM) based potential solver and a finite volume method (FVM) based Euler solver, is used to model the flow around ducted propellers. The VLM is applied to the blade inside the duct, solves for the potential flow in the vicinity of the blade and predicts the pressures, forces, moments and cavity patterns. The FVM is applied to the whole fluid domain with the duct. The Euler equations are solved with the pressure difference across the blades being converted into body force terms and the duct being modeled as solid wall boundaries. The effective velocities are then evaluated by subtracting the induced velocities from the total velocities. The VLM is applied again with the updated effective velocities and the iteration between VLM and FVM continues until the thrust and torque converge. The interaction between duct and propeller is included with such an iterative procedure. Some special treatments on the ducted propeller are presented. A simplified image model is applied to account for the nonaxisymmetric duct wall effects. A gap model, based on an orifice equation, is implemented to predict the influence of the viscous gap region on the overall performance of ducted propellers. A computational viscous model is used to assess the discharge coefficient in the current method. Some approaches to predict the effective velocities with accuracy are discussed. Systematic validations for the current method with other numerical methods and experiments are given.

Finally an approach to model the tip leakage vortex is presented. The tip leakage vortices are aligned via a free wake relaxation method. Convergence and parameter studies are given for this model.

Table of Contents

List of Tables

List of Figures

Nomenclature

Latin Symbols

A	influence coefficient sub-matrix
A	area of obstruction throat (dimensional)
$\hat{A}_c$	area of the mean camber surface contained in GBFLOW cell
A'	expanded influence coefficient matrix
B	influence coefficient sub-matrix
$\vec{B}$	vector potential
C	influence coefficient sub-matrix
$C_{f,num}$	numerical friction coefficient
c	artificial speed of sound
c	chord length of 3-D foil section (dimensional)
C_p	pressure coefficient,
	$C_p = (P - P_o)/(0.5\rho n^2 D^2)$ for propeller
C_Q	discharge coefficient
D	influence coefficient sub-matrix
D	propeller diameter, $D = 2R$ (dimensional)
D	duct diameter (dimensional)
d	obstruction diameter (dimensional)
d_n, d_r	displacement in normal, radial direction for roll up point
F	function defined as difference between ψ and g
$\vec{F}$	column matrix for the x derivative terms

F_n	Froude number based on n, $F_n = n^2 D/g$
$\bar{F}_x$	integrated pressure force on duct in x direction
$\vec{f}$	body force vector
f	camber
f_{max}	maximum camber (dimensional)
$\vec{f_{3d}}$	3D body force vector
$\vec{G}$	column matrix for the y or r derivative terms
g	gravitational acceleration (dimensional)
g	ψ coordinate of the cavity surface
$\vec{H}$	column matrix for the z derivative terms
h	height of 2D gap (dimensional)
J_s	advance ratio, $J_s = U_\infty/nD$
K_Q	torque coefficient, $K_Q = Q/\rho n^2 D^5$
K_T	thrust coefficient, $K_T = T/\rho n^2 D^4$
K_{TP}	propeller thrust coefficient, $K_{TP} = T/\rho n^2 D^4$
K_{TD}	thrust coefficient on duct
	$K_{TD} = T_D/\rho n^2 D^4$
$K_{TD,fr}$	axial direction friction force on duct
K_{TT}	total thrust coefficient on ducted propeller,
	$K_{TT} = K_{TP} + K_{TD} - K_{Td,fr}$
N	circumferential point numbers
N_K	circumferential cell number
n	propeller rotational frequency (rev/s) (dimensional)
$\vec{n}$	unit normal vector
P	pressure

$\tilde{p}$	pressure (dimensional)
P/D	pitch ratio
P_o	far upstream pressure, at the propeller axis (dimensional)
P_v	vapor pressure of water (dimensional)
P_e	nondimensional effective pressure
P_{eff}	effective pressure
r	radial coordinate
$\vec{q_E}$	effective velocity vector of propeller in ship fixed system
$\vec{q_e}$	effective velocity vector of propeller in propeller fixed system
$\vec{q_i}$	irrotational velocity vector
$\vec{q_p}$	induced velocity vector of propeller
$\vec{q_r}$	rotational velocity vector
$\vec{q_t}$	total velocity vector
$\vec{Q}$	column matrix containing the source terms
Q	flow rate (dimensional)
$\tilde{\vec{Q}}$	dimensional source term
Q_B	strength of blade source
Q_C	strength of cavity source
$\vec{q}_{ind}$	induced velocity at tip leakage vortex vertices
R	propeller radius (dimensional)
R	vector of known normal velocity due to thickness and inflow
R	ratio between flow rate and pressure difference
R'	expanded RHS
$\vec{R}$	residual

Re	Reynolds number based on inflow and foil chord length $Re = \frac{\tilde{U}c}{\nu}$
R_{gap}	vector of right hand side of orifice equation
R_B	radial location of vortex
R_{B_i}	radial location of image vortex
R_d	duct radius
R_h	hub radius
r_i	distance between control point and vertex of cell
r_i	radius of duct inner surface
r_o	radius of duct outer surface
S	arclength
$\bar{S}$	area of duct surface
$S_{i,j}$	area of cell i, j
$\vec{U}$	column matrix for the time derivative terms
$\tilde{U}$	inflow velocity (dimensional)
u_x	axial velocity
u_r	radial velocity
u_θ	tangential velocity
$u*$	interpolated velocity at blade control point
$\vec{V}$	resultant velocity
$\vec{V_B}$	induced velocity by blade thickness sources
$\vec{V_\Gamma}$	induced velocity by line vortices on blade and wake
$\vec{v_\gamma}$	induced velocity by a horseshoe loop with unit strength
$\vec{V_I}$	inflow velocity
$\vec{V_O}$	induced velocity by other blades

$\vec{V_Q}$	induced velocity by cavity sources
$\hat{\mathcal{V}}_c$	cell volume
t	time
t	thickness (dimensional)
U_∞	velocity at infinity or ship speed (dimensional)
U_τ	frictional velocity near wall
X_B	axial location of vortex
X_{B_i}	axial location of image vortex
$\vec{x}$	=(x, y, z) or (x, r, θ), location vector
x_{cut}	cut location
x_{prop}	propeller location
$(x_{prop}, y_{prop}, z_{prop})$	coordinates in propeller fixed system
$(x_{ship}, y_{ship}, z_{ship})$	coordinates in ship fixed system
$\vec{x_u}$	a unit vector in axial direction
y^+	y coordinate scaled by ν/U_τ, a near wall flow scale
Z	number of blades

Greek Symbols

α	angle of attack for duct section
α_r	inflow angle
β	artificial compressibility
β	obstruction ratio
ΔC_p	difference of pressure coefficient across the gap
Δp	pressure difference across the gap
$\Delta \hat{p}$	pressure difference across the blade surface
Δx_e	difference in the x coordinates for e edge
Δr_e	difference in the r coordinates for e edge
δ_{ii}	second finite central difference in i-direction
δ_{iiii}	fourth finite central difference in i-direction
δt	time step size
$\delta\theta$	angular increment of wake sheet.
Γ	circulation on blade $\Gamma = \frac{\tilde{\Gamma}}{2\pi R V_s}$
Γ_f	circulation around 3D foil $\Gamma = \frac{\tilde{\Gamma}}{U_\infty c}$
$\tilde{\Gamma}$	circulation (dimensional)
Γ	vector of unknown strength
Γ'	expanded vector of unknown strength
Γ_{gap}	vector of unknown gap vortex strength
γ	strength of line vortices
μ_2	the second order artificial viscosity
μ_4	the fourth order artificial viscosity

ω	angular velocity of propeller rotation
ν	kinematic viscosity
ϕ	velocity potential
ϕ_p	perturbation potential
ϕ_Γ	induced potential by vortex horseshoe with unit strength
ϕ_{Q_B}	induced potential by blade source with unit strength
ϕ_{Q_C}	induced potential by cavity source with unit strength
ψ	hight of the cavity

q_r	relative flow to the gap
q_t	the total velocity at tip leakage vortex vertex
ρ	density of fluid (dimensional)
σ_2	the second order artificial viscosity coefficient
σ_4	the fourth order artificial viscosity coefficient
σ_n	cavitation number based on n, $\sigma_n = (P_o - P_c)/(0.5\rho n^2 D^2)$
σ_v	cavitation number based on $\tilde{U}$, $\sigma = (P_o - P_c)/(0.5\rho\tilde{U}^2)$
$\xi,\ \eta,\ \zeta$	curvilnear coordinate in computational domain

Superscripts

A, B, C, D	cell indices
(i, j, k)	node or cell indices in i, j, k direction
N, W, S, E	edge indices in north, west, south, east of a cell
$n, n+1$	time step indices
$-$	nondimensional variables
$\hat{}$	dimensional variables

Acronyms

BEM	Boundary Element Method
CFD	Computational Fluid Dynamics
DTMB	David Taylor Model Basin
DBC	Dynamical Boundary Condition
FVM	Finite Volume Method
KBC	Kinematic Boundary Condition
ITTC	International Towing Tank Conference
LE	Leading Edge
MIT	Massachusetts Institute of Technology
NSMB	Netherlands Ship Model Basin
PRESTO!	PREssure STaggering Option
PISO	Pressure-Implicit with Splitting Operators
QUICK	Quadratic Upwind Interpolation for Convective Kinematics
RANS	Reynolds Average Navier-Stokes equations
NACA	National Advisory Committee for Aeronautics

SIMPLE	Semi-Implicit Method for Pressure Linked Equation
VLM	Vortex-Lattice Method
DNS	Direct Numerical Simulation

Computer Program Names

$FLUENT$	commercial CFD code
MPUF-3A	cavitating propeller potential flow solver (VLM)
PROPCAV	cavitating propeller potential flow solver (BEM)
GBFLOW3X	Axisymmetric effective wake solver (FVM)
GBFLOW3D	3D effective wake solver (FVM)
U^2NCLE	CFD code developed by the Mississippi State University

Chapter 1

Introduction

1.1 Background

Ducted propellers have been widely used for marine applications. The earliest practical ducted propeller appeared in the experiment conduced by Luisa Stipa and Kort in early 1930s (Carlton [1994]). After that, ducted propellers were first applied in heavily loaded boats, such as tugs, push-boats and trawlers. Nowadays, the applications can be widely seen in commercial ships such as large tankers and bulk carriers, as well as in the dynamic positioning systems of offshore platforms or vessels.

A ducted propeller for a commercial ship is shown in Figure 1.1. Such a typical ducted propeller configuration consists of an annular duct that normally has an airfoil cross section surrounding a propeller. With different section forms, the duct can be classified as an accelerating or a decelerating type. As shown in Figure 1.2, an accelerating duct has a smaller radius at the propeller plane compared to the radius at the leading edge whereas a decelerating type duct has the opposite arrangement.

The wide application of ducted propeller comes from their significant advantages relative to open propellers.

Figure 1.1: Geometry of a ducted propeller in practice. Taken from www.becker-marine-system.com.

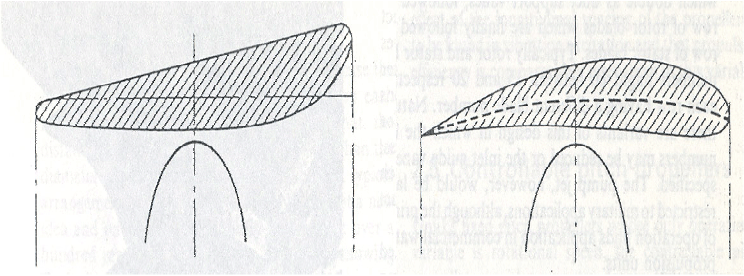

Figure 1.2: Typical section for accelerating duct (left) and decelerating duct (right). Taken from Carlton [1994].

- An accelerating ducted propeller remarkably increases the lifespan and efficiency for propellers with high loadings. The presence of the duct allows the redistribution of the mean lifting forces between the propeller and the duct. An accelerating duct can provide up to 50% of the propeller's thrust at bollard pull condition (zero ship speed). The re-distribution of thrust between duct and propeller lowers the loading requirements for the propeller and engines, thus extends their lifespan and lowers maintenance requirements. At the same time, the part of the shedding vortices, which would shed into the wake if duct is absent, now becomes attached vortices on the duct. The energy loss is therefore decreased, providing that the loss due to friction on the duct is less than the the gain from the reattchment of shedding vortices. Since higher energy loss occurs when propeller loading is high, the application of accelerating ducted propellers in high loading situation will provide more gains in efficiency, as shown in Figure 1.3.

- The decelerating ducted propellers are applied to high speed vehicles to address cavitation problems and resulting side effects. Cavitation is the forma-

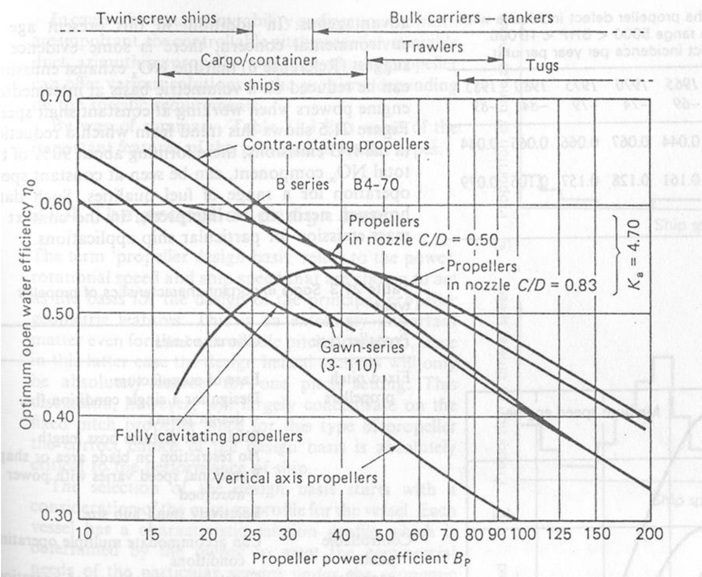

Figure 1.3: Open water efficiency for different propellers. Taken from Manen [1966].

tion of partial vacuum in liquid due to the pressure drop caused by swift body motion. These cavities collapse when moving downstream where pressure is recovered. The collapse of bubbles comes together with shock waves, which are the primary causes of noise, surface erosion and trailing edge curl. These cavitation-induced damages can affect the efficiency of the propeller and the maneuverability. Decelerating ducts can increase the pressure inside the duct, and delay or even avoid the inception of cavitation.

- Besides the respective advantages for accelerating and decelerating ducted propellers, they have the common advantages as follows: better control over the inflow to the propeller; improvement of maneuverability and position-keeping ability; protection from damage to the propellers.

1.2 Motivation

The advantages of ducted propellers over open propellers come from the duct surrounding the propeller. However, the following difficulties are faced in the modeling of a ducted propeller.

- The interaction between the propeller and the duct brings more difficulties in evaluating the effective velocity of the ducted propeller. As shown in Figure 1.4, the effective velocity includes the nominal velocity and the interaction velocity. The nominal velocity is the velocity at the propeller plane when the propeller is absent. It contains strong vortices shed from the hull boundary layers, and can be estimated from either model tests (with scale factors) or computational solutions such as Navier-Stokes solvers. The interaction velocity requires dynamics of vorticity to solve the interaction of propeller with inflow vorticity and the duct, which is beyond the capabilities of potential methods. In the work of Choi [2000], the effective velocity in front of an open propeller could be solved by subtracting the propeller induced velocity from the total velocity, as shown in Figure 1.4. The effective velocity before a ducted propeller can also be solved in this way.

- The second difficulty comes from the small clearance between the duct inner surface and the blade tip. This region is viscous dominant and the flow is very complex. To solve the flow region is a heavy computational burden for a viscous solver, since a lot of cells are needed in the gap region to capture the tip leakage vortex core. In our approach, we will look for a way to predict the

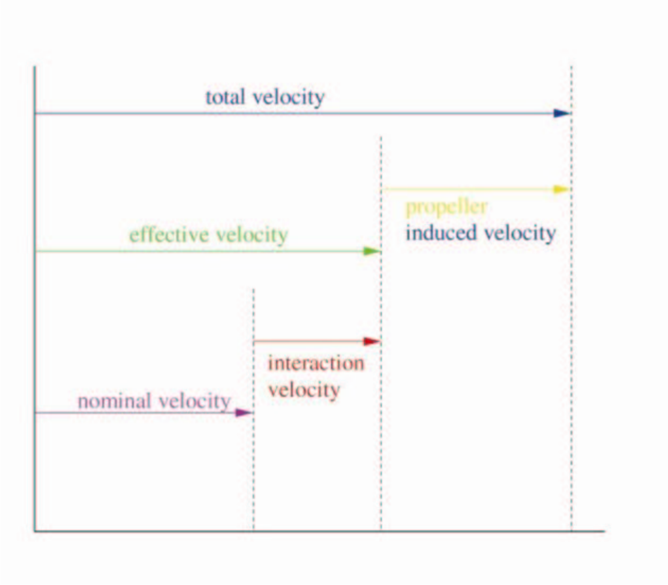

Figure 1.4: Decomposition of the wake field for a propeller. Taken from Carlton [1994].

overall influence of the gap region on the propeller performance rather than solve the detailed flow inside the gap.

The motivation of this research is to develop a robust, reliable and computational efficient tool to predict the correct hydrodynamic performance of ducted propellers, with focus on the accurate effective velocity prediction and gap effects.

1.3 Objectives

The objective of this research is to extend the coupling of a vortex lattice method and an axisymmetric/3-D Euler solver to solve the flow around the ducted propeller and predict the forces, moments and cavitation of the propeller, and pressures and forces on the duct.

1.4 Overview of Dissertation

The contents of the remaining chapters are as follows:

- Chapter 2 presents a literature review of previous work on numerical modeling of ducted propellers. A brief review of the vortex lattice method, which is used to predict the potential flow in the vicinity of propeller is also given. Efforts to determine effective velocity for open propellers are also reviewed.

- Chapter 3 describes the present method to predict the flow around ducted propellers. Formulation of the Axisymmetric/3D versions of the Euler solver are given. Approaches for determining the effective velocity of ducted propellers and interactions are introduced. Grid, boundary conditions and body forces for ducted propellers are presented.

- Chapter 4 presents the gap model, which is used to account for the viscous dominant flow inside the gap between propeller tip and duct inner surface.

- Chapter 5 presents some improvements to evaluate the effective velocities for a ducted propeller. An effective pressure term is also introduced to satisfy the Bernoulli equation.

- Chapter 6 presents validation of the current method with other numerical methods.

- Chapter 7 presents validation of the current method with experiments.

- Chapter 8 presents the tip leakage vortex model to account for the increase in loading at the tip of ducted propeller.
- Chapter 9 presents a summary and conclusions. Recommendations for future work are also given

Chapter 2

Literature Review

In this chapter, a vortex lattice method, which is used to solve the potential flows around propellers, is reviewed first. Then the efforts by different research groups on effective velocity evaluation are summarized. After that, previous studies on ducted propeller analysis are reviewed. Finally, the uniqueness of current work is summarized.

2.1 Vortex Lattice Method for Propeller Potential Flow

The vortex lattice method (VLM) is classified as a lifting surface method. The major characteristic of this method is that the singularities (vortices and sources) are distributed on the mean camber surface.

VLM has been applied widely in the numerical modeling of wing sections and was introduced for the analysis of fully wetted propeller flows by Kerwin and Lee [1978]. The method was later extended to treat unsteady sheet cavitating propeller flows by Lee [1979] and Breslin et al. [1982]. A robust arrangement of singularities and control point spacing was employed in VLM to produce accurate results by Kinnas and Fine [1989]. In Kinnas [1991], a leading edge correction was introduced to account for the defect of linear cavity solution near a round leading edge, and was incorporated into a code named PUF-3A. The method was then extended to treat super-cavitating propellers subject to steady flow by Kudo and Kinnas [1995]. Most recently, the method has been re-named MPUF-3A for its additional ability to search for mid-chord cavitation by Kinnas et al. [1998]. The latest version of MPUF-3A also includes wake alignment in circumferentially averaged inflow by Greeley and Kerwin [1982], the non-linear thickness-loading coupling by Kinnas [1992], the effect of hub and wake alignment including the effect of shaft inclination by Kinnas and Pyo [1999]. However, details of the flows at the blade leading edge and tip cannot be captured accurately due to the breakdown of either the linear cavity theory or the thickness-loading coupling corrections.

With the above development in the vortex lattice method, the accuracy of VLM is highly enhanced and close to the level of the low order boundary element method (BEM). However, accuracy of the effective velocity is a prerequisite when accurate results are sought for a complex propulsor system. A lot of effort has been devoted to the evaluation of effective velocity (or called effective wake, as the velocity is after the stern), as presented in the following section 2.2.

The formulation and details of the vortex lattice method will be given in Chapter 3.

2.2 Effective Wake Prediction

In the industry practice, the nominal velocity is used as the inflow to the propeller. The vorticity due to the ship boundary layer is included correctly in the nominal velocity, while the interactions between the propeller and the upstream vortices are missing. Since the 1980s, plenty of studies have been devoted in the effective velocity prediction in order to predict the propeller performance with accuracy.

Huang and Groves [1980], based on the successful measurement of wake very close to the propeller plane, applied a simplified velocity representation for Euler equations to predict the effective wake.

Shih [1988] employed a vortex ring to represent the Euler equation in a non-conservative force field to predict the effective wake. The flow field due to each vortex ring was given by actuator disk theory. This prediction showed good agreement with the measurement for axisymmetric shear flow in the MIT water tunnel.

Besides these inviscid models, Stern et al. [1988b] solved the partially parabolic Reynolds Averaged Navier-Stokes (RANS) equation for 3D axisymmetric propeller-hull interaction problem. Three ways to represent the propeller force were applied: (a) inner boundary condition, where pressure and velocity jump were given as boundary conditions at the propeller location, (b) velocity field interaction, where a new set of equations governing the effective velocity field was used, (c) body force method, where the propeller pressure jump was converted into a source term in the RANS formulation. Their studies showed that the body force method was the best model. The steady flow predictions with body force method were in agreement with the experiment. This method was also implemented by Stern et al. [1994] and Weems and Korpus [1993] for the combined ship wake and propeller flow.

Kerwin et al. [1994] proposed a design procedure with an effective wake instead of a nominal wake. In his procedure, the flow field was decomposed into axisymmetric and non-axisymmetric parts. The former part was obtained by a RANS solver, while the latter one was obtained from the vortex lattice method. The body forces of the blades were computed from the Kutta-Joukowski and the Legally forces acting on the vortices and sources. Later this method was extended to predict the flow around multiple blade-row open/ducted propellers in Kerwin et al. [1997].

Direct modeling of propeller and hull were also successful. Stern et al. [1988a] modeled a rotating infinite-pitch rectangular blades by applying a complete viscous flow solution. Chen et al. [1994] extended this approach to a realistic propeller with prescribed inflow wake. Stanier [1998] used RANS to estimate propeller scale effects. Chen and Stern [1999] solved the RANS for open propeller subject to uniform inflow for four quadrants: forward, back, crashhead and crashback conditions.

A whole array of studies have been performed at the University of Texas at Austin. These studies made a strong foundation for the current work. In the work of Choi and Kinnas [1998], Kinnas et al. [2000] and Choi and Kinnas [2001b], a steady 3-D Euler solver (GBFLOW-3D), based on a finite volume approach and the artificial compressibility method, was developed for the prediction of the 3-D effective wake of single propellers in unbounded flow or in the presence of a circular section tunnel. A body force method was used to represent the propeller in this approach. Compared to approaches of Stern's and Kerwin's group, the follow advantages apply: (1) 3-D Euler approach saves running time and computational effort, and yet yields results close to that of experiments (2) the body forces are converted from pressure distribution on the camber surface directly, and (3) In further studies, it was found that the 3-D Euler solver (GBFLOW-3D) predicted a 3-D effective wake inflow which was very close to the time average of the fully unsteady wake inflow (predicted by WAKEFF-3U [1]). Therefore, it is not necessary to spend long computational time to get the propeller time-averaged performance for fully unsteady propellers. Formulation and numerical details of this method will be presented in Chapter 3

2.3 Studies on Ducted Propellers

Gibson and Lewis [1973] modeled a ducted propeller by coupling an actuator disk method with a surface vorticity method. The propeller was represented by the actuator disk and the rotation was neglected. The duct was more exactly represented by the surface vorticities distributed on the actual surface. The nonlinear thickness effects of the duct were also included by such distribution of vortices.

Glover and Ryan [1973] used a surface vorticity method to represent the duct surface, and a lifting line method to represent the propeller. The computation of the pressures was nonlinear, and duct was modeled more exactly.

An actuator disk model was coupled with an axisymmetric Euler solver by Falcão de Campos [1983]. In this work, the axisymmetric shear flow effects within

---

[1] A unsteady flow solver, incorporated with unsteady body force distribution inside fluid domain, which is based on Choi and Kinnas [2001a]

a radially varying inflow field was included, and the axisymmetric interaction was considered between the duct and the propeller.

Later, lifting surface method was applied to model the complex propeller blade geometry with accuracy. This method was implemented for ducted propeller in steady cases by Van Houten [1986].

Kerwin et al. [1987] combined a potential-based panel method on the duct with a vortex lattice method on the propeller. In this work, flow around the combination of axisymmetric duct and hub were first computed by a low order potential based panel method. Induced velocities at control points of the vortex lattice representation of the blades were evaluated. Strengths of vortex lattice elements were calculated, requiring the total normal velocity vanish at each control point. Perturbation potential at the centroid of each panel was then updated and solution of the panel method were modified. The iteration continues between the vortex lattice method and the panel method. The non-axisymmetric flow on the duct and hub could be captured by the iterative procedure. Helical panels, following the blade and trailing vortex grid at the tip and the root of the blade were utilized, and the sensitivity of potential to the radial position of the control points was addressed. Later, their method was extended to determine the optimum loading distribution on blades inside of a duct which was represented in nonlinear theory by Kinnas and Coney [1992].

Steady and unsteady ducted propeller (single and two-component) flows were addressed by Hughes et al. [1992], Hughes and Kinnas [1993] and Hughes [1993], with the implementation of a time marching panel method for all components. In their work, a generalized image model for hub and duct was applied, which accounted for the hub and duct wall effects without solving the boundary value problem for the duct and hub at each time step. To account for the gap effects on the global flow solution, Hughes [1997] also applied an empirical tip flow gap model.

Srivastava [1996] applied a time-marching Euler solver to model ducted propellers. Free slip condition was satisfied at the surface of duct and propeller when solving unsteady 3D Euler equations. He used a blade-fixed coordinate system, so the duct was treated as a rotor.

Brockett [1999] coupled a boundary element model of the annular duct and the hull with a lifting-line model of the propeller to determine the interaction between the ducted propeller and the stern of an axisymmetric hull. He found that the open propeller, accelerating duct propeller and decelerating ducted propeller had the same level of efficiency due to the interaction effects, while the accelerating ducted propeller had increased course-keeping ability compared to the other two propellers.

Kerwin et al. [1994, 1997] and Warren et al. [2000] applied a hybrid method which coupled a RANS method for the duct with a potential based lifting surface method to include the viscous effects on the duct and hub walls.

More recently, computer intensive RANS calculations have been applied to model both the propeller and the duct.

A Ka series propeller with a NSMB nozzle 19A was analyzed by the RANS solver in work of Sanchez-Caja et al. [2000]. In their work, a multiblock cell-centered finite volume method with sliding mesh was applied to solve the $k - \epsilon$ equations around propeller and duct. At design advance ratio, the thrust coefficient was predicted without noticeable error, however, the torque coefficient differed by 4.5%. Important features of of the propeller flow, such as the hydrodynamic pitch angle of the propeller wake and wake itself, could be predicted with accuracy.

The $k - \epsilon$ and $k - \omega$ models (SST model) were also utilized by Abdel-Maksoud and Heinke [2002], where the scale effects of ducted propellers were studied by applying a RANS solver in a rotating coordinate system, with the inclusion of centrifugal and Coriolis forces. Such an estimation of the the Reynolds number effect on the performance of the propellers was of importance for extrapolation of the model test results to full-scale results.

Lee et al. [1998] modeled the leakage vortex flow for ducted propellers. The method was able to predict the location of the leakage vortices even though it was difficult to capture the location of the leakage vortex core.

Numerical modeling of the gap flow and leakage vortex has been performed in Brewer [2002] by applying a 3D unstructured and unsteady solver U^2NCLE (Unsteady, Unstructured Navier Stokes Solver developed at the Mississippi State University) for ducted propellers. Minimum pressure, circulation and axial/tangential velocities in the vortex core are also investigated.

Hsiao and Chahine [2004] applied RANS for the solution of a complete ducted propulsor flow, then reduced the computational domain and conducted a

DNS calculation to get an improved solution. In this study, bubble dynamics models were applied to track the vortices. Cavitation inception due to vortex/vortex interaction were also investigated.

2.4 Uniqueness of the Current Work

Compared to the methods presented above, the features that are unique for the current method are as following:

- Coupling of the vortex lattice method (VLM) and the finite volume method (FVM) based Euler solver provides an iterative way to predict the hydrodynamic performance and cavitation shapes on ducted propellers. This approach assumes that the vorticity due to the stern boundary layer is included in the nominal wake, and the interaction between the propeller, the duct and the inflow vorticity is inviscid. In the current work, the viscous effects are evaluated, and its influence on the duct thrust is presented.

- Application of the orifice equation model has been seen previously in the boundary element method (BEM). However, the current method, to the best knowledge of author, is the first application to the vortex lattice method (VLM). The implementation of the orifice equation model effectively increases the loading at the tip. A shortcoming of the orifice equation model is that a numerical parameter, discharge coefficient C_Q is determined artificially. The contribution of the current work also includes the evaluation of the discharge coefficient.

- The tip leakage vortex, developed between the duct inner surface and propeller tip, is modeled in the vortex lattice method. Previous studies on tip leakage vortex were all focused on the details such as locations and core radius. The current method focuses on the overall performance of the ducted propeller. Taking advantage of this, it is not necessary to concentrate on the grid resolution near the tip leakage vortex region. The current model of the tip leakage vortex effectively increases the loading at the tip.

- To evaluate the effective velocity accurately, two approaches are applied: (1) effective vectors are calculated directly at the kinematic control points. (2) effective velocities are calculated just at a cell in front of the propeller LE. The former is a more straightforward approach, but the errors in the effective velocity evaluation are up to 3% since control points are very close to the singularities on the blade. The latter method does not pose any difficulties when evaluating the effective velocity. As the number of cells increase, the effective velocity will converge to accurate values at control points.

- Effective pressure term is incorporated in the vortex lattice method. This term is introduced to satisfy the Bernoulli's equation. With the correction, the cavitating performance of ducted propellers and the cavity patterns on the blade are improved.

- The current method can be extended to multi-component ducted propeller and flow inside the waterjet duct in a straightforward way.

Chapter 3

Current Method

In this chapter, the method of predicting the effective velocities for an open propeller is given first. Then the formulation of the vortex lattice method and the finite volume method based Euler solver are presented. The extension of the method for the modeling of the ducted propellers is addressed at the end.

3.1 Effective Velocities Prediction for Open Propellers

As mentioned in the previous chapters, the "effective velocities" for a propeller are solved by subtracting the propeller induced velocities from the total velocities. This approach can be viewed as an example of a Helmholtz's decomposition:

$$\begin{aligned} \vec{q_t} &= \nabla \times \vec{B} + \nabla \phi \\ &= \vec{q_r} \qquad + \quad \vec{q_i} \end{aligned} \tag{3.1}$$

where $\vec{q_r} = \nabla \times \vec{B}$ is the rotational part, and $\vec{B}$ is the vector potential. $\vec{q_i} = \nabla \phi$ is the irrotational part, and ϕ is the velocity potential.

In the work of Choi [2000], the propeller induced velocities $\vec{q_p}$ was used in place of the irrotational part $\vec{q_i}$, and the effective velocities q_e (including the upstream vorticities, interactions between inflow and propeller) in place of the rotational part $\vec{q_r}$, as shown in Figure 3.1.

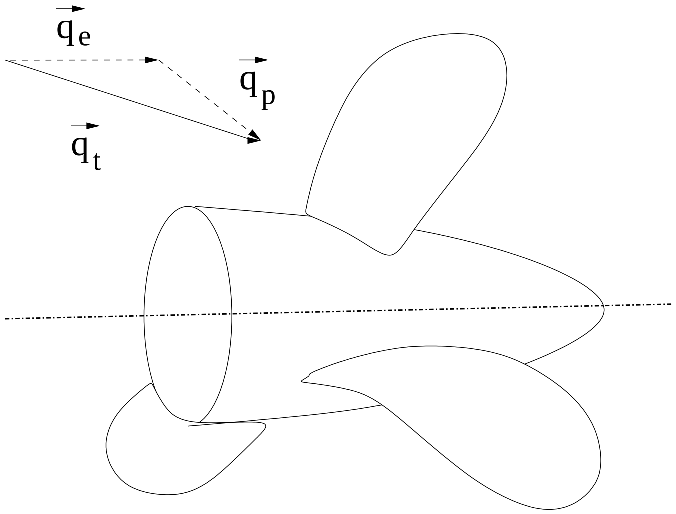

Figure 3.1: Decomposition of the total flow into vortical part and irrotational part.

To solve for the effective velocities, we make the following assumptions: the interaction between the vortical flow and the propeller is inviscid, and the role of viscosity can be neglected. The vortical flow should be measured no larger than two radii ahead of the propeller in order to minimize the viscous effects between the inflow plane and the propeller plane. It is also required that the vortical flow be measured at least half radius ahead, otherwise the flow will be affected by the interaction from the propeller. Some numerical validations on the inviscid approach will be given in Chapter 3.5.

A finite volume method (FVM) based Euler solver was used to solve the total velocities inside the whole fluid domain. Euler equations were solved on the grid points to solve for velocities and pressures. This approach poses no difficulties in handling the non-uniform vortical inflows, since the Euler equations do not require the assumptions of irrotational flow. The nominal wake, including the strong vorticities, can be used as inflow at the inlet boundaries. With the body forces of propeller incorporated as source terms $\vec{f}$ inside the Euler equations, the total velocities were solved as:

$$\frac{D\vec{q_t}}{Dt} = -\frac{\nabla p}{\rho} + \vec{f} \tag{3.2}$$

With given nonuniform wake at the inflow boundary and the body force distribution, the inviscid interaction between the inflow and the propeller can be predicted.

A vortex lattice method (VLM) is used to determine the potential flow in the vicinity of the propeller. This method is only applicable to inviscid irrotational flow, and cannot be applied to non-uniform vortical flow. However, the non-uniform rotational inflow can be included as effective velocities for the propeller to circumvent the difficulties. The propeller induced velocities, $\vec{q_p}$ can be solved from the propeller perturbation potential, ϕ_p, as:

$$\vec{q_p} = \nabla \phi_p \tag{3.3}$$

In solving the VLM for a right-handed propeller, the normal derivative of perturbation potential is required to satisfy the free slip conditions on the propeller camber surface, as:

$$\frac{\partial \phi_p}{\partial n} = -(\vec{q_e} + \vec{\omega} \times \vec{x}) \cdot \vec{n} \tag{3.4}$$

where $\vec{\omega}$ is the angular velocity vector of the propeller rotation and $\vec{x}$ is a vector pointing from the propeller origin to the control point location. There are several useful outputs after solving the VLM: (1) pressure on the blade, which can be converted into body force terms to solve for the Euler equations. (2) perturbation

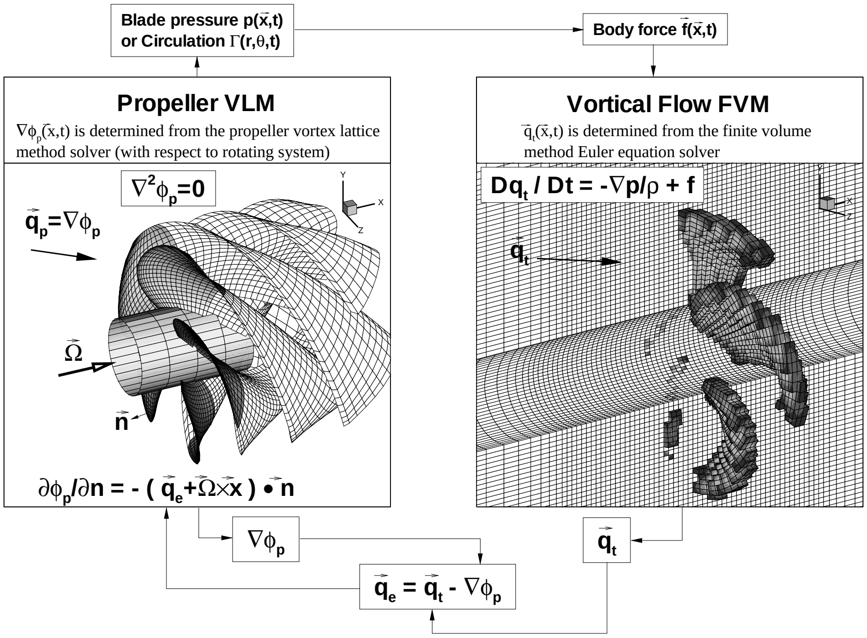

Figure 3.2: Decomposition of the total flow around a single propeller into the potential flow (MPUF-3A) and vortical flow (GBFLOW). From Choi and Kinnas [2003].

potential ϕ_p, which can predict the the induced velocities, as in equation (3.3). (3) thrust and torque, cavity volumes and cavity patterns on the blades.

An iterative procedure between VLM and the vortical flow Euler solver is used to solve the effective velocities for an open propeller, as shown in Figure 3.2. First, we assume the nominal wake to be the effective velocity to the propeller. After the VLM is solved, the perturbation potential and the pressure on the blades are predicted. The pressure is converted into body force terms in the Euler equations. The FVM based Euler equations are solved, with the prescribed body forces. The total velocities are predicted at the effective velocity plane. The effective velocities can then be calculated by subtracting induced velocities (the gradient of perturbation potential at these locations) from the total velocities. With these new effective velocities, the VLM is solved again to predict an updated pressure distribution and perturbation potential distribution. The body force terms in the Euler solver are then updated and the FVM is carried out again. The total velocities are updated, and the new induced velocities are calculated from perturbation potentials and subtracted to get the most recent effective velocities. The iterative procedure continues until the convergence of thrust and torque on blades is reached. As reported in Choi [2000], the iterative process usually converges within three iterations for open propellers.

3.2 Formulation for Vortex Lattice Method (VLM)

The VLM, with the code name MPUF-3A, is used to determine the potential flow in the vicinity of the propeller blade.

In this method, line vortices and sources are placed on the mean camber surface of the blade and the trailing wake. The potential flow in the vicinity of the propeller is the superposition of singularities, which include (1) horseshoe vortices on the blade to represent the blade loading, (2) vortex panels in the trailing wake to represent the trailing vorticity in the wake, (3) line sources on the blade mean camber surface to represent the blade thickness, and (4) line sources on the blade or wake to represent the possible cavity thickness.

The potential flow around the blade is uniquely determined when the strengths of above mentioned singularities are determined. The strengths of the singularities are determined by satisfying the (1) kinematic boundary condition (KBC) and (2) dynamic boundary condition (DBC). The kinematic boundary condition requires

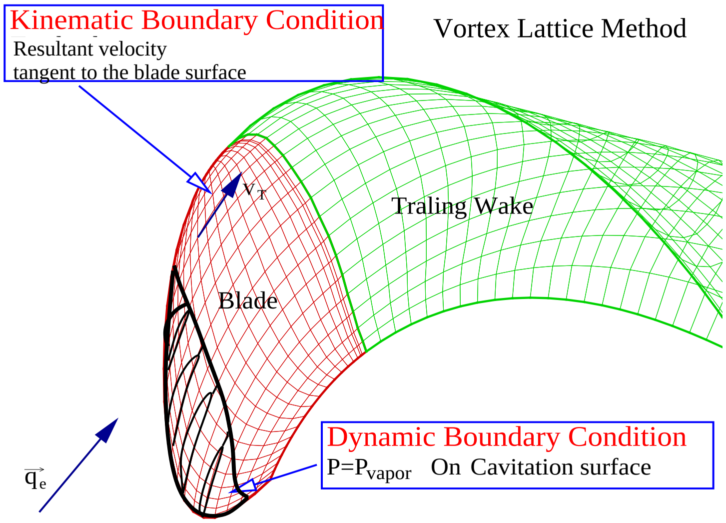

Figure 3.3: Algorithm in solving Vortex Lattice Method.

the flow velocity vectors at the control points to be tangent to the mean camber surface. The dynamic boundary condition requires the pressure on the cavitating part of the mean camber surface be equal to the vapor pressure. The sketch of the scheme is shown in Figure 3.3. Because of the complexity involved in determining the cavity extent and location, an iterative procedure is required to satisfy the dynamic boundary conditions.

On the wetted blade surface, the kinematic boundary condition requires the resultant normal velocity to be zero at the control points. In the work of Lee [1979], the resultant velocity $\vec{V}$ can be written as the summation of the individual contributions as:

$$\vec{n} \cdot \vec{V} = \vec{n} \cdot (\vec{V_\Gamma} + \vec{V_Q} + \vec{V_I} + \vec{V_B} + \vec{V_O}) = 0 \tag{3.5}$$

where $\vec{V_\Gamma}$ is the velocity induced by the line vortices on the key blade and wake; $\vec{V_Q}$

is the velocity induced by the cavity sources on the key blade and wake; $\vec{V_I}$ denotes the inflow velocity, which can contain strong vorticity from boundary layer in the stern region; $\vec{V_B}$ denotes the velocity induced by the line vortices, which represent the thickness of the blade; $\vec{V_O}$ denotes the induced velocity by the other blades and wakes.

The discrete line vortices are grouped into horseshoe vortices with constant strength Γ. For a unit strength, the induced velocity can be solved by Biot-Savart law. Since such an induced velocity can be seen as the influence at the control point by a horseshoe with unit strength, we call this velocity influence coefficient $\vec{v_\gamma}$.

The source strength for the blade thickness, Q_B, could be given from the strip theory. The induced velocity $\vec{V_B}$ is known once the blade thickness is given.

The source strength of the cavity thickness, Q_C, is unknown. A procedure of assumed cavity lengths are used to evaluate the pressure on the cavity surface. In this way, the relationship between computed pressure and cavity lengths is established. A cavity closure condition is required for the strips outside the region where $P > Pv$. Height of the cavity is determined by the kinematic condition, which requires that the substantial derivative of the quantity $F = \psi - g$ vanishes on the camber surface, as

$$\frac{DF}{Dt} = (\frac{\partial}{\partial t} + \vec{V} \cdot \nabla)(\psi - g) = 0 \tag{3.6}$$

where ψ could be viewed as the height of the cavity, and g is the ψ coordinate of the cavity surface. Once the height of the cavity is determined, the cavity thickness Q_C at this time step is determined. A spanwise strip-by-strip iteration procedure is applied to update the cavity extent and height at a time step. When solving equation (3.5), the induced velocity $\vec{V_Q}$ is used as the known value from the previous time step.

The line vortex strengths of Γ on other blades are treated as known values of the last time step. Line sources used to represent the thickness of the other blade are same as those of the key blade, thus are also known.

Grouping all the known quantities of equation (3.5) to the RHS, we have:

$$\sum \Gamma \vec{v_\gamma} \cdot \vec{n} = -(\vec{V_Q} + \vec{V_I} + \vec{V_B} + \vec{V_O}) \cdot \vec{n} \tag{3.7}$$

where Γ is the unknown vortices strengths at this time step, and $\vec{v_\gamma}$ are the influence coefficient.

Once the solution converges, all the singularity strengths on the blades are uniquely determined, and the pressure on the blade can be integrated to get the thrust and torque. During the iteration procedure, the cavity extent and height are also predicted.

3.3 Formulation for Finite Volume Method Based Steady Euler Solver

A finite volume method (FVM) based Euler solver is developed at the University of Texas at Austin to solve the total flow inside the fluid domain. The computational code is named GBFLOW, which represents “G(eneral) B(ody) Flow solver”. The code has two versions: an axisymmetric one named GBFLOW3X, and a 3-D one named GBFLOW3D. It is validated in Choi [2000] that the pre-

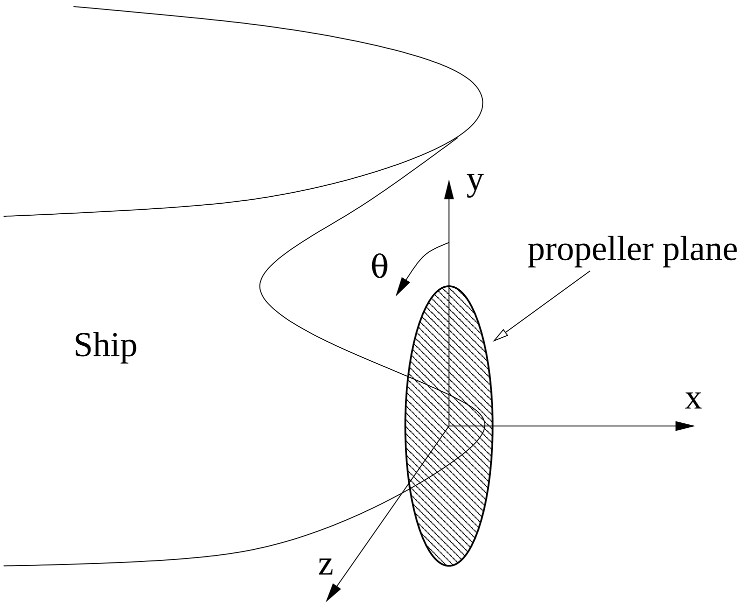

Figure 3.4: Ship-fixed Cartesian Coordinate system, Taken from Choi [2000]

diction from GBFLOW3X is close to the circumferential average of the prediction from GBFLOW3D. In this study, the axisymmetric version will be used for most of the cases, while in some of inclined wake case, the 3-D version applies.

The Euler solver models the flow in the vicinity of the propulsor, by assuming that the interaction of the propulsor with the inflow is primarily inviscid. The propeller action is replaced with appropriate body force in the Euler equations. Axisymmetric and non-axisymmetric, steady and unsteady Euler solvers are developed to predict the effective wake for wetted or cavitating single propellers subject to given nominal wakes (Choi and Kinnas [1998]; Kinnas et al. [1998]; Choi and Kinnas [2000a,b, 2001b]; Choi [2000]). Extensive validations of the predictions of the effective wake in the case of single propellers are given in these references.

A ship-fixed coordinate system is applied for the steady Euler solver, as shown in Figure 3.4. The x-axis points downstream along the propeller shaft and origin of the coordinate is chosen as the center of the propeller disk. For the axisymmetric formulation, a cylindrical coordinate is used, with the positive y-axis extending in the radial direction and the θ-axis satisfying the right hand rule. For the 3-D formulation, a Cartesian coordinate is used, with the y-axis pointing vertically upward and z-axis pointing to the port side (left) of the hull.

3.3.1 Axisymmetric Steady Euler Solver

The axisymmetric Euler solver is helpful especially at the early stage of the propeller design, since propeller designers make use of axisymmetric inflow at this stage. Also, since the Euler solver is solved only in a meridional plane, the solver takes much less time to run compared to the 3-D solver. The axisymmetric Euler equations are solved with only the circumferential mean nominal inflow wake taken into account. This step is sufficient in predicting the mean performance of the propulsor.

The dimensionless axisymmetric incompressible Euler equations, written in the cylindrical coordinate system (x, r, θ), with the corresponding velocity components (u_x, u_r, u_θ), are as follows.

$$\frac{\partial \vec{U}}{\partial t} + \frac{\partial \vec{F}}{\partial x} + \frac{\partial \vec{G}}{\partial r} = \vec{Q} \tag{3.8}$$

where the column matrices U, F and G are defined as follows:

$$\vec{U} = \begin{bmatrix} rp \\ ru_x \\ ru_r \\ ru_\theta \end{bmatrix} \quad , \quad \vec{F} = \begin{bmatrix} ru_x/\beta \\ r(u_x^2 + p) \\ ru_x u_r \\ ru_x u_\theta \end{bmatrix}$$
$$\vec{G} = \begin{bmatrix} ru_r/\beta \\ ru_x u_r \\ r(u_r^2 + p) \\ ru_r u_\theta \end{bmatrix} \quad , \quad \vec{Q} = \begin{bmatrix} 0 \\ rf_x \\ (u_\theta^2 + p) + rf_r \\ -u_r u_\theta + rf_\theta \end{bmatrix} \tag{3.9}$$

where β is the artificial compressibility factor according to the artificial compressibility method in Chorin [1967]

The method requires that the artificial Mach number, $\sqrt{u_x^2 + u_r^2 + u_\theta^2}/c$, be less than 1.0, where the artificial speed of sound is defined as $c = 1/\sqrt{\beta}$. When a steady state is reached, $\partial p/\partial t$ becomes zero and the incompressible solution is obtained.

In order to obtain the body force distribution on the finite volume cells, which correspond to the location of the blade, the pressure difference across the blade surface, Δp, is integrated over the area of the lifting surface intersected by the finite volume cell, as shown in Figure 3.5.

The three-dimensional body force-pressure relation can be written in *dimensional* terms as follows.

$$\hat{\mathcal{V}}_c \hat{\rho} \vec{\hat{f}} = \Delta \hat{p} \hat{A}_c \vec{n} \tag{3.10}$$

where, $\hat{\mathcal{V}}_c$ is the cell volume, $\Delta \hat{p}$ is the pressure difference across the blade surface (evaluated in MPUF-3A), $\hat{A}_c$ is the area of the mean camber surface contained in the cell, and $\vec{n}$ is the normal vector to the mean camber surface. To obtain the

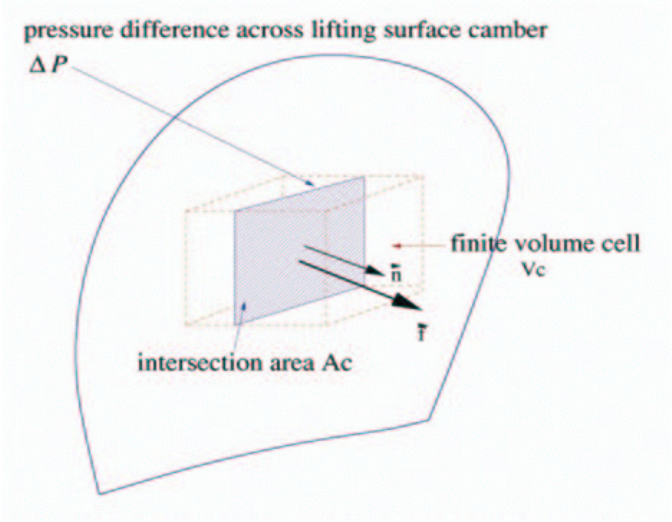

Figure 3.5: Body force determination in the Euler solver, From Kinnas et al. [2001].

corresponding expression for the axisymmetric body force, the cell volume, $\hat{\mathcal{V}}_c$, in equation (3.10) must be changed to the volume of the ring that is created by rotating the area of the side of the cell along the meridian plane, $\hat{\mathcal{A}}_{cell}$, about the shaft axis. Thus, the corresponding dimensionless relation becomes as follows.

$$\left(\frac{2\pi\hat{r}\hat{\mathcal{A}}_{cell}}{R\ \ R^2}\right)\left(\frac{\hat{\vec{f}}}{U_\infty^2/R}\right)\left(\frac{U_\infty^2}{4n^2D^2}\right) \quad = \quad \left(\frac{\Delta\hat{p}\hat{A}_c\vec{n}}{\hat{\rho}n^2D^4}\right)$$

or

$$2\pi r\mathcal{A}_c \qquad \vec{f} \qquad \frac{J_s^2}{4} \quad = \quad \vec{F}_P \tag{3.11}$$

where, the dimensionless pressure force $\vec{F}_P$ can be obtained from the propeller potential flow solver (MPUF-3A). $\hat{r}$ is the radius of the centroid of the cell, R and D are the propeller radius and diameter respectively, J_s is the advance ratio based on the ship speed, and n is the rotational frequency of the propeller.

As a result, the dimensionless *axisymmetric* body force can be evaluated using the following formula:

$$\vec{f} = \left(\frac{2}{\pi r \mathcal{A}_{cell} J_s^2} \right) \vec{F}_P \tag{3.12}$$

This pressure-based formulation for the body force has improved the performance of the method in the case of high skew propellers, compared to that of the circulation-based formulation used in Choi and Kinnas [2001b].

3.3.2 Three-Dimensional Euler Solver

The three-dimensional incompressible Euler equations can be written in the following form with respect to the dimensionless variables, again using the artificial compressibility method.

$$\frac{\partial \vec{U}}{\partial t} + \frac{\partial \vec{F}}{\partial x} + \frac{\partial \vec{G}}{\partial y} + \frac{\partial \vec{H}}{\partial z} = \vec{Q} \tag{3.13}$$

The terms $\vec{U}$, $\vec{F}$, $\vec{G}$, $\vec{H}$, and $\vec{Q}$ are defined as follows.

$$\vec{U} = \begin{bmatrix} p \\ u \\ v \\ w \end{bmatrix}, \qquad \vec{F} = \begin{bmatrix} u/\beta \\ u^2 + p \\ uv \\ uw \end{bmatrix}, \quad \vec{G} = \begin{bmatrix} v/\beta \\ uv \\ v^2 + p \\ vw \end{bmatrix}$$

$$\vec{H} = \begin{bmatrix} w/\beta \\ uw \\ vw \\ w^2 + p \end{bmatrix}, \quad \vec{Q} = \begin{bmatrix} 0 \\ f_x \\ f_y \\ f_z \end{bmatrix}$$

The rest of the formulation is similar to that of the axisymmetric Euler solver; i.e. the adoption of a vertex based scheme, Ni's Lax-Wendroff Method for the time discretization, and the fourth order artificial viscosity.

The three-dimensional body force distribution can be obtained from the pressure distribution on blades, by applying equation (3.10) directly. Using dimensionless quantities, equation (3.10) can be re-written as follows.

$$\left(\frac{\hat{\mathcal{V}}_c}{R^3}\right)\left(\frac{\hat{\vec{f}}_{3D}}{U_\infty^2/R}\right)\left(\frac{U_\infty^2}{4n^2D^2}\right) \quad = \quad \left(\frac{\hat{p}\hat{A}_c\vec{n}}{\hat{\rho}n^2D^4}\right)$$

$$\text{or}$$

$$\mathcal{V}_c \qquad \vec{f}_{3D} \qquad \frac{J_s^2}{4} \quad = \quad \vec{F}_P \tag{3.14}$$

As a result, the dimensionless *three-dimensional* body force can be calculated by the following formula.

$$\vec{f}_{3D} = \left(\frac{4}{\mathcal{V}_c J_s^2}\right)\vec{F}_P \tag{3.15}$$

In Choi and Kinnas [2001b], the body force was varied in the circumferential direction according to the propeller loading at the same blade angle. This body force can be considered as the time average of the body force at a point in space in the case of a non-axisymmetric nominal inflow.

3.4 Solution of Finite Volume Method

Equation (3.8) with each term defined in equation (3.9), is the final form of the axisymmetric governing equation to be solved using the finite volume method. Note that equation (3.8) is weakly conservative since there are terms on the right hand side which inevitably include u_θ, u_r, and p.

A vertex based scheme is used in the numerical implementation, in which the velocity and pressure values are stored and handled at the vertices. One of the advantages is that the treatment of the boundary is then direct: no interpolation needed.

To solve the axisymmetric governing equation (3.8), the fluid domain is discretized into quadrilateral cells. The governing equations are integrated over the area of the cells. The Gauss divergence theorem is applied to convert the area integrals to line integrals, as the following semi-discrete integral equation:

$$\frac{\partial \vec{U}}{\partial t} S_{ij} + \sum_{edges} (\vec{F} dr - \vec{G} dx) = \vec{Q} S_{ij} \tag{3.16}$$

where S_{ij} is the area of cell with ith index in ξ direction and jth index in η direction, as shown in Figure 3.6. Details about the curvilinear coordinates ξ and η are given in Appendix A.

The summation over the edges in equation (3.16) is defined as the residual $\vec{R}$. For a cell with index i, j, the residual is:

$$\vec{R}_{i,j} = \sum_{edges} (\vec{F} dr - \vec{G} dx) = \sum_{e=N,W,S,E} (\vec{F}_e \Delta r_e - \vec{G}_e \Delta x_e) \tag{3.17}$$

where $\vec{F}_e$ and $\vec{G}_e$ are the average values of $\vec{F}$ and $\vec{G}$ at edge "e" respectively. Δx_e and Δr_e represent the difference in the x and r coordinates at the same edge.

Ni's Lax-Wendroff Method (Ni [1982]) is used for the time discretization. As a second-order explicit method, the unknown $\vec{U}$ at time step $n+1$ is expressed in term of the known $\vec{U}$ and the first and second derivatives at the time step n, by Taylor series expansion.

$$\vec{U}_{i,j}^{n+1} \simeq \vec{U}_{i,j}^{n} + \left(\frac{\partial \vec{U}}{\partial t} \right)_{i,j}^{n} \Delta t + \left(\frac{\partial^2 \vec{U}}{\partial t^2} \right)_{i,j}^{n} \frac{(\Delta t)^2}{2} \tag{3.18}$$

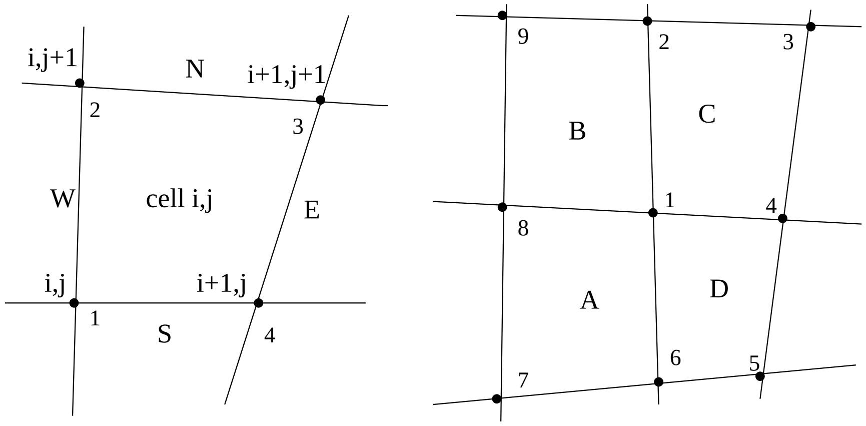

Figure 3.6: A quadrilateral FVM cell (left) and the cell influencing a given node (right). Adjusted from Kinnas [1999]

The first derivative term in equation (3.18) is evaluated as the average of $\left(\frac{\partial \vec{U}}{\partial t}\right)^n$ of the four neighboring cells A, B, C, D, as shown in Figure 3.6.

$$\left(\frac{\partial \vec{U}}{\partial t}\right)^n_{i,j} \simeq \frac{1}{4}\sum_{cells}\left(\frac{\partial \vec{U}}{\partial t}\right)^n_{cells} = \frac{1}{4}\sum_{c=A,B,C,D}\left(-\frac{R^n_c}{S_c} + Q^n_c\right) \tag{3.19}$$

where R^n_c is the residual evaluated as in equation (3.17).

The second derivative term in equation (3.18) are also taken as the average of neighboring cell A, B, C, D, as

$$\left(\frac{\partial^2 \vec{U}}{\partial t^2}\right)^n_{i,j} \simeq \frac{1}{4}\sum_{c=A,B,C,D}\frac{\partial}{\partial t}\left(-\frac{R^n_c}{S_c} + Q^n_c\right) = \frac{1}{4\Delta t}\sum_{c=A,B,C,D}\left(-\frac{\Delta R^n_c}{S_c} + \Delta Q^n_c\right) \tag{3.20}$$

where ΔR^n_c and ΔQ_c are the changes in the value of R^n_C and Q^n_c between time steps n and $n-1$.

Grouping all the contribution of first derivative and second derivative terms in equations (3.19 and 3.20) for all the neighboring cells, equation (3.18) can be written as:

$$\vec{U}^{n+1}_{i,j} = \vec{U}^n_{i,j} + \sum_{c=A,B,C,D}(\delta \vec{U}_{i,j})^n_c \tag{3.21}$$

where $(\delta \vec{u}_{i,j})^n_c$ are the contribution from neighboring cells at time step n.

To improve the stability, the second and fourth order viscosity μ_2 and μ_4 are added to the RHS of the equation (3.21), as:

$$\vec{U}^{n+1}_{i,j} = \vec{U}^n_{i,j} + \sum_{c=A,B,C,D}(\delta \vec{U}_{i,j})^n_c + \Delta t(\mu_2 - \mu_4) \tag{3.22}$$

with

$$\begin{aligned}\mu_2 &= \sigma_2(\delta_{ii}\vec{U}^n_{i,j} + \delta_{jj}\vec{U}^n_{i,j}) && (3.23)\\ \mu_4 &= \sigma_4(\delta_{iiii}\vec{U}^n_{i,j} + \delta_{jjjj}\vec{U}^n_{i,j}) && (3.24)\end{aligned}$$

where σ_2 and σ_4 are second and fourth order viscosity coefficients respectively.

The finite central difference operators, δ_{ii} and δ_{iiii} in equation (3.23) and (3.24) are defined as follows.

$$\begin{aligned}\delta_{ii} &= (\ \ )_{i-1} - 2(\ \ )_i + (\ \ )_{i+1} && (3.25)\\ \delta_{iiii} &= (\ \ )_{i-2} - 4(\ \ )_{i-1} + 6(\ \ )_i - 4(\ \ )_{i+1} + (\ \ )_{i+2} && (3.26)\end{aligned}$$

The time step size, Δt, is related to the grid size via the CFL condition (Courant et al. [1967]). The convergence criterion is that the maximum change in the dimensionless velocity and pressure is less than 10^{-6}.

In the 3-D case, The semi-discrete equation of equation 3.13 can be written for each cell as:

$$\frac{\partial \mathbf{U}_{(i,j,k)}}{\partial t} V_{(i,j,k)} + \sum_{faces} (\mathbf{F}A_x + \mathbf{G}A_y + \mathbf{H}A_z) = \mathbf{Q}_{(i,j,k)} V_{(i,j,k)} \qquad (3.27)$$

where, $V_{(i,j,k)}$ is the volume of the cell (i, j, k), and (A_x, A_y, A_z) are the projections of the area of each face along the (x, y, z) directions, respectively. The treatment is just the extension of that in the axisymmetric case. The difference is that a vertex in the 3-D space will have eight neighboring cells.

3.5 Choice between Inviscid and Viscous Model

The hydrodynamic performance of cavitating propellers can be predicted by the vortex lattice method (MPUF-3A). However, the accuracy of the predictions (especially in terms of the cavity extent and volume) is highly dependent on the accuracy of the effective inflow. In order to predict the effective wake, an Euler solver is applied and coupled with the VLM. The choice of an inviscid flow (Euler) solver instead of a viscous flow (RANS) solver will be justified here.

The Euler solver, due to its inviscid flow assumptions, would be unable to predict the thick turbulent boundary layer near the stern if applied over the full length of the hull. As a result, the effective wake is predicted inaccurately. However, if the inflow is known somewhere upstream of the propeller (from measurements or a viscous flow solver), and if the effects of viscosity between the inflow boundary and the propeller can be neglected, then an Euler solver should be able to capture the inviscid vorticity dynamics and the interaction between inflow and the propeller. This inflow location has to be “close enough” so that the effects of viscosity between this location and the propeller can be neglected, and “far enough” so that the propeller does not affect the inflow. Some preliminary numerical tests have indicated that for moderately loaded propellers, 2-4 propeller radii upstream of the propeller plane should be sufficient. In other words, it is assumed that viscosity plays a significant role in the flow upstream of the inflow boundary, and a less significant role between inflow boundary and the propeller.

In Figure 3.7, half of an axisymmetric hull is shown with the solution domain and the corresponding boundary conditions. As a first step, in the “full do-

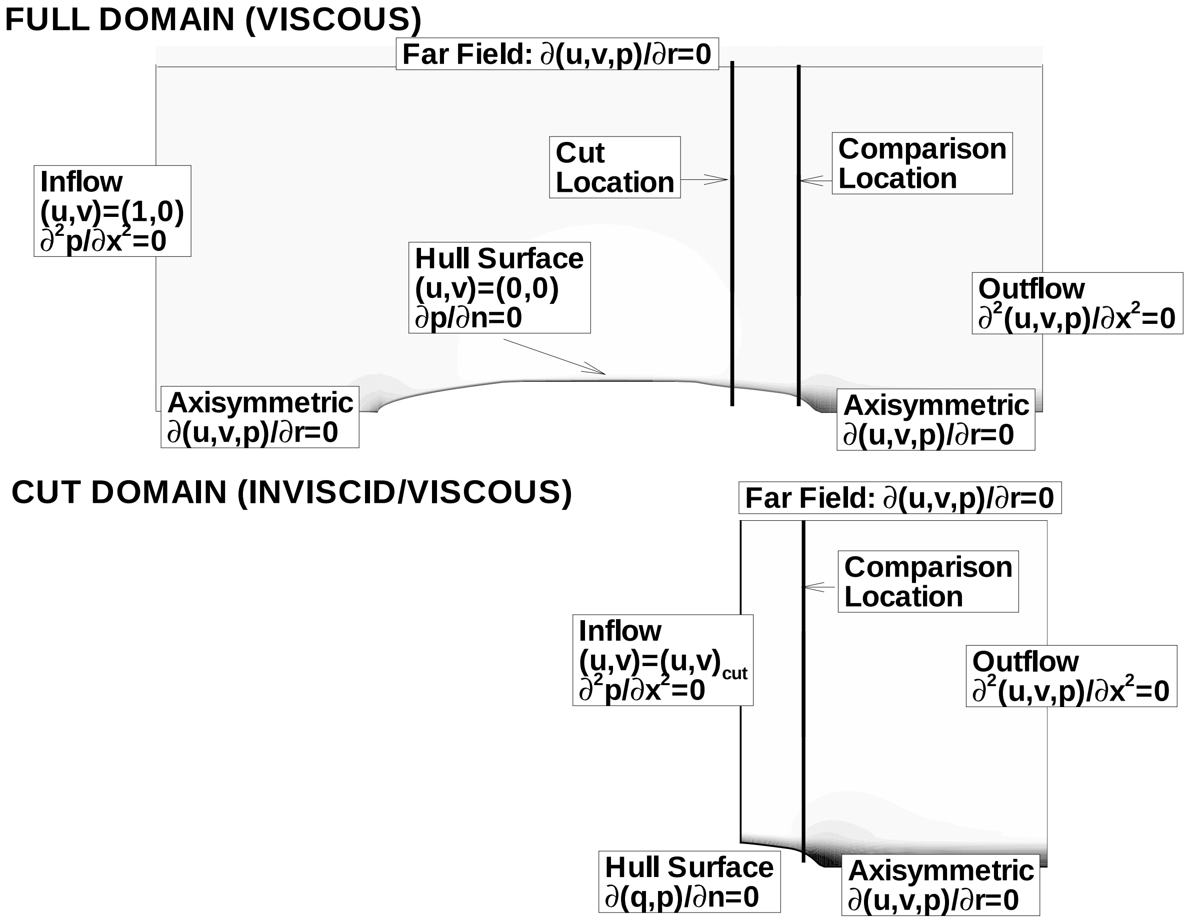

Figure 3.7: The comparison procedure.

main”, a viscous solver is used to evaluate the flow at an axial “cut location”. A new domain is defined from the cut location to the downstream boundary of the full domain, which is called the “cut domain”. Using the flow (as determined by the viscous solver) at the cut location as the inflow, the Euler solver is applied on the cut domain. The velocity profiles from both solvers are compared at the same axial location at the stern. There can be an additional step: the viscous solver can be applied on the cut domain to test the possibility of retrieving the full domain result by using the inflow at the cut location.

(CASE 1) An axisymmetric body with a parabolic bow and Huang’s stern D (Huang and Groves [1980]) is used, as shown in Figure 3.7. The axisymmetric version of a commercial CFD code FLUENT was applied. The solver is segregated, implicit, axisymmetric and unsteady, with 5 equations model for the turbulent viscosity. Uniform inflow with Reynolds number, $Re = 10^6$ (based on the length of the hull) was given at the inflow boundary. The SIMPLE algorithm was applied for the pressure and velocity coupling. The momentum equations were discretized using a second order upwind scheme, while the turbulent kinematic energy and dissipation rate equations were discretized using a first order upwind scheme. The full domain was solved first using FLUENT, and the inflow at the location of the cut was evaluated at $x_{cut} = 0.8$. Taking the inflow from FLUENT, Euler solver (GBFLOW-3X) was applied on the cut domain. The predicted velocities at $x_{prop} = 0.95$, which was located at part of the curved stern at the location of the propeller, were compared to those from the viscous solver. The velocity profiles at the propeller plane were compared in Fig. 3.8. The velocity profiles compare well everywhere except in the vicinity of the propeller root. This local difference is due to the fact that in the Euler solver a free-slip condition is applied on the wall.

(CASE II) Another hull geometry with parabolic bow and stern is shown in Figure 3.9. Again FLUENT was applied, with Reynolds stress 5 equation model and Reynolds number $Re = 10^7$ (based on the length of the hull). Other configurations are similar to the previous case. The cut location was at $x_{cut} = 1.0$ and the velocity profiles are compared at $x_{prop} = 2.0$. The contour of axial velocities are shown in Figure 3.9, and the comparison between axial velocity and tangential velocity in Figure 3.10.

From the velocity comparisons for both cases, the error seems acceptable since it is compensated by the dramatic savings on the computation time and storage needed for the Navier-Stokes solver. The numerical tests for different Reynolds numbers were performed and it was found, as expected, that higher the Reynolds number, the closer the velocity profiles predicted by the viscous and the Euler solvers are.

3.6 Model of Ducted Propeller

In this section, the general procedure for modeling ducted propellers is discussed. However, the characteristics described below are not the key points which make the current method different from that of other research groups. Only the special treatments, which are discussed in following independent chapters, bring the current study its own merits.

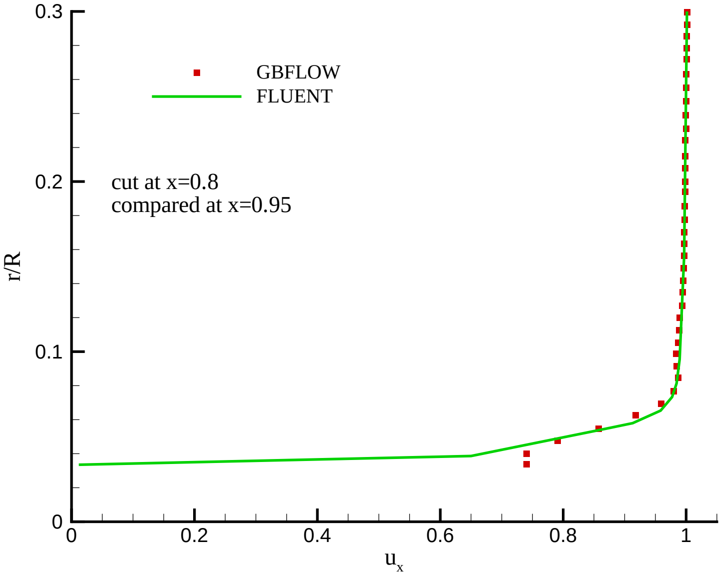

Figure 3.8: Axial velocity comparison at $x = 0.95$.

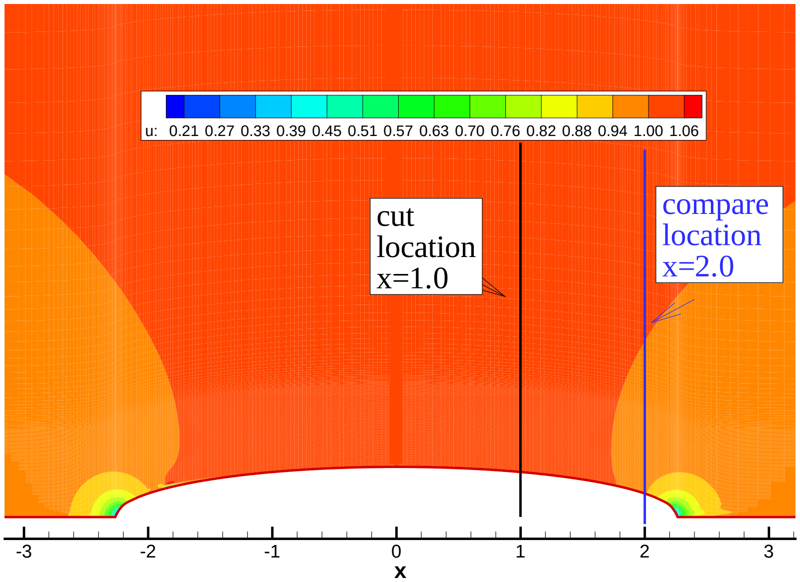

Figure 3.9: Geometry and axial velocity contours for an axisymmetric hull of case II.

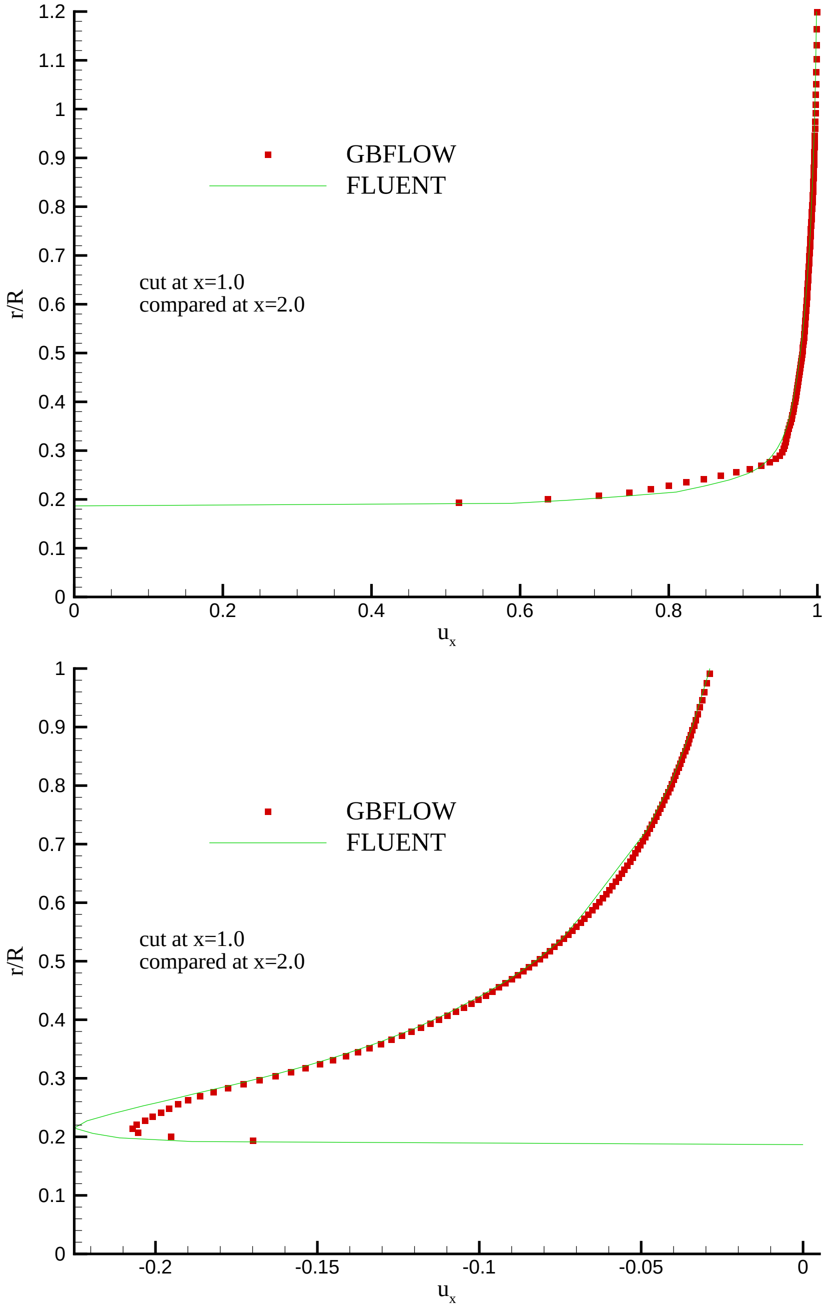

Figure 3.10: Axial velocity (top) and radial velocity (bottom) compared at the propeller plane for case II.

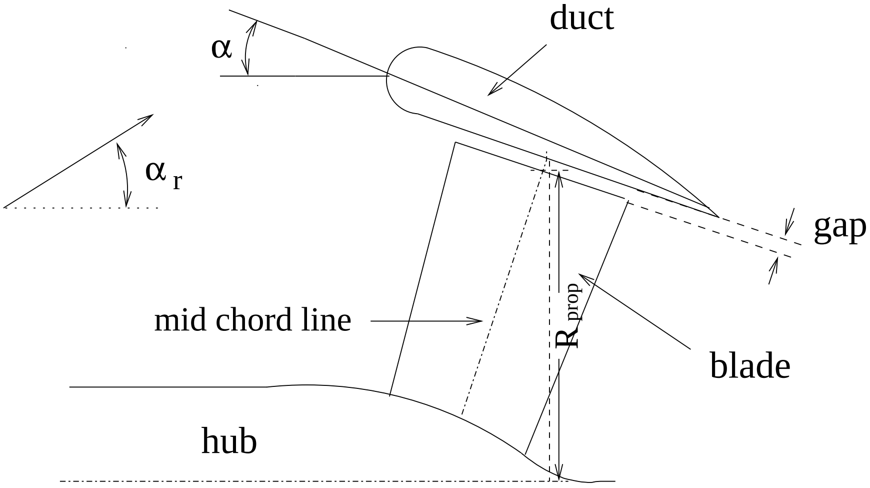

Figure 3.11: Ducted propeller section and geometric parameters.

3.6.1 Geometry Description and Numerical Discretization

Figure 3.11 depicts a typical section of a ducted propeller, where the main geometric parameters are also indicated. The angle of attack of the duct section is α. For most ducted propellers, tips of the blades are designed to have a finite chord length to adapt to the duct surface. There exists a constant gap between the tip and the duct inner surface, which is normally expressed as a percentage of the propeller radius (defined at the midchord of the tip). The inflow can be at an angle α_r with respect to the duct axis.

The original vortex lattice grid in the spanwise direction is created by coaxial cylindrical surfaces. However, for ducted propeller and/or propellers with conical hub, the radii at the tip or hub are not constant any more. Natarajan [2003] modeled the blade geometry between a given hub and duct surface and determined the coordinates of the vortex panels as functions of the arclength, S, by using cu-

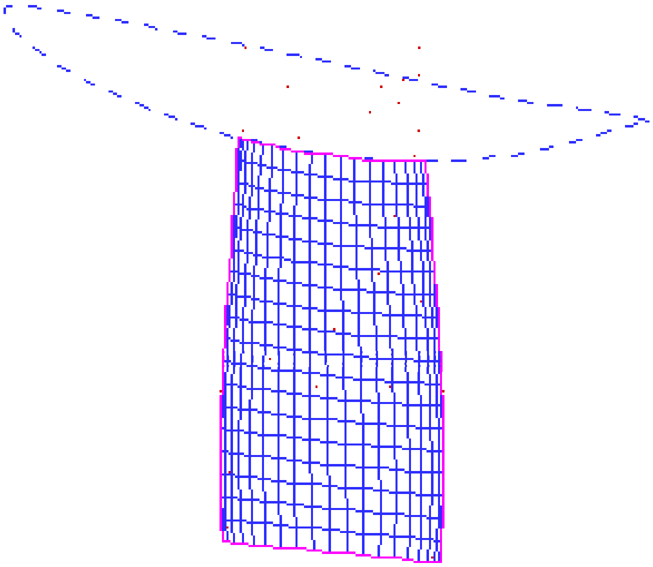

Figure 3.12: Adapted grid follows the geometry of the duct in VLM. From Kinnas et al. [2002]

bic splines. A Newton Raphson scheme is used to find the intersection point with the duct and hub surfaces. After these intersection points are determined, the grid points are redistributed according to the given spanwise spacing. The technique of adapting the blade geometry to duct surface is shown in Figure 3.12, where the duct section is placed at a large angle of attack, and at the same time, the radius of the duct is much smaller than 1.0.

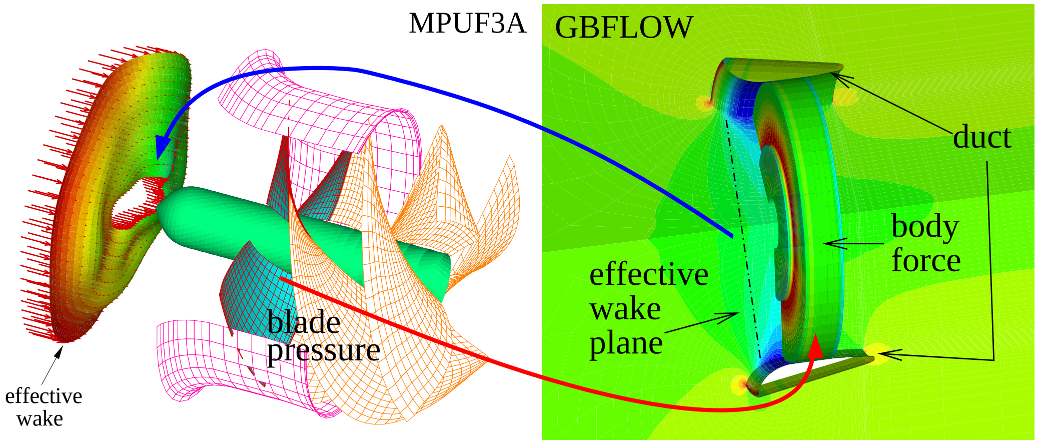

Figure 3.13: Iterative solution method for ducted propeller problems.

3.6.2 Interaction Between Duct and Propeller

While the propeller is modeled in MPUF-3A via the lifting surface vortex-lattice method, the duct is modeled as part of the solid boundary of the fluid domain in GBFLOW. The interaction between the propeller and the duct can thus be considered by iterating between the duct and the propeller. The initial propeller force is predicted by MPUF-3A with a guessed uniform inflow. GBFLOW then takes over and converts the propeller forces into body force terms in the right-hand side of Euler equations. GBFLOW evaluates the total velocity flow-field and subtracts from it the propeller induced velocities (at the propeller effective wake plane) to produce the updated effective velocity. The updated effective velocity is then used by MPUF-3A to modify the pressure force distribution on the blades. This iterative procedure, as shown in Figure 3.13, is repeated until the forces on the blades converge to within a specified tolerance.

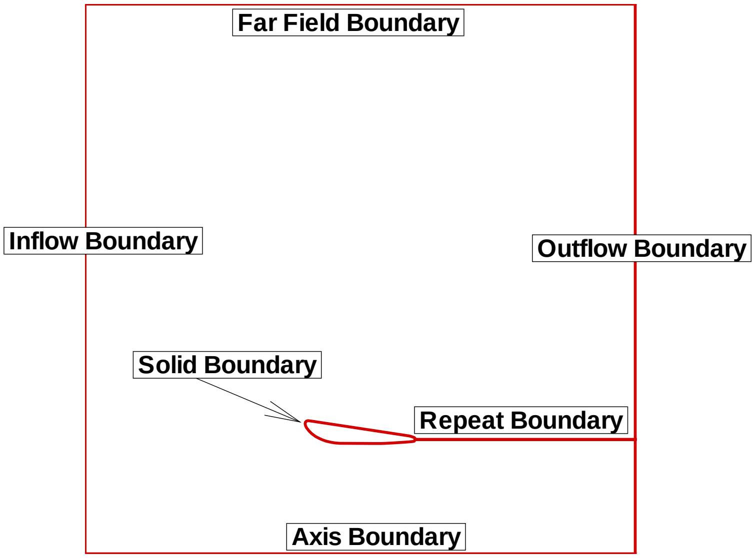

Figure 3.14: Flow domain around the duct and boundary conditions in the Euler solver.

3.6.3 Grid and Boundary Conditions

In the present work, only axisymmetric duct and hub geometries are considered. A 2-D grid is generated for the axisymmetric version of GBFLOW, and then rotated along the x-axis to create the 3D grid for GBFLOW3D. The domain is doubly-connected because of the existence of the duct. A ’C’ type grid is applied to make the domain simply-connected, and to simplify the numerical implementation, as shown in Figure 3.14.

The current grid generation code can import any arbitrary duct geometries and at the same time includes a basic library for NACA sections, such as

NACA66/00 thickness distribution, and NACA 0.8 meanline camber distribution. The grid is refined at the leading and trailing edges of the duct with full cosine spacing either along the axial direction or along the arclength direction. Elliptic grid is generated by solving the Laplace equation using the Gauss-Seidel iterative method. The details on grid generation are found in Appendix A. The grid close to the propeller location inside the duct is not smoothed in the axial direction on purpose. The intention here is to have flat propeller and effective wake planes.

The boundary conditions in GBFLOW are specified on each boundary of the domain, as follows:

- Inflow boundary: The nominal velocities are given at the boundary to represent the flow at the upstream of the propeller. The velocities at grid points are interpolated from the nominal velocities, and the pressure values at this plane can be evaluated by the zero gradient of pressure in the axial direction.

$$(u, v, w) = (u, v, w)_{inflow}, \qquad \frac{\partial p}{\partial x} = 0 \tag{3.28}$$

- Outflow boundary: Developed flow are assumed at this boundary, all the flow gradients in the axial direction are zero.

$$\frac{\partial (u, v, w, p)}{\partial x} = 0 \tag{3.29}$$

- Far field boundary: Velocities at this boundary are kept same as the inflow, since the boundary is out of influence of the duct and propeller. Pressure values on this plane are calculated from pressures inside of flow domain.

$$(u, v, w) = (u, v, w)_{inflow}, \qquad \frac{\partial p}{\partial n} = 0 \tag{3.30}$$

- Axis boundary: All the velocity and pressure values are averaged from the adjacent cells.

$$(u, v, w, p) = \frac{1}{N_K} \sum_{i=1}^{i=N_K} (u, v, w, p)_i \tag{3.31}$$

  where $i = 1, ...N_K$: cell nodes next to the axis, and N_K is the number of cells in the circumferential direction.

- Solid boundary: free slip boundary conditions are applied on the this boundary. A zero normal pressure gradient is also required.

$$\vec{q} \cdot \vec{n} = 0, \qquad \frac{\partial p}{\partial n} = 0 \tag{3.32}$$

  where $\vec{q} = (u, v, w)$.

- Repeat boundary: the values of the velocities and pressure are averaged from those at the adjacent nodes. Notice this boundary does *not* represent the actual duct trailing wake. It is just a branch cut which makes the domain simply-connected, as presented in Appendix A.

Chapter 4

Image and Gap Models

In this chapter, an image model is first introduced and then a gap model. The image model is applied to include the duct wall effects with additional image vortex panels. A gap model, based on the orifice equation, is implemented in the vortex lattice method to account for the effects of the gap flow in a global sense. The method does not attempt to predict the details inside the gap clearance region, but rather include the gap effect to provide a more accurate prediction of the blade circulation at the tip region.

4.1 Image model

4.1.1 Introduction and Numerical Implementation

As described in Kerwin et al. [1987], the flow around the duct is expected to vary between blades, especially in the case of very small tip gaps. This is usually called the “duct wall effect” (or “hub wall effect” in the case of the hub).

In principle, the present method should be able to predict the duct wall effect by using a grid in GBFLOW which rotates with the propeller, and a body force model which places the forces at the blade location along the circumference. However, given that the blade is represented with body forces, this grid would be in general quite inaccurate in predicting the correct flow variation around the duct and the correct loading at the propeller tip.

In order to deal with the “duct/hub wall effect”, a simplified image model with respect to the inner duct surface and the hub surface is used in MPUF-3A. The accuracy of the simplified image model was tested versus that of the generalized (exact) image model in the case of ducts and hubs in Kinnas and Coney [1992]. For a ducted propeller, the image of the blade with respect to the duct inner surface should be generated in addition to that of the hub image.

The image vertices are determined by Kinnas et al. [2002], as

$$R_{B_i} = R_d (X_B)^2 / R_B \tag{4.1}$$

$$X_{B_i} = X_B \tag{4.2}$$

where R_{B_i} and X_{B_i} are the radial and axial coordinates of the image respectively. R_B and X_B are coordinates of the blade vertices and R_d stands for the radius of the inner surface of the duct.

The image of the hub can be determined in a similar way:

$$R_{B_i} = R_h (X_B)^2 / R_B \tag{4.3}$$

$$X_{B_i} = X_B \tag{4.4}$$

where R_h stands for the radius of the hub.

Following the above approach, a blade and its hub and ducted images are shown in Figure 4.1.

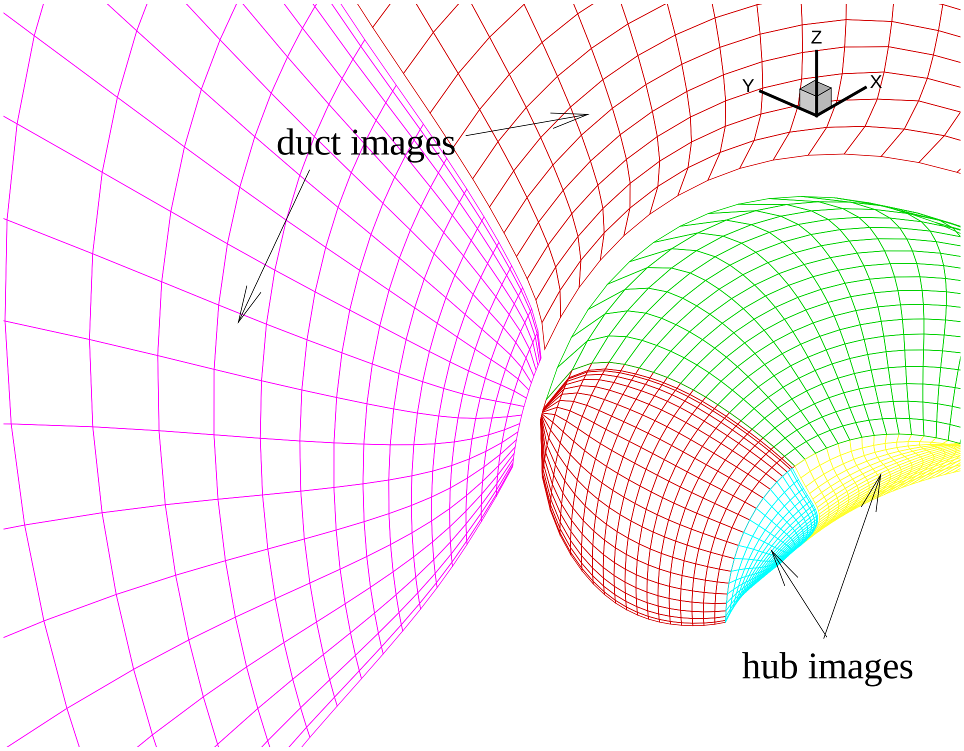

Figure 4.1: A blade with hub/duct images, based on equation (4.3), (4.4), (4.1) and (4.2)

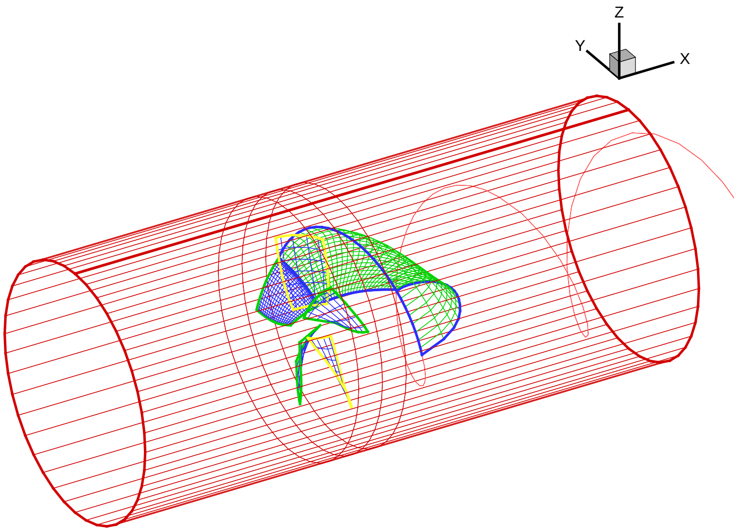

Figure 4.2: Propeller P3745 inside a straight tunnel, with zero gap clearance

4.1.2 Effects of duct images

In this section, the effects of duct images are studied. The focus is to verify that the induced radial velocity due to the image are canceling that from real vortices at the duct wall.

A straight tunnel can be viewed as a simple duct. In this study, we use P3745 inside a straight tunnel. The gap between tunnel and blade tip is 0%. The geometry of tunnel and propeller are shown in Figure 4.2.

The circumferentially averaged induced radial velocity at tunnel surface ahead of the blade is evaluated. To exclude the effects of other blades, a one blade propeller is used as the first case. The induced velocities from the blade vortices and their images are shown in Figure 4.3, and those from transition wake and corresponding images are shown in Figure 4.4. The sum of induced velocities from vortices and their images are seen to be close to zero. There are no penetrating radial velocities that violates the tunnel wall boundary condition. At $x = -0.175$, which is a cell in front of propeller LE in GBFLOW, the induced velocities are evaluated in the circumferential locations. For induced radial velocity from blade vortices and their images, the velocity contours are shown in Figure 4.5, and at the outer-most circle $r = 1.0$, the velocities are shown along blade angles in Figure 4.6. For induced radial velocity from transition wake vortices and their images, the velocity contours are shown in Figure 4.7, and at the outer-most circle $r = 1.0$, the velocities are shown along blade angles in Figure 4.8. The cancellation occurs at blade locations and average to be close to zero for vortices and images from blade. Since the wake length occupies the whole blade angles, the cancellation between transition wake vortices and their images can be seen when they are averaged.

4.2 Gap model

4.2.1 Introduction

For an open propeller subject to a given inflow, the loading at the tip reaches zero. For ducted propeller, the loading at the tip has a finite value due to extremely small clearance between the blade tip and duct inner surface. The viscous effects inside the small gap region influence the overall performance of the ducted propeller. In this sense, it is necessary to develop an effective model to consider the viscous effect inside the gap.

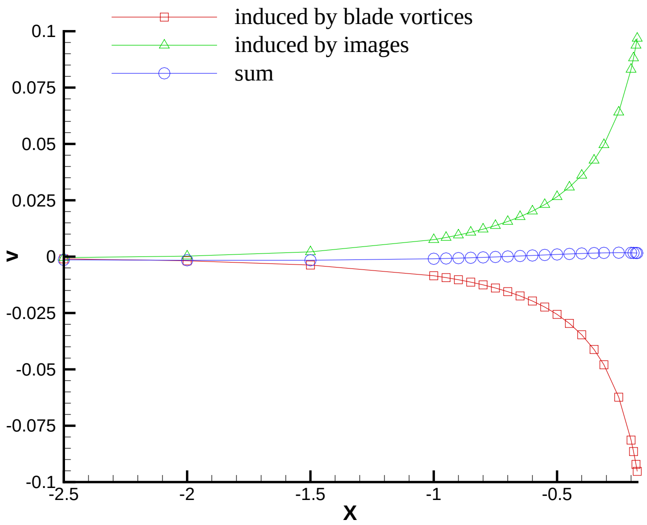

Figure 4.3: Circumferentially averaged induced radial velocities ahead of propeller, for blade vortices and their images of one bladed P3745.

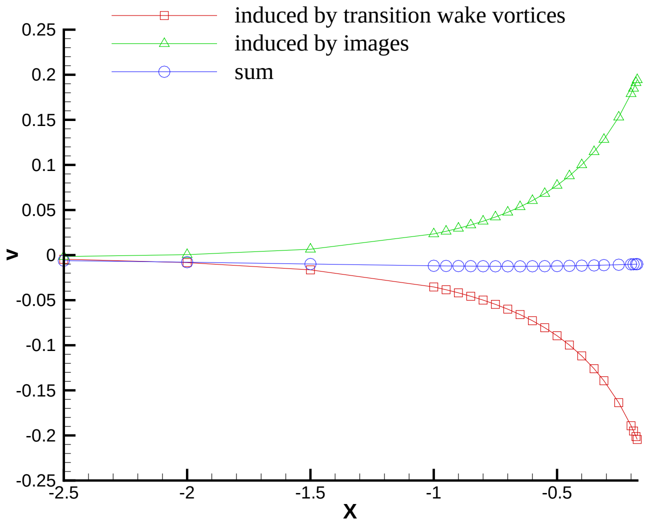

Figure 4.4: Circumferentially averaged induced radial velocities ahead of propeller, for transition wake vortices and their images for one bladed P3745.

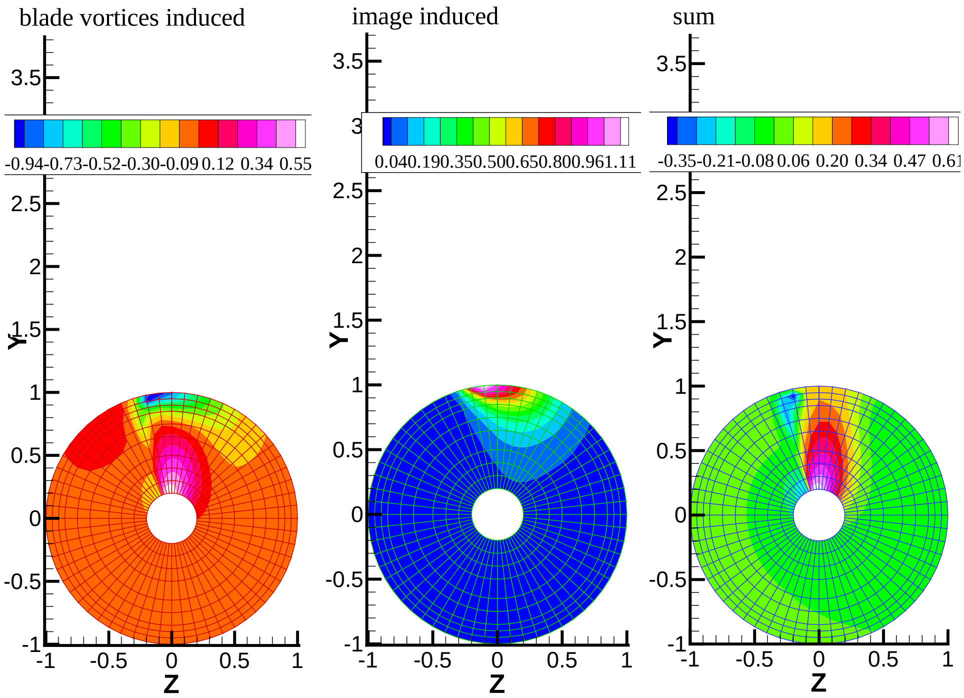

Figure 4.5: Induced radial velocities ahead of propeller at $x = -0.175$, for blade vortices and their images of one bladed P3745.

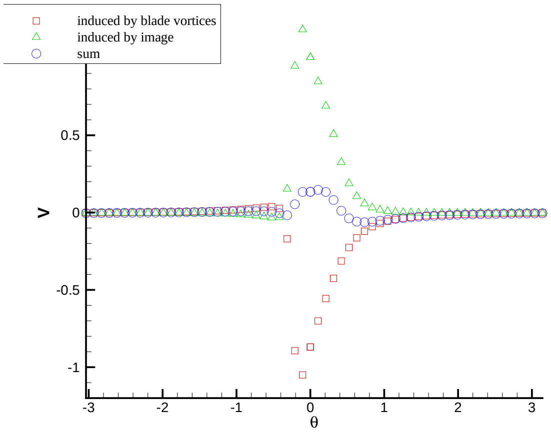

Figure 4.6: Induced radial velocities ahead of propeller at $x = -0.175$ and $r = 1.0$ along blade angles, for blade vortices and their images for one bladed P3745.

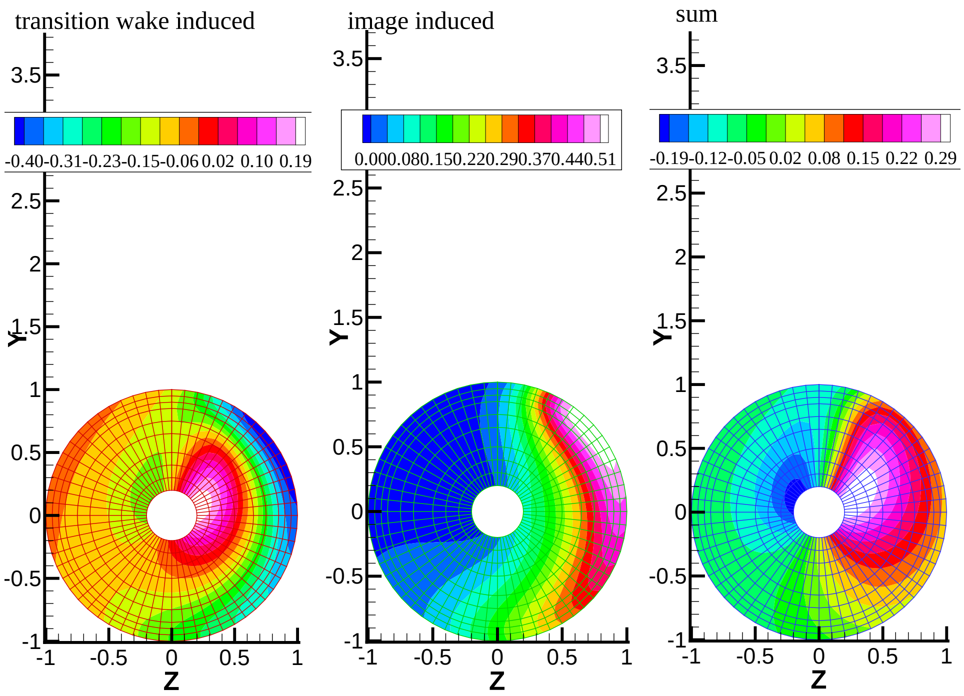

Figure 4.7: Induced radial velocities ahead of propeller at $x = -0.175$, for transition wake vortices and their images of one bladed 3745.

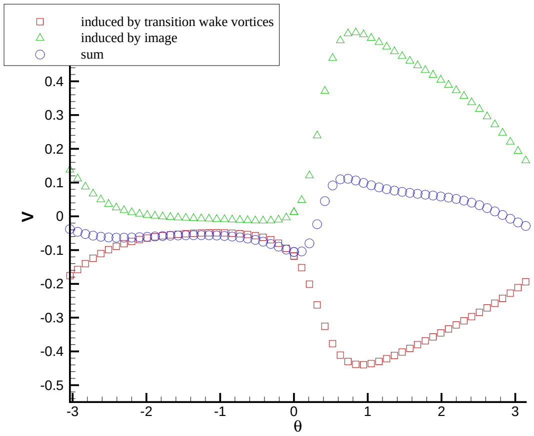

Figure 4.8: Induced radial velocities ahead of propeller at $x = -0.175$ and $r = 1.0$ along blade angles, for transition wake vortices and their images for one bladed 3745.

From flow visualizations and measurements in the experiments of Chesnakas and Jessup [2003], and detailed viscous flow calculations by Brewer et al. [2003], a strong tip vortex is seen to develop from the leading edge part of a square tip blade, similar to that off the leading edge of a delta wing. This tip vortex will interact with the vortex which is coming off the trailing edge of the tip. This flow pattern acts like a "winglet" and increases the loading of the blade at the tip. To capture the details of the tip gap flow, a viscous flow solver with high concentration of grids at the tip region is required as detailed in the work of Brewer et al. [2003].

The details of tip gap region is neither the interest of the present work nor within the capability of inviscid methods. A popular way to deal with the small gap clearance is to connect the tip surface with the duct inner surface artificially. The vortex lattice method code, MPUF-3A, can predict the finite loading at the tip of the blade when an image model is used for a zero percent gap. However, sealing the small gap leads to overprediction of the loading at the blade tip.

If the emphasis is on the hydrodynamic performance of the propeller rather than on the details of the viscous flow inside the gap, a model describing the relation between flow rate and pressure jump through the gap is preferred.

4.2.2 Bernoulli's Obstruction Theory

Bernoulli's obstruction theory was used to model the flow obstruction inside a basic duct in Figure 4.9 (White [1986]). Given the duct diameter D and an obstruction diameter d, the ratio β between D and d is a key parameter:

$$\beta = \frac{d}{D} \tag{4.5}$$

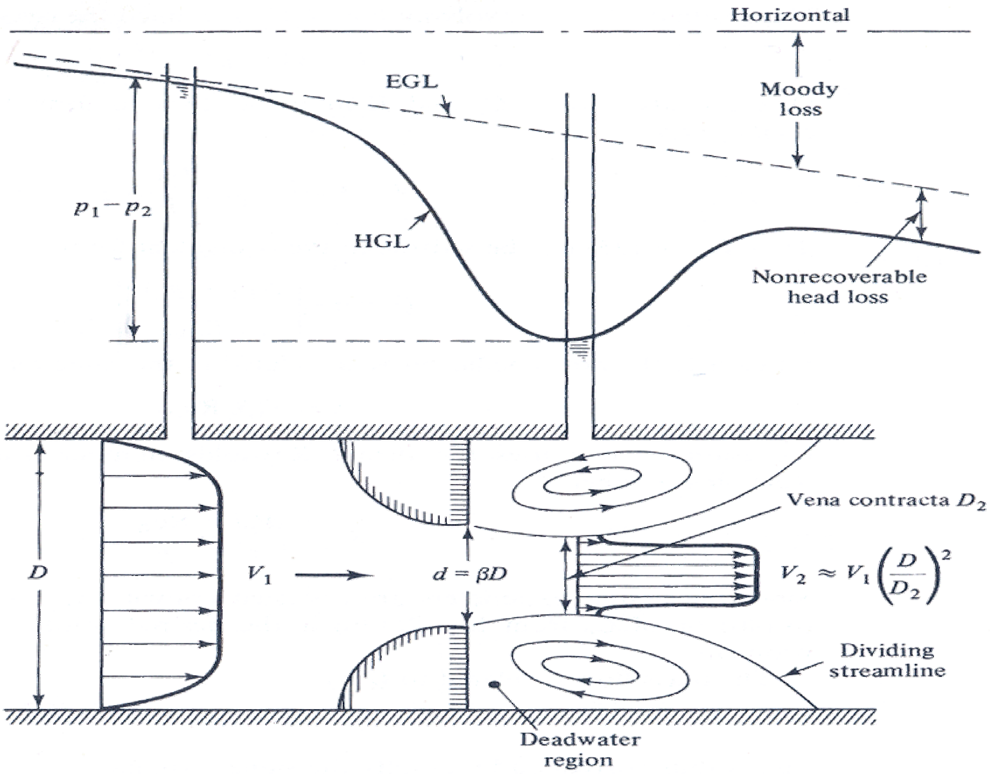

Figure 4.9: Velocity and pressure change through a flow obstruction. Taken from White [1986]

Applying the Bernoulli and continuity equations for incompressible steady frictionless flow, we have

$$Q = \frac{\pi}{4} D^2 V_1 = \frac{\pi}{4} d^2 V_2 \tag{4.6}$$

$$p_0 = p_1 + \frac{1}{2}\rho {V_1}^2 = p_2 + \frac{1}{2}\rho {V_2}^2 \tag{4.7}$$

where V_1 and p_1 are the velocity and pressure before the obstruction respectively. V_2 and p_2 are the velocity and pressure after the obstruction respectively. Eliminating the velocity and expressing the pressure jump as $\Delta p = p_1 - p_2$, the final flow rate is

$$\frac{Q}{A} = V_2 = \sqrt{\frac{2\Delta p}{\rho(1-\beta^4)}} \tag{4.8}$$

where A is the area of the obstruction throat.

Since friction can not be neglected, an empirical discharge coefficient C_Q is introduced. Considering that the gap size is small, we have $1-\beta \approx 1$. So the final relationship between flow rate and pressure jump across the obstruct can be written as:

$$\frac{Q}{A} = C_Q\sqrt{\frac{2\Delta p}{\rho}} \tag{4.9}$$

4.2.3 Numerical Implementation

Kerwin et al. [1987] proposed to treat the gap between duct inner surface and the blade tip as a 2-D orifice. The “orifice equation model” is an application of Bernoulli’s Obstruction theory in 2-D orifice, as shown in Figure 4.10:

$$C_Q = \frac{Q}{h}\sqrt{\frac{\rho}{2\Delta p}} \tag{4.10}$$

After nondimensionalization, the relative gap flow is:

$$\bar{q_R} = C_Q\sqrt{\Delta C_p} \tag{4.11}$$

where $\bar{q_R}$ is the nondimensional relative flow through the gap, defined as $\bar{q_R} = \frac{Q}{hU_\infty}$ and ΔC_p is the difference of pressure coefficients, defined as $\Delta C_p = \frac{\Delta P}{\rho U_\infty^2/2}$.

This model has been successfully coupled with panel methods by Hughes [1997] and Moon et al. [2002], with the discharge coefficient C_Q set as 0.84. This

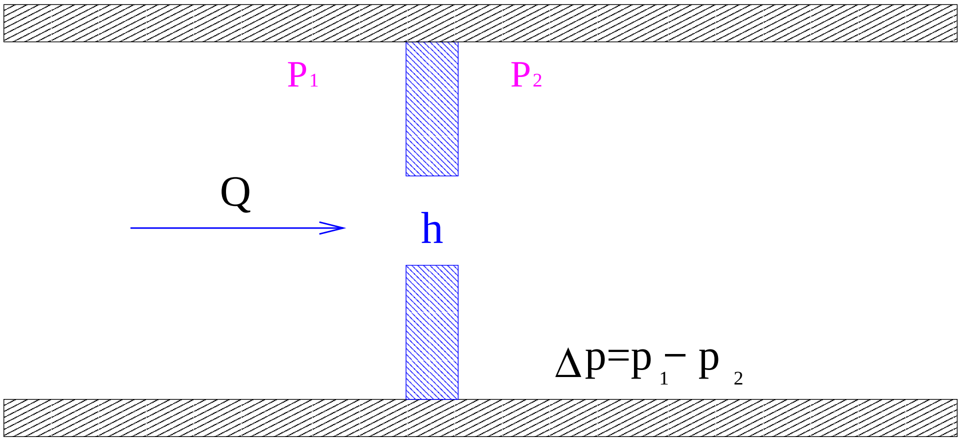

Figure 4.10: Bernoulli's obstruction theory in 2D.

method, added to the current vortex lattice method, is considered to represent correctly the global flow characteristics and the overall influence of the gap on the blade.

To implement this model in MPUF-3A, vortex loops are built inside the gap, which extend from the tip panels of the blade to the duct inner surface. These vortex loops need to continue into the wake, and the corresponding wake panels are called the gap wake panels (or loops). Such a vortex loop arrangement can be seen in Figure 4.11 in 3D, while a more elaborate expanded view of the vortex loop structure is shown in Figure 4.12.

Equation (4.11) is applied on the gap kinematic boundary condition (KBC) points to determines the flow velocities at the gap panels. Since pressure is evalu-

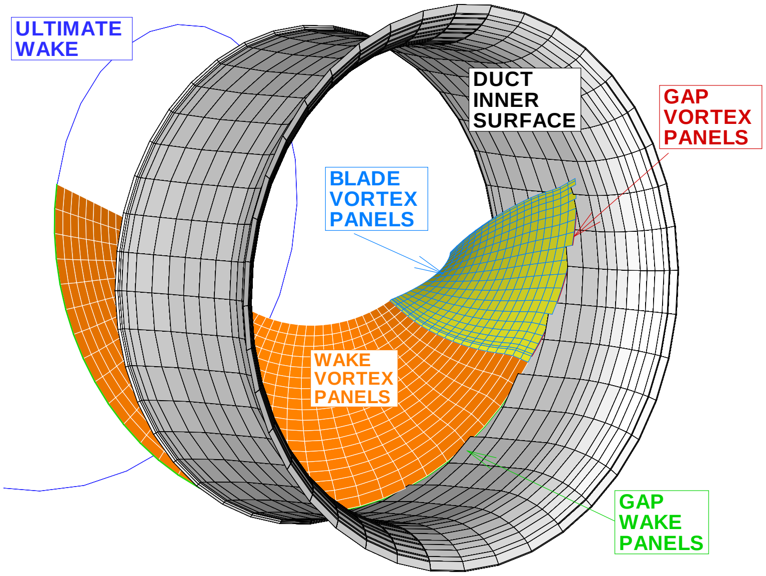

Figure 4.11: Ducted propeller vortex-lattice model with blade, wake and gap vortex loops.

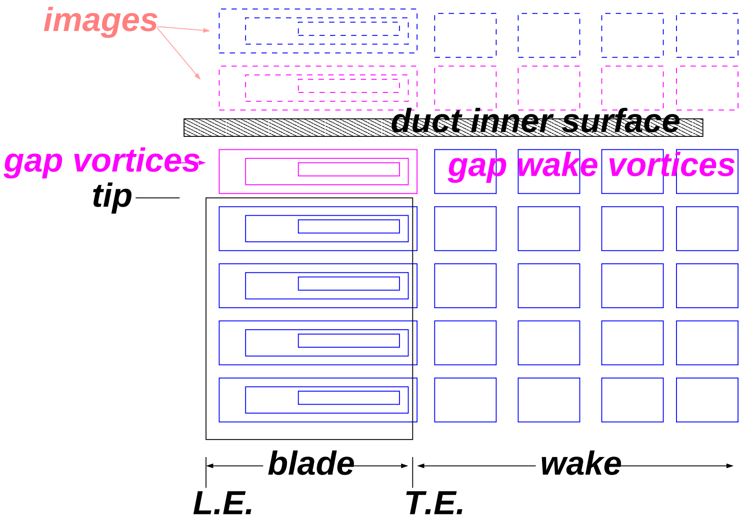

Figure 4.12: Vortex loop structure in the gap model.

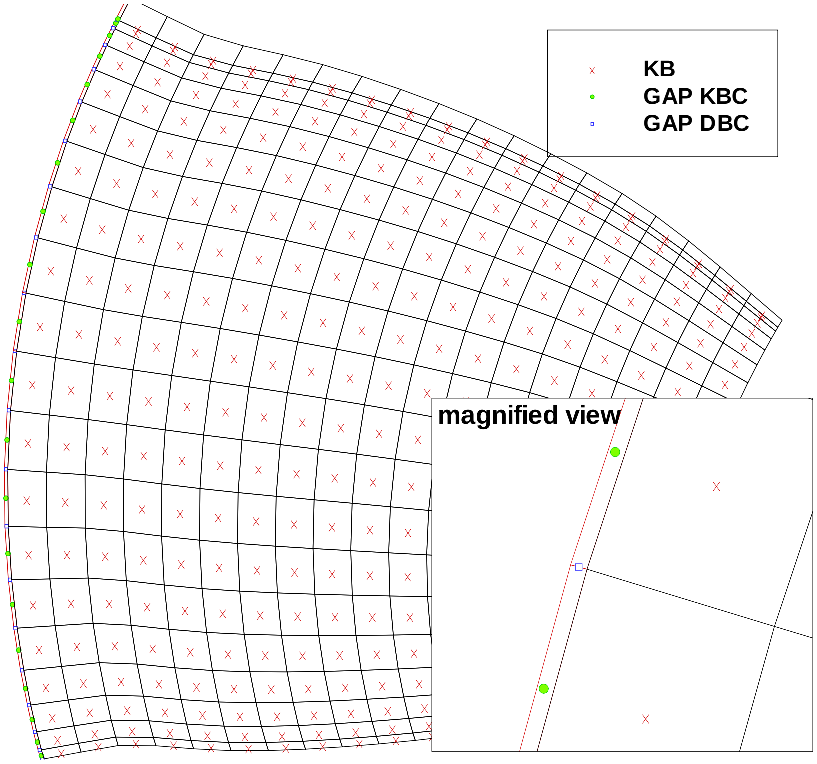

Figure 4.13: Arrangement of control points on the blade and gap panels.

ated only at blade dynamic boundary condition (DBC) points, additional gap DBC points are also introduced. The arrangement of the gap KBC and DBC points is similar to that on the blade panels, as shown in Figure 4.13. In order to determine ΔC_p of Equation (4.11), the pressures on the blade are extrapolated along the spanwise direction to gap DBC points, and then interpolated to get the pressure at the gap KBC points.

The original MPUF-3A version solves for the strengths of the blade vortices by requiring zero normal velocity at the blade KBC points. The kinematic boundary condition equation (3.7), is written in a matrix form as:

$$A \cdot \Gamma = R \tag{4.12}$$

where A is the influence coefficient matrix, which is calculated as the induced normal component of velocity at control points by horseshoe loops of unit strength. R is the RHS of equation (3.7) and Γ is vector of unknown horseshoe strengths.

Since additional horseshoes are distributed inside the gap region, the influence coefficient matrix A is expanded:

$$A' = \begin{bmatrix} A & B \\ C & D \end{bmatrix} \tag{4.13}$$

where A, B, C and D are sub-matrices. Sub-matrix A is same as the original influence matrix in equation (4.12). Sub-matrix B includes the induced normal velocities at control points by the gap horseshoes of unit strength. Sub-matrix C includes the induced normal velocities at gap KBC points by blade horseshoes of unit strength. Sub-matrix D includes the induced normal velocities at gap KBC points by gap horseshoes of unit strength.

The unknown Γ' vector will also expand to include the unknown gap horseshoe strengths, as

$$\Gamma' = \begin{bmatrix} \Gamma \\ \Gamma_{gap} \end{bmatrix} \tag{4.14}$$

where Γ is same as the unknowns in equation (4.12), while Γ_{gap} are the unknown strengths for gap horseshoes.

Kinematic boundary conditions required by Equation (4.11) will be added in the new RHS R':

$$R' = \begin{bmatrix} R \\ R_{gap} \end{bmatrix} \tag{4.15}$$

where R is same as the RHS in equation (4.12), while R_{gap} are the RHS of orifice equation (4.11).

Finally, for the kinematic boundary condition, the linear equation is rewritten as:

$$A' \cdot \Gamma' = R' \tag{4.16}$$

An iterative process is required when applying Equation (4.11), since the value of ΔC_p depends on the propeller loading, and the value of which must be determined as well.

Assessment of Discharge Coefficient

As mentioned before, modeling the details of flow inside the gap region is neither interest of the current work nor within the capability of inviscid model. However, it is still valuable to investigate the gap model with a viscous solver, which could capture the details inside the gap. The justification of discharge coefficient can be made with the viscous model.

The viscous solver FLUENT is applied for this study at this stage. The blade geometry is simplified by using a 3-D rudder like foil. The dimensions and boundaries for the computational domain are shown in Figure 4.14. The computational domain extends from $x = -2$ to $x = +4.0$ in the length direction, $y = -3$ to $y = +3$ in the width direction, and $z = 0$ to $z = 1 + gap$ in the height direction.

The foil section is NACA0010, with a chord length of 1m. The leading edge of of the foil at the bottom is at the origin of the coordinate. The foil is at 3 degrees of angle of attack, and the flow comes from the inlet with a uniform speed of 10 m/s. Gap percentage is defined as the percentage of the height of the foil and a 1% gap stands for a gap clearance $1cm$ for a $1m$ long foil.

The grids on the foil are shown in Figure 4.15, with the magnified view close to the leading edge in Figure 4.16. The grid can be view as stacks of grid with distribution as in Figure 4.17 in the height direction. Along the foil span, 40 layers of hexahedron and wedge cells are created. The gap region contains 30 layers of cells, with about 11,590 cells in each level. There are more than eight million cells inside the whole domain.

A 2D section as in Figure 4.17 is used with inviscid FLUENT model and the pressure on the foil is compared with 2D BEM in Figure 4.18. Some difference occurs in the mid chord region, but the loading are very close between each other.

A segregated implicit 3-D steady solver is used for 3D viscous case.The Reynolds number for the flow, based on the chord length of the foil, is about $Re = 10^7$. The bottom, left and right boundaries, are set to be symmetric boundary. Top of the domain is wall, where no-slip condition is applied for viscous solver, and symmetric for the inviscid case in order to compare with PROPCAV. The no-slip condition is applied on the foil surfaces for viscous calculation. The circulation is compared between FLUENT and these of BEM inviscid cases in Figure 4.19. The values are close below $z = 0.7$, above that, the loading on the foil in FLUENT is maintained until $z = 0.9$ and then drops to zero rapidly. The BEM predicts a

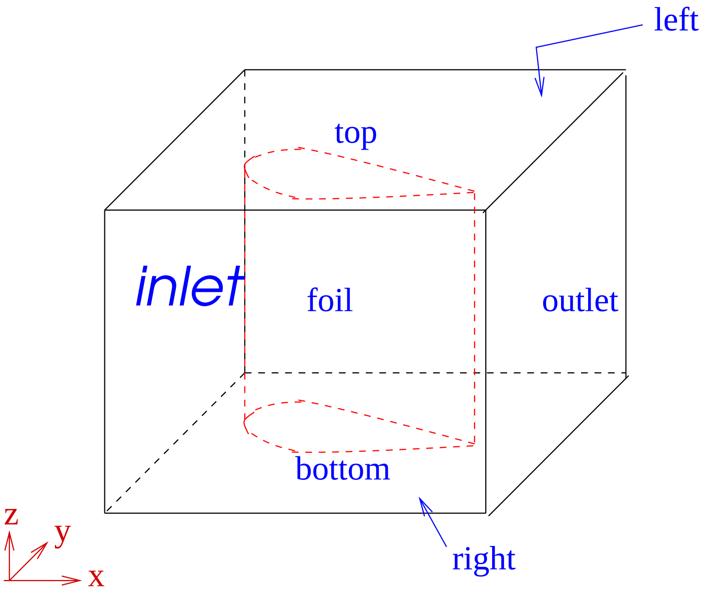

Figure 4.14: Dimensions and boundaries for a 3-D foil case.

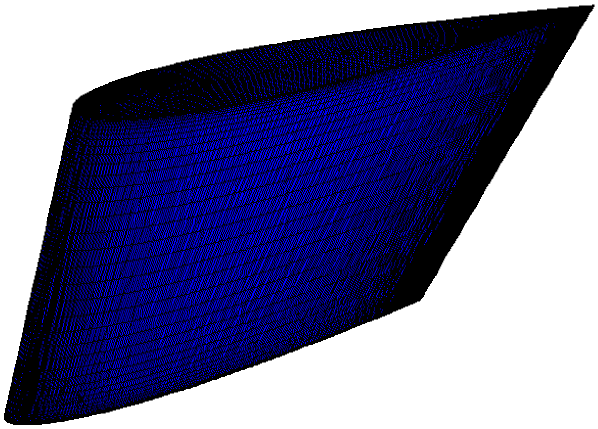

Figure 4.15: Grid on the foil.

loading close to a parabolic forms.

Grid dependency studies are performed for the viscous 1% gap case. The first arrangement is that 50 layers on the foil and 20 layers inside the gap; the second arrangement is that 40 layers of the foil and 30 layers inside the gap. The circulation distribution along the foil does not change much with the different arrangement, as shown in Figure 4.20.

The viscous model is chosen as a seven equation Reynolds Stress model. The y^+ on the foil for the 1% gap case are limited to be below 200, as shown in Figure 4.21. The streamlines close to the gap region are shown in Figure 4.22 and 4.23, where the leakage vortices can be observed. The circulation distribution along the foil is shown in Figure 4.24. The circulation Γ_{foil} is nondimensionalized as:

$$\Gamma_{foil} = \frac{\hat{\Gamma}_{foil}}{uc} \tag{4.17}$$

where u is the dimensional inflow velocity and c is the dimensional chord length of 3d foil. The dimensional circulation is defined as

$$\hat{\Gamma}_{foil} = \oint_a \vec{q} \cdot ds \tag{4.18}$$

where a is the closed path. As expected, the loading of the foil decreases as the gap size increases.

The following parameters are defined: discharge coefficient $C_Q = \frac{Q}{h}\sqrt{\frac{\rho}{2\Delta P}}$ and ratio between flow rate and pressure difference $R = \frac{Q}{\Delta P}$.

Figure 4.25 shows the locations for evaluating flow rate and pressure. Ten equally spaced quadrilateral sections along the noise-tail line are created, and the

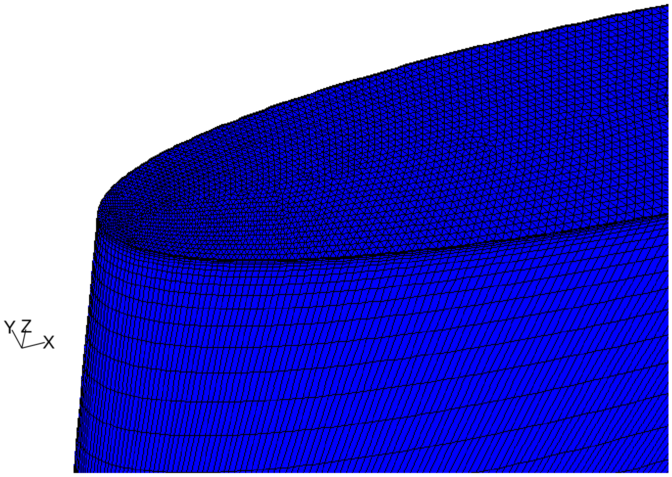

Figure 4.16: Magnified view of grid at the leading edge.

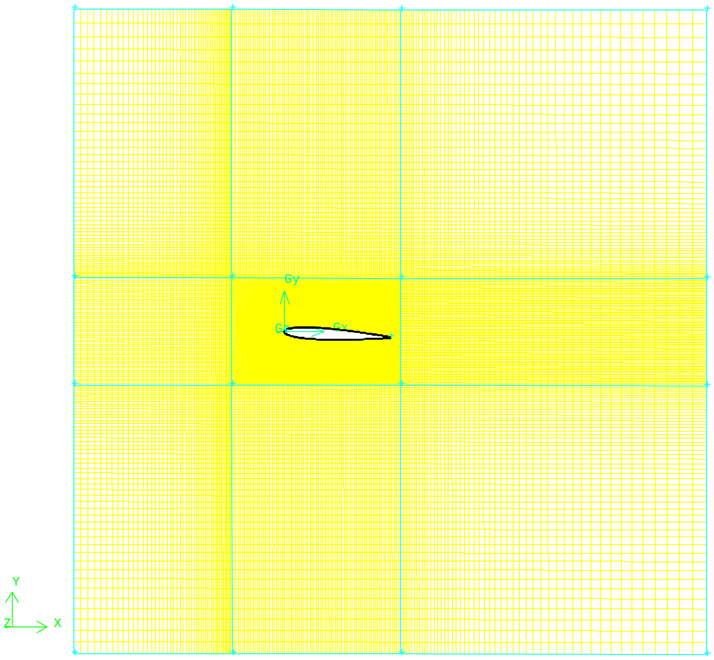

Figure 4.17: A typical horizontal section of the computation domain, which cuts with the foil.

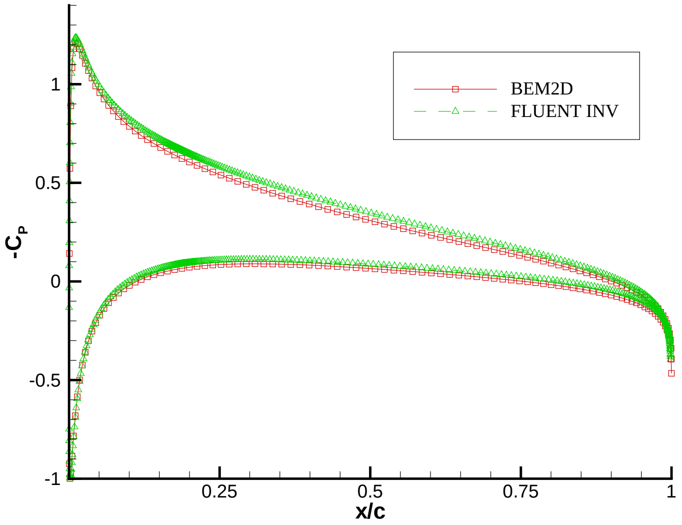

Figure 4.18: Comparison of inviscid C_P on the foil with BEM 2D.

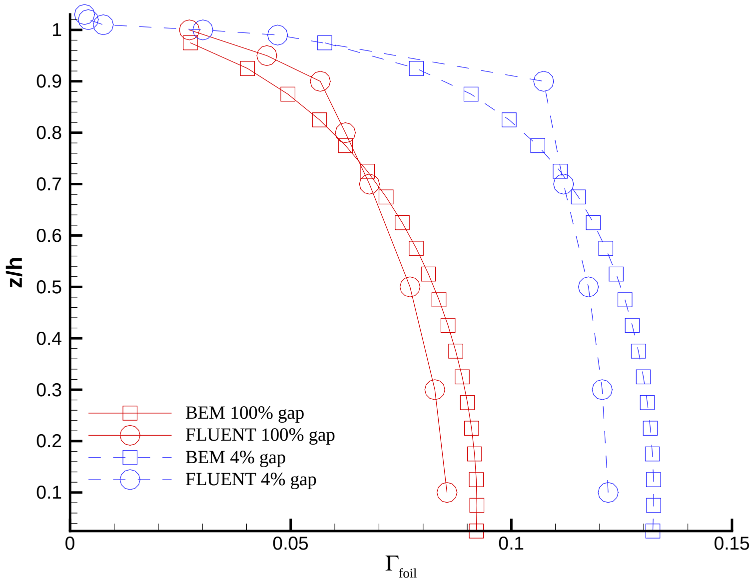

Figure 4.19: Comparison of inviscid circulation distribution for 100% gap and 4% gap cases for BEM and viscous circulation distribution for FLUENT.

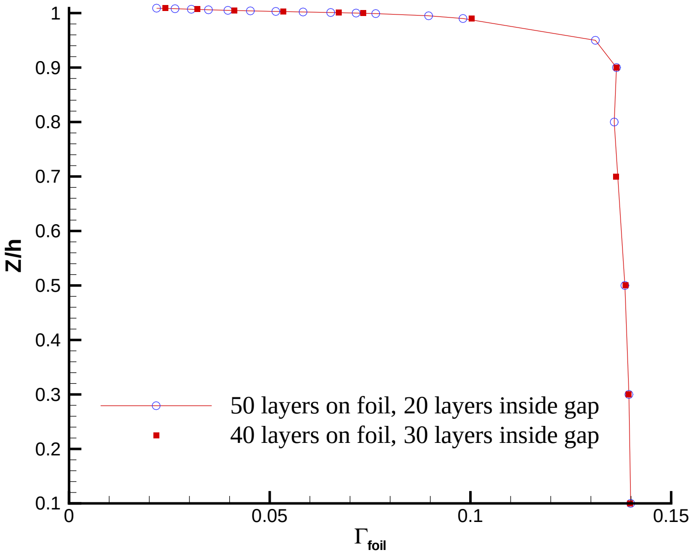

Figure 4.20: Convergence of circulation distribution for viscous 1% gap case.

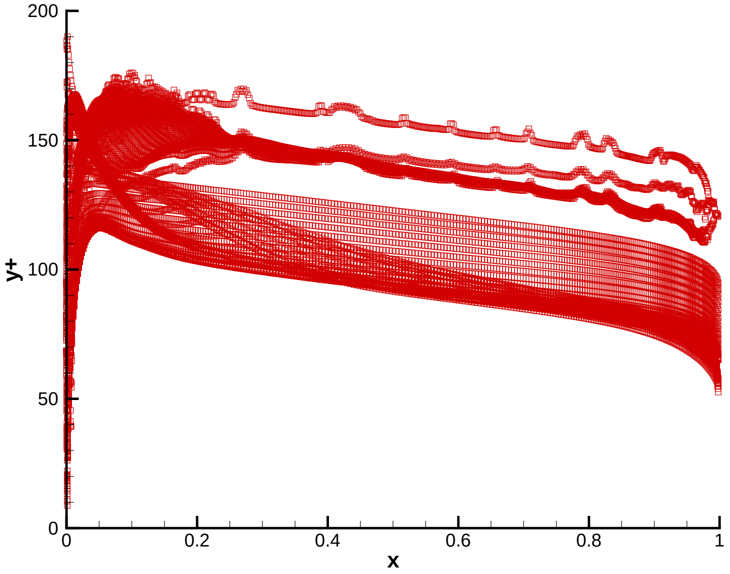

Figure 4.21: y^+ on the foil (including the top of the foil inside the gap region) for the 1% gap case

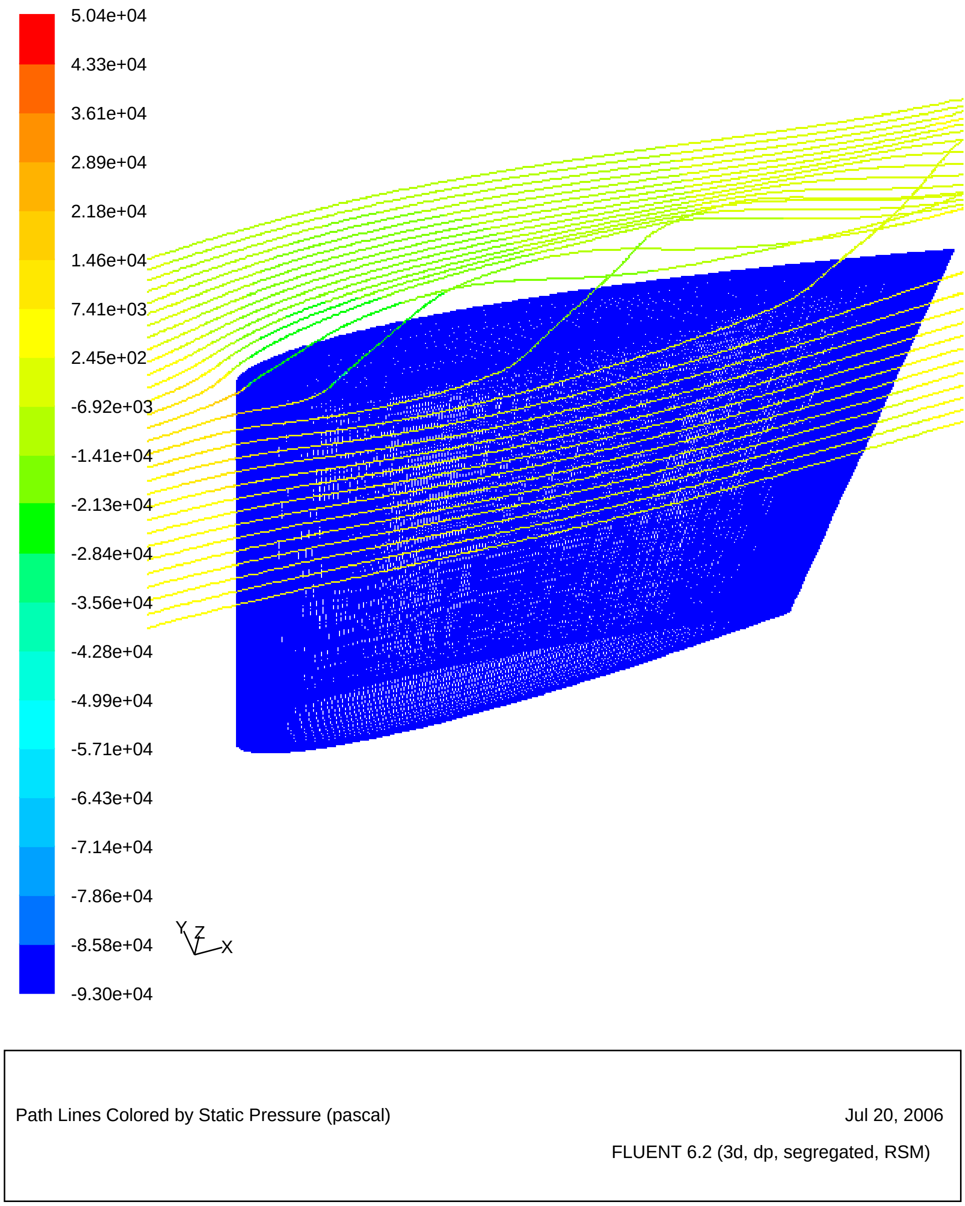

Figure 4.22: Streamlines in the vicinity of the 1% gap, colored by pressure.

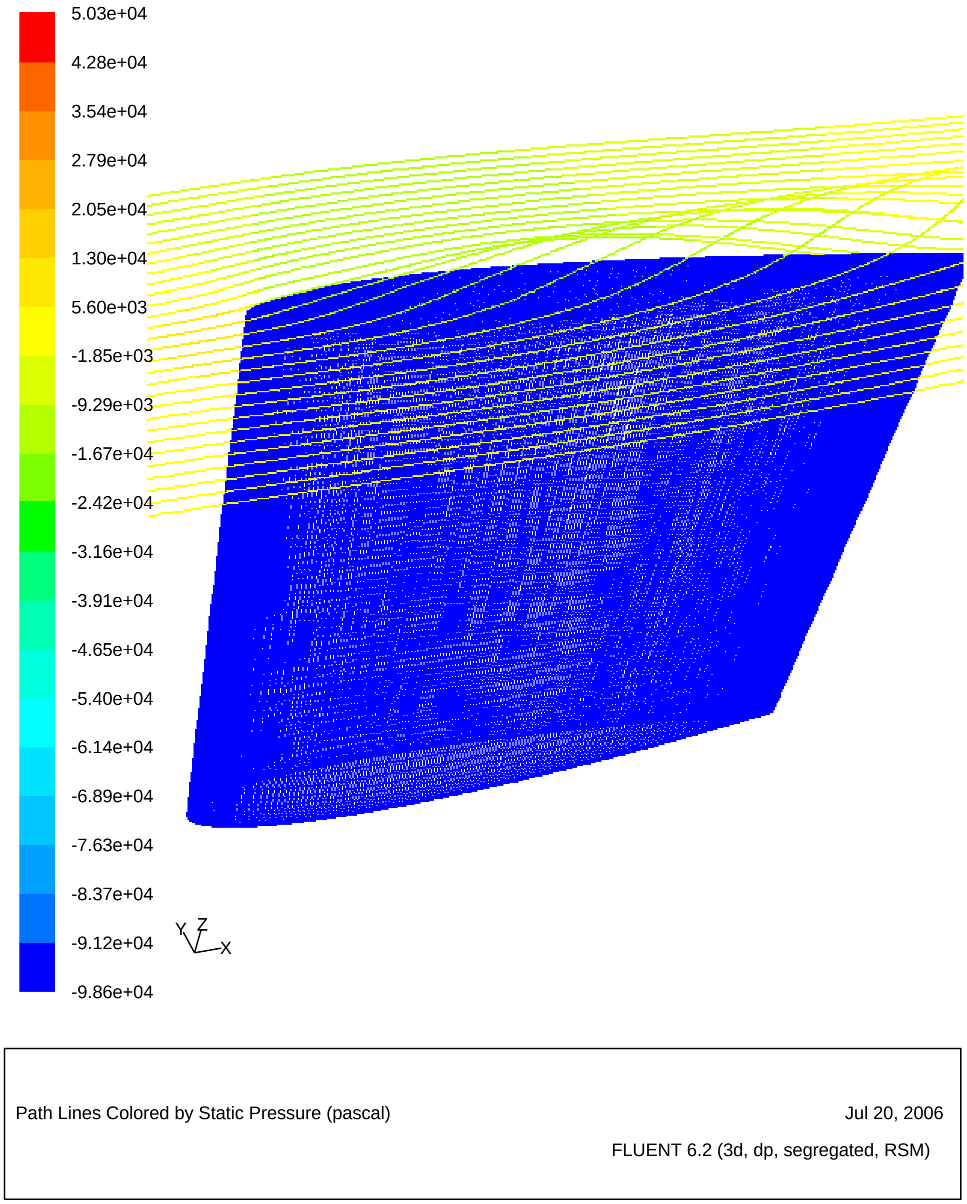

Figure 4.23: Streamlines in the vicinity of the 4% gap, colored by pressure.

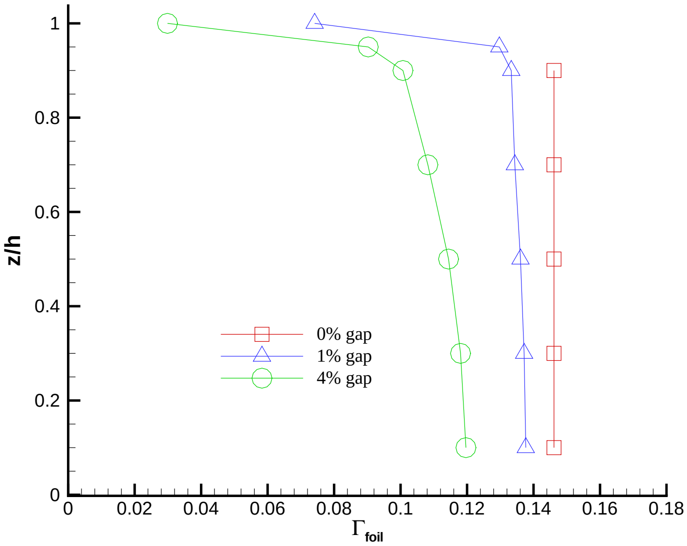

Figure 4.24: Circulation distribution along the foil for viscous 0%, 1% and 4% gap cases.

flow rates are evaluated on each of them. The pressure differences are measured across the gap for each section.

The calculated values of C_Q and R for both 1% and 4% gap cases are listed in Table 4.1. For both cases, the discharge coefficients are close to 1.0 for most sections, especially at the front part of the foil. The higher discharge coefficients at the aft part of the foil might be attributed to leakage vortices. Notice the C_Q values in Table 4.1 are higher than 0.84, which is recommended by Hughes [1997] and Moon et al. [2002].

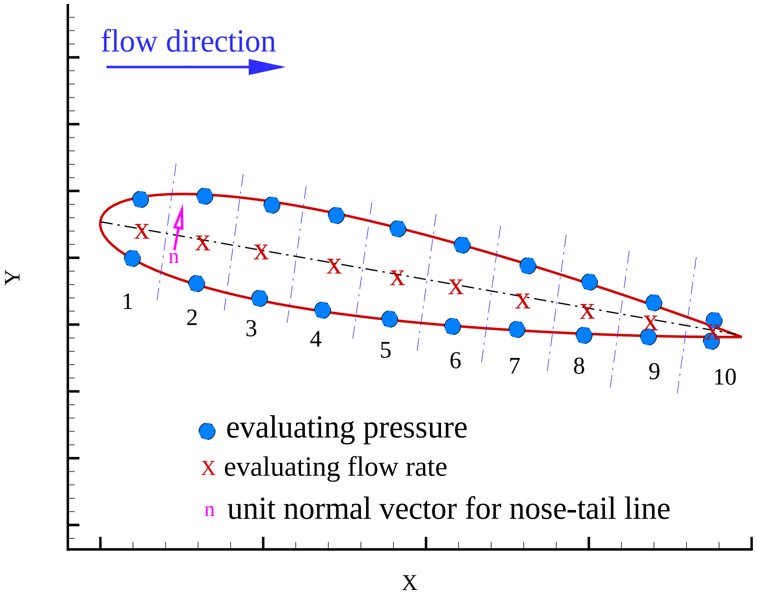

Figure 4.25: Locations where flow rate and pressure are evaluated.

	1% gap		4% gap	
section	R	C_Q	R	C_Q
1	3.76E-7	0.70	2.00E-6	0.75
2	2.54E-7	0.60	2.75E-6	0.95
3	2.75E-7	0.65	3.43E-6	1.12
4	3.16E-7	0.73	3.73E-6	1.22
5	4.09E-7	0.86	3.88E-6	1.28
6	6.47E-6	1.10	3.75E-6	1.29
7	1.18E-6	1.49	3.81E-6	1.33
8	2.63E-6	2.20	4.13E-6	1.39
9	4.60E-6	2.81	4.51E-6	1.44
10	3.88E-5	2.32	8.26E-5	1.83

Table 4.1: Evaluation of flow rate/pressure difference ratios and discharge coefficients.

4.2.4 Numerical Results

To validate the gap model and study its effect on blade loading, a Ka 4-70 Wageningen B-screw Series propeller with nozzle 19A is considered. The geometry of the duct and the propeller body forces are shown in Figure 4.26. The propeller is a four bladed propeller with a pitch ratio of $P/D = 1.0$ at $r = 0.7R$. The duct has an extended flat (cylindrical) inner surface. The propeller is subject to uniform inflow at an advance ratio of $J_s = 0.55$, and the gap is 0.38% of the radius of the inner duct at the propeller plane.

As discussed in Chapter 4.2.3, the pressure on the gap DBC points are extrapolated from pressure on the blade DBC points. At the mid-chord, such an extrapolation is shown in Figure 4.27.

A convergence study of circulation distribution using the modified MPUF-3A version with various spanwise discretization is shown in Figure 4.28. The predicted circulations using the original MPUF-3A version, without the gap model (both the current and original models have the image model implemented), are shown in the same figure. The expected increase in the loading with the gap model is evident.

Figure 4.29 shows the convergence study with gap percentages. As expected, the loading decreases as the gap percentage increases. Note that the circulation for the 0.38% gap is very close to that for the zero gap.

In the case of 1% gap, the effect of C_Q is shown in Figure 4.30. When $C_Q = 0$, the gap is actually sealed (since no flow rate inside the gap then) and the

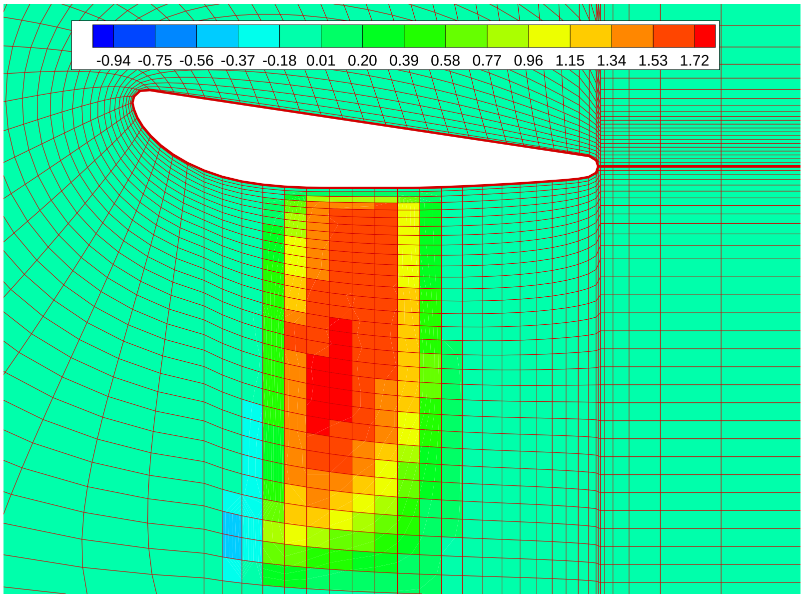

Figure 4.26: Body forces (GBFLOW) of Ka 4-70 propeller inside the nozzle 19A.

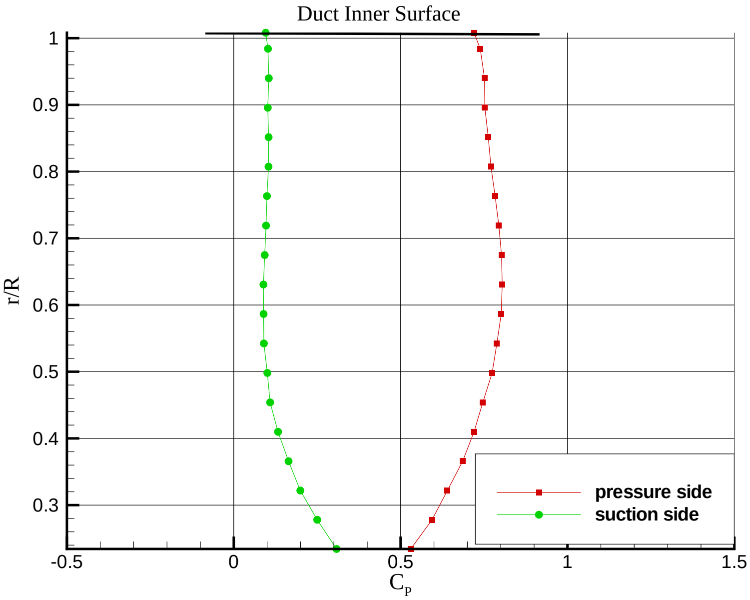

Figure 4.27: Pressure distributions on two sides of the blade along the mid-chord panel and extrapolation inside the gap.

loading is the highest. As C_Q increases, the loading decreases quickly at the tip. Thus, the value of C_Q can be a very critical parameter in determining the loading at the propeller tip. When the gap size is reduced to 0.38%, the effect of C_Q on circulation distribution is shown in Figure 4.31. It is shown that the influence of C_Q is relatively smaller, comparing to the 1% gap case.

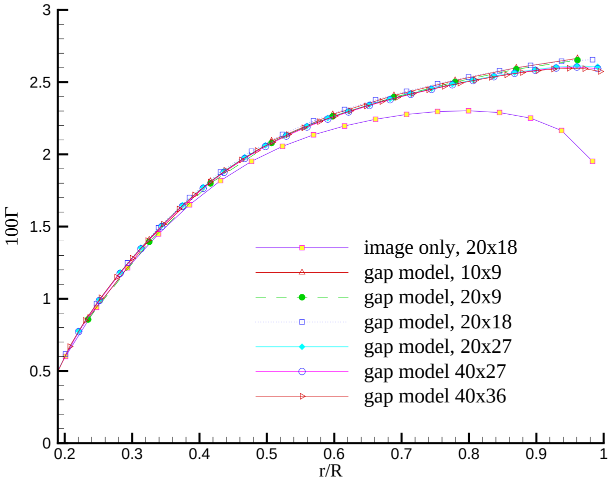

Figure 4.28: Convergence study of predicted circulation with number of spanwise elements.

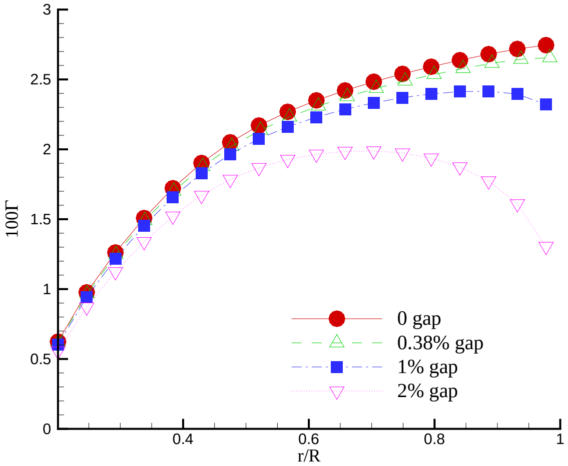

Figure 4.29: Effect of the gap percentage on the predicted circulation, $C_Q = 0.85$

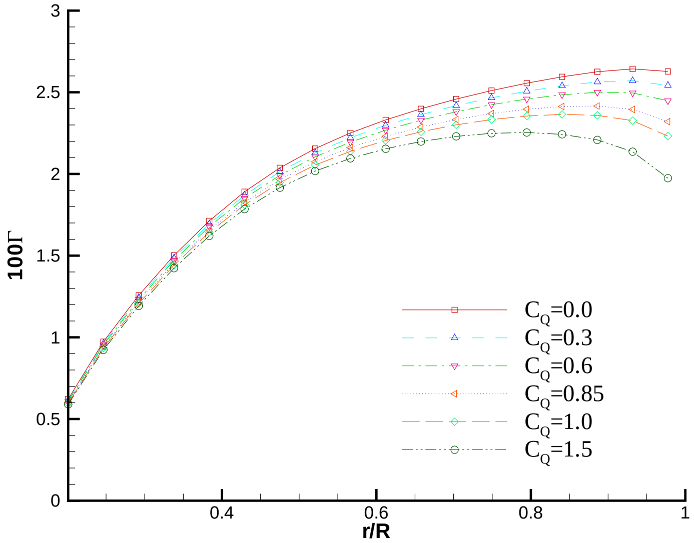

Figure 4.30: Effect of C_Q on the predicted circulation for 1% gap

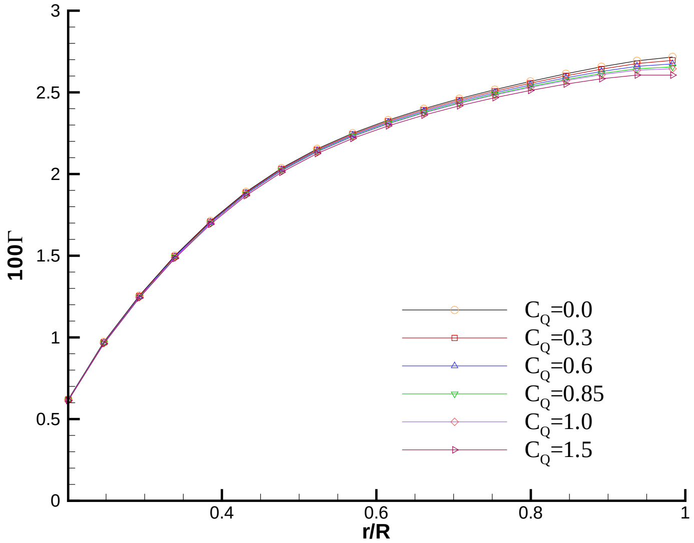

Figure 4.31: Effect of C_Q on the predicted circulation for 0.38% gap

Chapter 5

Effective Velocity and Effective Pressure

In this chapter, some approaches of improving the accuracy of the effective velocity predictions are presented. In the case of ducted propellers, an effective pressure term is introduced to satisfy the Bernoulli equation. The numerical schemes and formulations are described and validated.

5.1 Effective Velocity

Evaluation of the effective velocity is critical in the prediction of correct propeller performance and cavity extent. Approaches to increase the accuracy of the effective velocity are addressed in the following sections.

5.1.1 Previous Method: A Straight Effective Velocity Plane

In the work of Choi [2000], the effective velocities are evaluated at a straight plane ahead of the propeller leading edge, as shown in Figure 5.1. The effective velocity plane contains the selective field points where the subtraction between total velocities and induced velocities are performed. The axial location of the plane is determined so that it is the closest straight plane ahead of the propeller leading edge. The radial location of these selective points are coincident with chosen grid points.

After the propeller solution is obtained, the propeller induced potential can be calculated by a complete set of singularities, as:

$$\phi_p = \sum_{\Gamma} \Gamma \phi_\Gamma + \sum_{Q_B} Q_B \phi_{Q_B} + \sum_{Q_C} Q_C \phi_{Q_C} \tag{5.1}$$

where Γ is the strength of each vortex horseshoe, Q_B is the strength of each line source representing blade thickness, and Q_C is the strength of the each line source representing cavity thickness. ϕ_Γ, ϕ_{Q_B} and ϕ_{Q_C} are the induced potential at the field location by vortex horseshoe, the line source for blade thickness and the line source for cavity thickness respectively, of unit strength. However, it was found that numerical errors were introduced when the thickness effects were included in the induced velocity calculation. As a result, only the first term in the RHS of equation (5.1) is used to calculate the induced potentials.

The induced velocities at field points are calculated by numerically differentiating the induced potentials. For the axisymmetric case, the induced velocity is both averaged in time and circumferentially. For the non-axisymmetric case, the induced velocity is averaged in time only.

Using a straight effective velocity plane is accurate for open propellers with simple geometries. Choi [2000] found that the effective wake did not vary significantly between 0.2 to 0.4 radii in front of propeller. He also studied the effects of axial grid resolution, circumferential grid resolution and artificial dissipation on the effective velocity evaluation. However, only simple propeller geometries, like N4148 with zero rake and zero skew) were used in his numerical study.

The accuracy is deteriorated during the following situations: (1) the blades have relatively large skew and/or rake. (2) Velocity gradient near the propeller LE is large. For a ducted propeller, the velocity gradient inside the duct can be reasonably high. As a result, it is important to seek a more accurate way to evaluate the effective velocity.

5.1.2 A Direct Way: Effective Vectors at Blade Control Points

Instead of evaluating velocities in a plane ahead of the propeller, it is of interest whether the effective velocities could be calculated directly at the control points where kinematic boundary conditions apply. This approach is shown in Figure 5.2.

In this method, the total velocity vector $\vec{q_t}$ is interpolated at each control point, and the propeller induced velocity vector $\vec{q_i}$ is evaluated directly at the same location. The effective velocity vector $\vec{q_e}$ at the control point is determined by subtracting the induced velocity vector from the total velocity vector:

$$\vec{q_e} = \vec{q_t} - \vec{q_i} \tag{5.2}$$

The total velocity distribution on the whole flow domain is predicted by the finite volume method based Euler solver, GBFLOW. An inverse distance interpolation scheme, introduced by Shepard [1968], is applied to interpolate the total velocity at the control points.

As shown in Figure 5.3, a given control point is located inside a GBFLOW cell with n vertices. The distance between the control point and one vertex of the

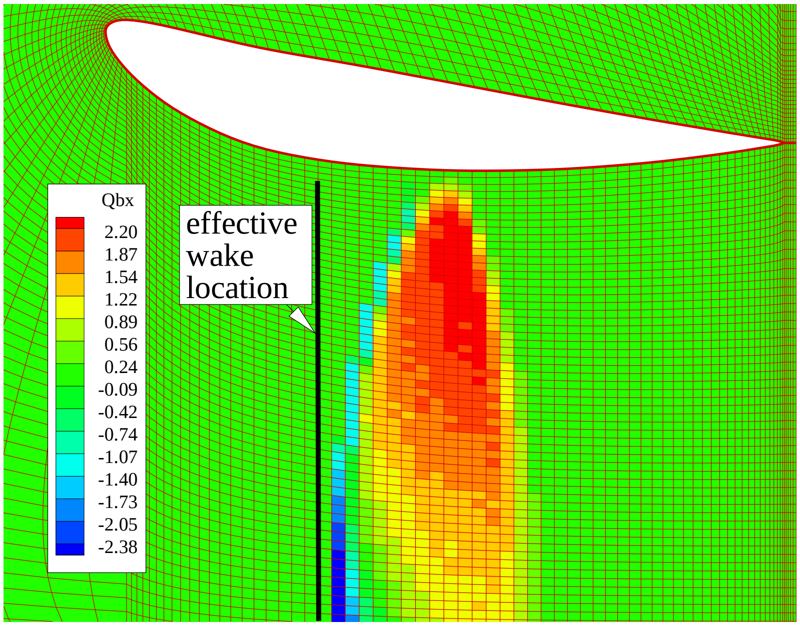

Figure 5.1: A straight plane is used to predict the effective velocities in front of the leading edge.

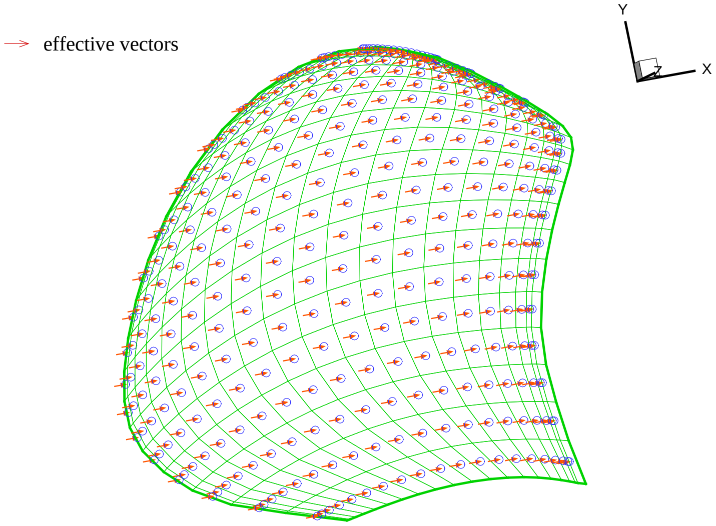

Figure 5.2: Effective velocity vectors are evaluated directly at the blade control points.

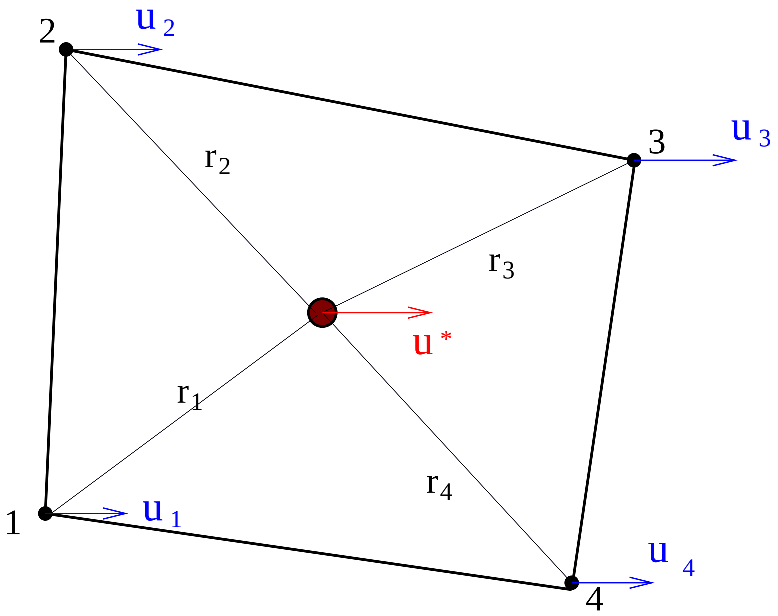

Figure 5.3: Inverse distance interpolation for velocity at a control point inside a GBFLOW cell.

GBFLOW cell is r_i. The total velocity on vertices are u_i. The velocity u^* at the control point is then given by the inverse distance interpolation scheme as:

$$u^* = \frac{\sum_1^n \frac{u_i}{r_i^2}}{\sum_1^n \frac{1}{r_i^2}} \tag{5.3}$$

The total velocity vectors are interpolated at the blade control points of a N4148 propeller. The advance ratio is $J = 0.8$ and the blade is discretized into 20x18 panels in MPUF-3A. The interpolated velocities on blade control points are plotted against the total flow field are shown in Figure 5.4.

To calculate the induced velocity, each control point is rotated in the circumferential direction to obtain a set of field points, as shown in Figure 5.5. Potentials or velocities are evaluated at these field points. In the case of axisymmetric flow,

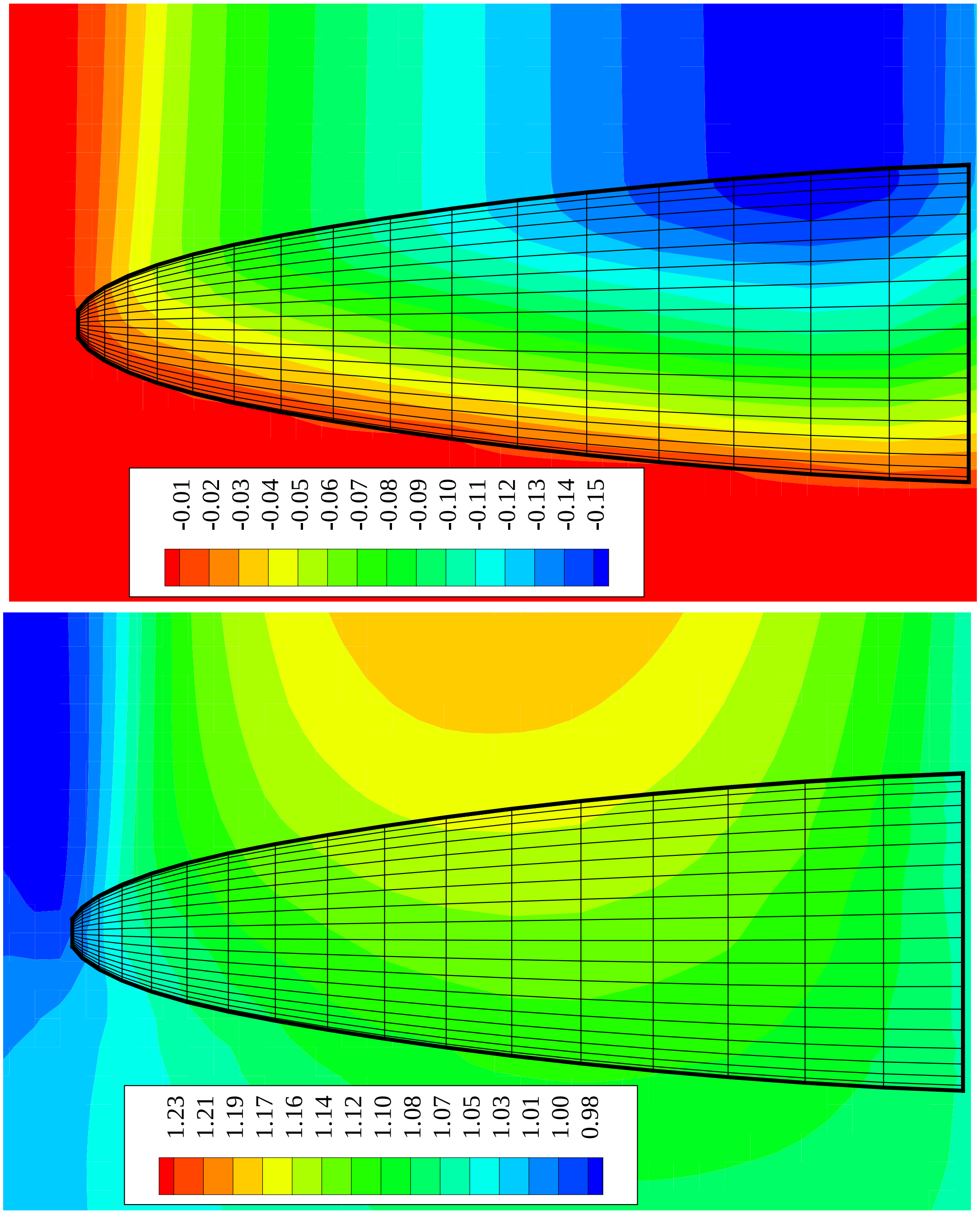

Figure 5.4: Interpolated velocities at control points of N4148 propeller, with the flow filed in GBFLOW as background. (left) axial velocities (right) tangential velocities.

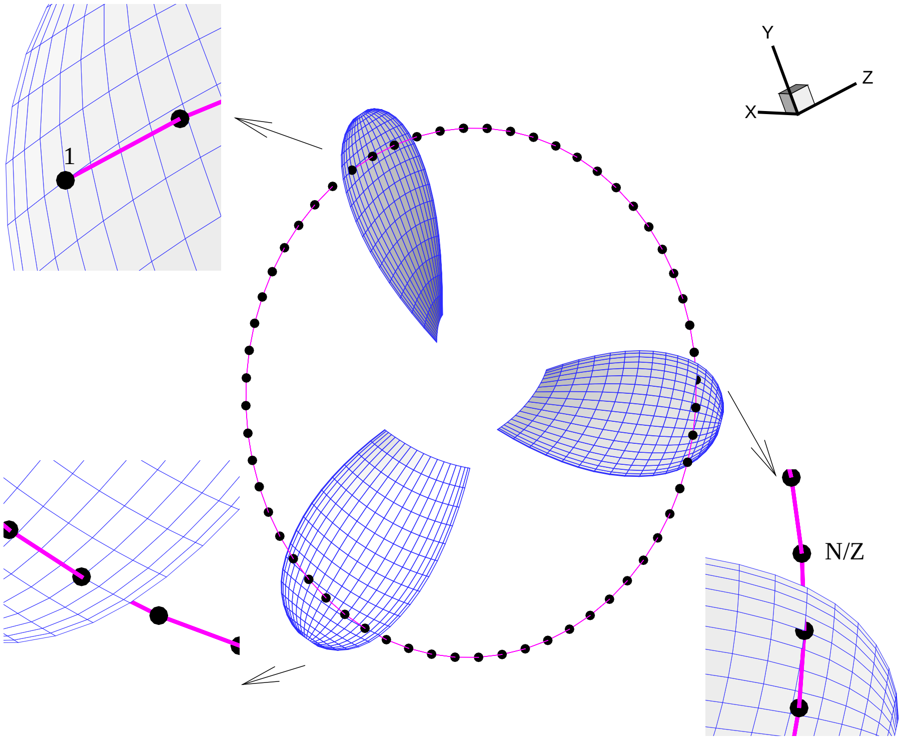

Figure 5.5: Spatial locations for induce velocity evaluation for a control point.

the propeller induced velocities are time averaged and circumferentially averaged. If the circumferential point number is N, and the propeller consists of Z blades, then only the potentials on the first $\frac{N}{Z}$ points are necessary, since the potentials and velocities will repeat on the remaining points.

To validate this approach, a propeller N4148 subject to a uniform inflow is considered. Since the inflow contains no vorticity, the interaction velocity between propeller and inflow is zero. The effective velocity is then the nominal velocity itself.

The contours of total axial velocity, induced axial velocity and effective axial velocity on blade control points are shown in Figure 5.6. Even though the contours of the induced velocity and the total velocity looks quite similar, the maximum error in the effective velocities is 3%, higher than the 1% error when the effective velocity is predicted on the straight plane in Choi [2000].

The original version of MPUF-3A used wake harmonics to obtain the inflow information, and interpolated at all the control points to get local inflow component in equation (3.5). In the current approach, the velocity vectors can be used directly at the control points. Figure 5.7 shows the circulation distribution along the spanwise direction when the effective vectors are used in the RHS of equation (3.5). This circulation distribution compares well with that of the case when uniform wake harmonics are used as inflow, even though the effective velocity contains 3% error.

Further validations are performed on P1452 and N3745. Comparing with N4148, P1452 is a propeller with skew, and N3745 is a propeller with finite tip. At advance ratio of $J_s = 0.6$, the contours of axial velocities on control points are shown in Figure 5.8. The errors increase to the level between -13% to 3%. The distribution of circulation is compared with MPUF3A with wake harmonics, PROPCAV and GBFLOW/MPUF3A with curved effective wake (details in the following section) in Figure 5.9. The effective vector approach is very close to MPUF3A and MPUF3A/GBFLOW, except for some difference in the mid-span. For N3745, the contours of axial velocities on blade control points are shown in Figure 5.10. The errors are even higher, but limited to the blade tip region. The distribution of circulation is again compared with the numerical methods used in the previous case, as shown in Figure 5.11. The major difference of effective vector approach exists in

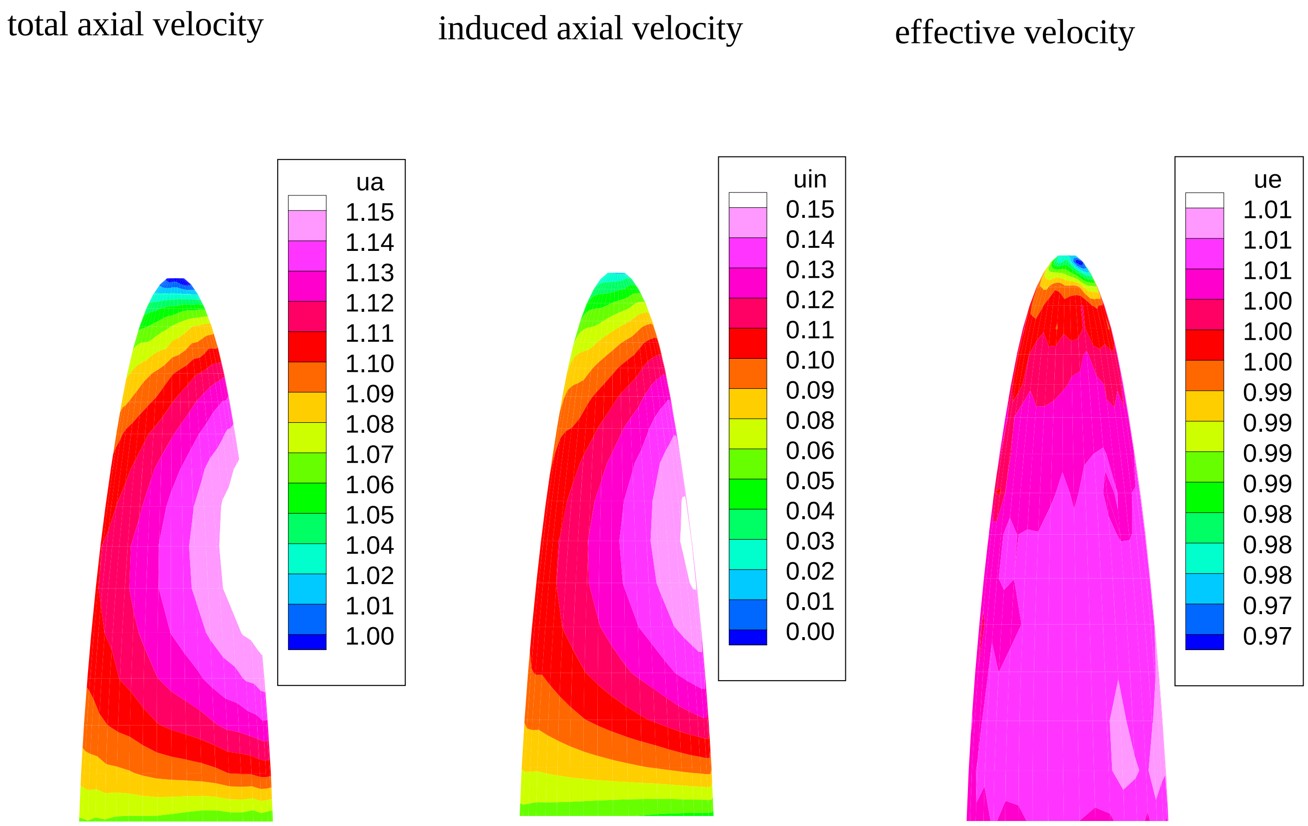

Figure 5.6: Contours of total axial velocity (left), induced axial velocity (mid) and effective axial velocity for N4148 propeller via the effective vector approach.

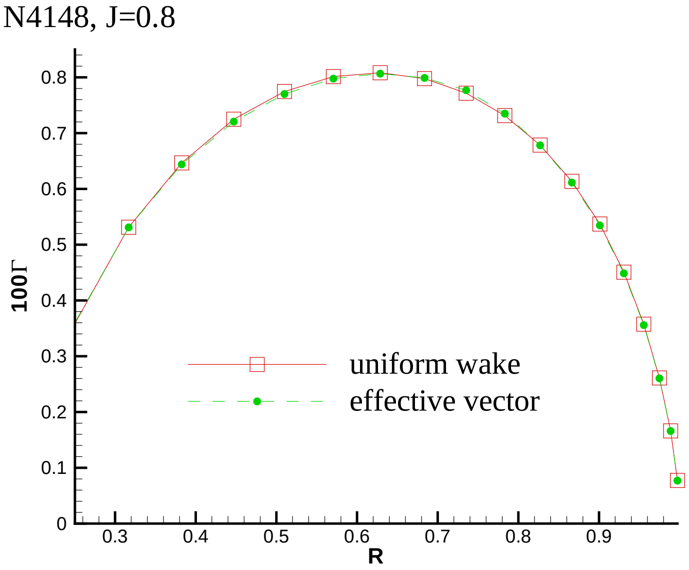

Figure 5.7: Circulation distribution along the spanwise direction for N4148 propeller, compared between the uniform wake approach and effective vector approach.

the mid-span, but it is still inside acceptable level.

However, there are two major difficulties in this direct approach: (1) when duct and hub are included, more errors are introduced, and (2) longer computational time, since all the control points need to be included. For a three bladed propeller and discretized as 20×18 panels, the previous approach will evaluate potentials on totally $15 \times 60/3 = 300$ points, if the straight plane includes 15 radial points and 60 circumferential points. For the current approach, the field points increases to $360 \times 60/3 = 7200$, since there are $20 \times 18 = 360$ control points in total. The direct approach requires 24 times the computational effort.

5.1.3 A Compromise: A Curved Effective Velocity Plane

An alternative way is to evaluate the effective velocity at a plane which is curved rather than straight. Strictly speaking, the curved plane is located a cell in front of the blade LE along the entire span, as shown in Figure 5.12.

This method is again validated with a propeller, N4148, subject to uniform inflow. The total velocity, induced velocity and effective velocity are shown in Figure 5.13. It is found that the uniform effective velocity is recovered using this approach.

In the study of ducted propellers, the curved plane in front of the blade LE will be chosen for the effective velocity calculation instead of a straight plane due to the following advantages: (1) comparable computational efforts (2) velocity evaluated at the nearest plane to the propeller to improve the accuracy.

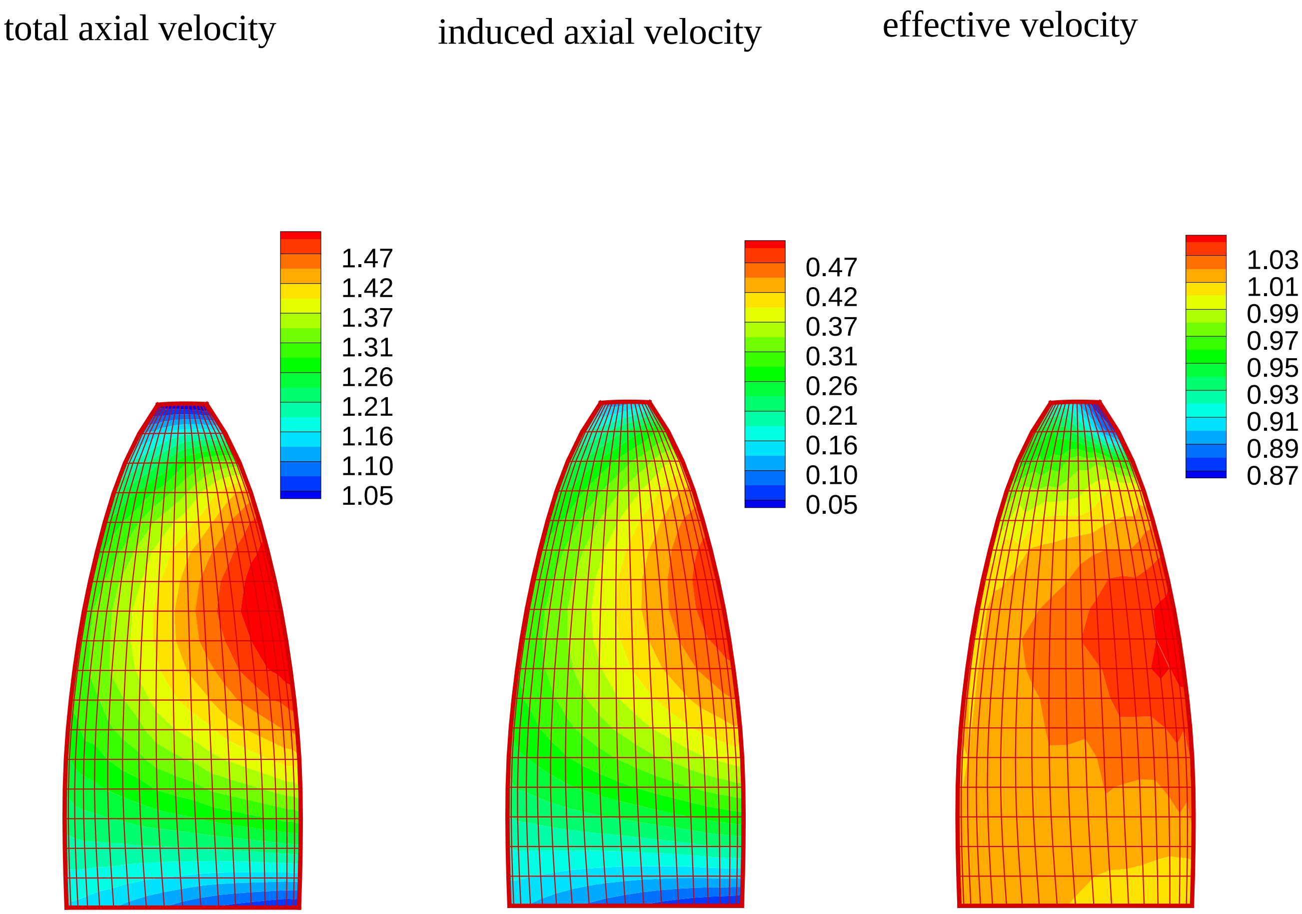
total axial velocity

induced axial velocity

effective velocity

Figure 5.8: Contours of total axial velocity (left), induced axial velocity (mid) and effective axial velocity for P1452 propeller via the effective vector approach.

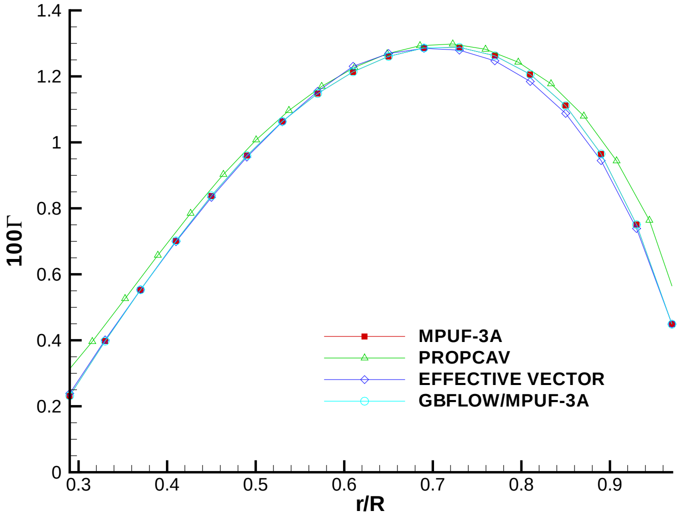

Figure 5.9: Circulation distribution along the spanwise direction for P1452 propeller, compared between effective vector approach, MPUF-3A, GBFLOW/MPUF-3A and PROPCAV

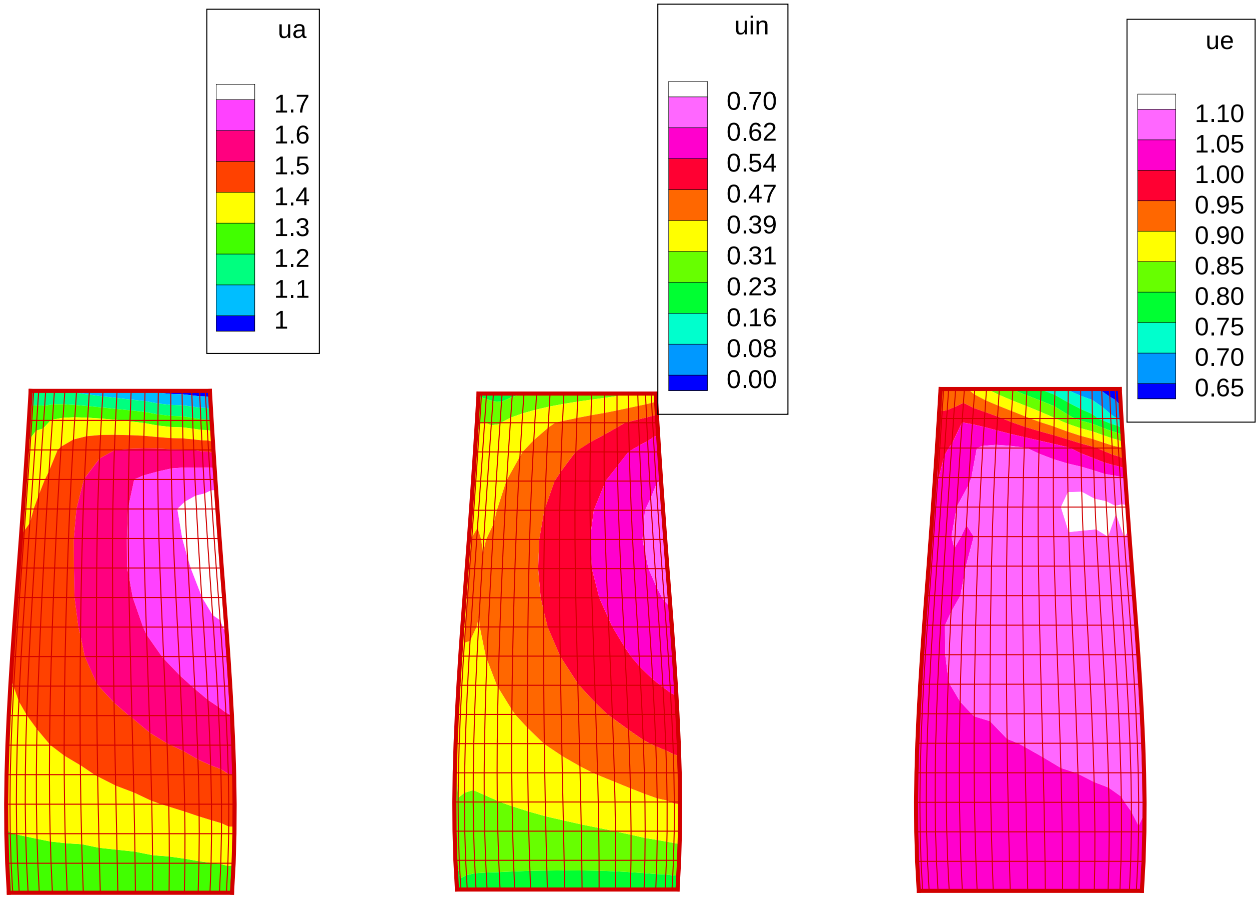

total axial velocity

induced axial velocity

effective velocity

Figure 5.10: Contours of total axial velocity (left), induced axial velocity (mid) and effective axial velocity for N3745 propeller via the effective vector approach.

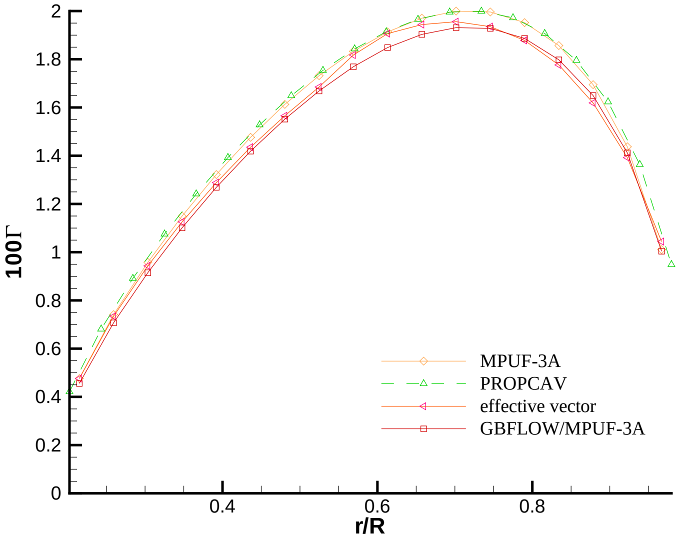

Figure 5.11: Circulation distribution along the spanwise direction for N3745 propeller, compared between effective vector approach, MPUF-3A, GBFLOW/MPUF-3A and PROPCAV

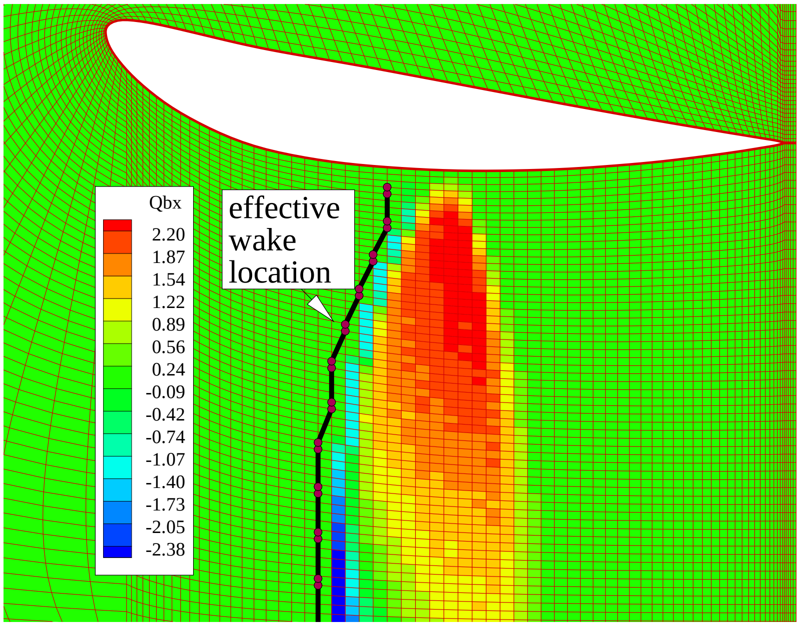

Figure 5.12: A curved plane ahead of the leading edge is used to evaluate the effective velocities.

5.2 Effective Pressure

Kinnas [2006] examined the Bernoulli equation for propeller flows under five different situations: (1) uniform inflow at zero angle with the propeller axis (2) uniform inflow at an angle α with propeller axis (3) non-uniform axisymmetric inflow (4) ducted propeller in uniform inflow (5) propeller in non-axisymmetric (vortical) inflow. A concept of "effective pressure" is introduced to satisfy the Bernoulli equation. For the completeness of the current research, the formulation are included here:

Velocity decomposition in front of a right handed propeller with rotational velocity ω is shown in Figure 5.14. The total velocity, based on the ship-fixed system $(x_{ship}, y_{ship}, z_{ship})$ can be decomposed as the effective velocity q_E, the rotation velocity $-\omega \times r$ and the induced velocity expressed as gradient of perturbation potential based on propeller-fixed system $(x_{prop}, y_{prop}, z_{prop})$.

$$\vec{q} = \vec{q_E} - \vec{\omega} \times \vec{r} + \vec{\nabla}\phi \tag{5.4}$$

The effective velocity based on the propeller-fixed system can be expressed as

$$\vec{q_e} = \vec{q_E} - \vec{\omega} \times \vec{r} \tag{5.5}$$

Perturbation potential in equation (5.4) is determined by the Vortex Lattice Method by satisfying the kinematic boundary condition on the blade control points.

$$\frac{\partial \phi}{\partial n} = -\vec{q_e} \cdot \vec{n} \tag{5.6}$$

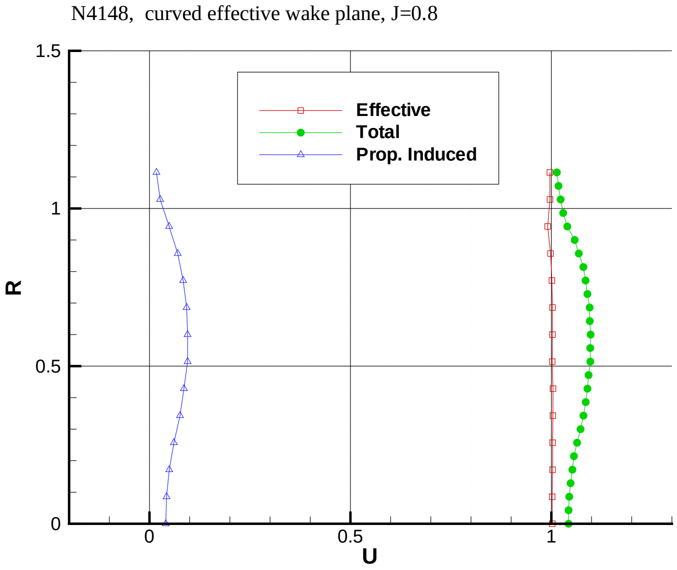

Figure 5.13: Total, induced and effective velocity when evaluated at a curved plane just a cell in the front of the blade LE.

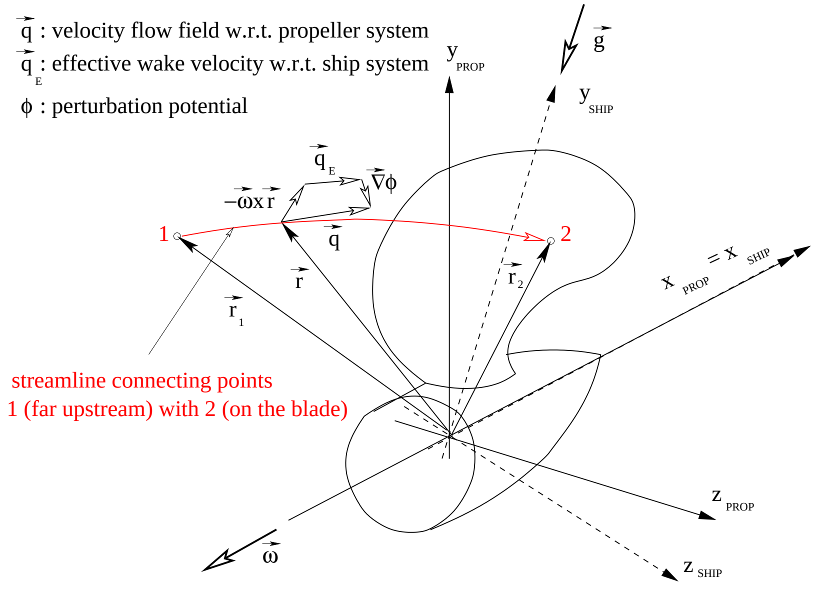

Figure 5.14: Velocity decomposition in front of the propeller in a ship-fixed system. Taken from Kinnas [2006]

where n is the normal vector to the blade surface.

The total flow velocity $\vec{q}$ in equation (5.4) is solved by the finite volume method base Euler solver, GBFLOW, and the propeller is represented by body forces. The unknown part of equation (5.4) is then $\vec{q_E}$, and it is normally a time averaged value to be only a function of space. The work of Kinnas [2006] is summarized next.

The Euler equation with respect to a rotating propeller system is:

$$\frac{D\vec{q}}{Dt} = -\nabla(\frac{p}{\rho}) + \vec{g} - \vec{\omega} \times (\vec{\omega} \times \vec{r}) - 2\vec{\omega} \times \vec{q} \tag{5.7}$$

After manipulation, as in Kinnas [2006], the final Euler Equation is in the form of

$$\frac{\partial \vec{q_E}}{\partial t} - \vec{q} \times (\vec{\nabla} \times \vec{q_E}) = -\vec{\nabla} H \tag{5.8}$$

where H is defined as follows:

$$H = \frac{\partial \phi}{\partial t} + \frac{p}{\rho} + \frac{q^2}{2} - \vec{g} \cdot \vec{r} - \frac{(\vec{\omega} \times \vec{r})^2}{2} \tag{5.9}$$

For ducted propeller subject to a uniform inflow U, the flow around the propeller is steady. We have

$$\frac{\partial \vec{q_E}}{\partial t} = 0 \tag{5.10}$$

$$\frac{\partial \phi}{\partial t} = 0 \tag{5.11}$$

Equation 5.8 is integrated along a streamline 1-2, as shown as in Figure 5.4.

$$\int_1^2 [\vec{q} \times (\vec{\nabla} \times \vec{q_E})] \cdot d\vec{r} = -\int_1^2 \vec{\nabla} H \cdot \vec{r} = H_1 - H_2 \tag{5.12}$$

The LHS of equation 5.12 is zero since it is along a streamline. So the value of H is constant along streamlines, as

$$\frac{p}{\rho} + \frac{{q_2}^2}{2} - \vec{g} \cdot \vec{r_2} - \frac{(\vec{\omega} \times \vec{r_2})^2}{2} = \frac{p_1}{\rho} + \frac{{q_1}^2}{2} - \frac{(\vec{\omega} \times \vec{r_1})^2}{2} \tag{5.13}$$

The pressure implemented in MPUF-3A has a format as following:

$$\frac{p}{\rho} + \frac{{q_2}^2}{2} - \vec{g} \cdot \vec{r_2} = \frac{p_1}{\rho} + \frac{{q_{e,2}}^2}{2} + \frac{p_{eff}}{\rho} \tag{5.14}$$

where, $\vec{q_{e,2}}$

$$\vec{q_{e,2}} = \vec{q_{E,2}} - \vec{\omega} \times \vec{r_2} \tag{5.15}$$

Equating the equation (5.13) and equation (5.14), the effective pressure used in Bernoulli equation is:

$$\frac{p_{eff}}{\rho} = \frac{{q_{e,1}}^2}{2} - \frac{(\vec{\omega} \times \vec{r_1})^2}{2} - \frac{{q_{e,2}}^2}{2} + \frac{(\vec{\omega} \times \vec{r_2})^2}{2} = \frac{{q_{E,1}}^2}{2} - \frac{{q_{E,2}}^2}{2} \tag{5.16}$$

When the inflow is uniform with velocity U, equation 5.16 can be rewritten as:

$$\frac{p_{eff}}{\rho} = \frac{U^2}{2} - \frac{{q_{E,2}}^2}{2} \tag{5.17}$$

Dividing by U^2 on both sides and taking into account of the nondimensional terms in GBFLOW, the nondimensional effective pressure can be written as:

$$\bar{p_e} = \frac{1 - \bar{q_e}^2}{2} \tag{5.18}$$

This effective pressure is added to the hydrostatic pressure term when calculating the pressure at the dynamic boundary condition points in the VLM. It decreases the ambient pressure in the vicinity of the propeller. Therefore, the cavitation predicted with the effective pressure model will be larger than that without the effective pressure model.

Cavitation tests of ducted propeller 1452 inside duct D15 were carried out at the Swedish State Shipbuilding Experimental Tank. The details of the experiment, including geometry of propeller and duct, will be discussed later in Section 6.2.2. This ducted propeller is used to study the influence of the effective pressure on the cavity shapes on blades.

In this numerical run, the cavitation number is $\sigma_n = 1.25$, and the advance ratio $J = 0.5$. Froude number is $F_n = 5$. The Froude number is defined as:

$$F_n = n^2 D/g \tag{5.19}$$

where g is the gravitational acceleration, n is the rotational speed of the propeller, and D is the diameter of the propeller. The cavitation number is defined as:

$$\sigma_n = \frac{p - p_v}{\frac{1}{2}\rho n^2 D^2} \tag{5.20}$$

where p_v is the vapor pressure. Iterations between MPUF-3A and GBFLOW, as discussed before, are carried out until the thrust and torque converge. The effective pressure term is added to the hydrostatic pressure term in MPUF-3A, as discussed before.

At the beginning of the iteration (we name it 0th iteration hereafter), a uniform velocity is used as guessed effective velocity. The nondimensional effective

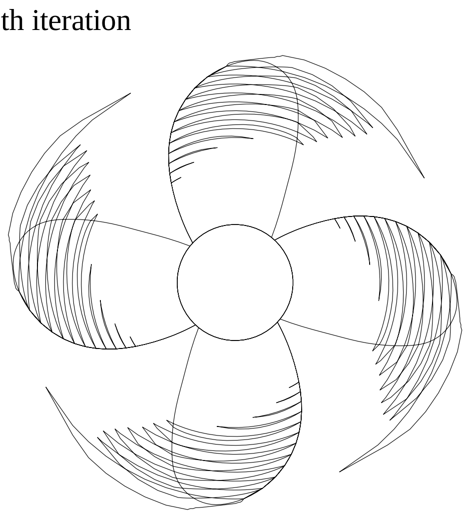

Figure 5.15: Cavitation at the 0th iteration, notice the effective pressure term is zero at this step.

velocity is then $\bar{q_e} = 1$ and the effective pressure term in equation (5.18) are zero. The cavity patterns at the 0th iteration are shown in Figure 5.15. As the iteration continues, the effective velocity predicted from GBFLOW is modified. The effective pressure is updated according to equation (5.18). The cavity shape predicted after the first iteration is shown in Figure 5.16. It is clear that the model with effective pressure terms predicts larger cavition volume than the model without such a modification. The iteration converges at the 10th iteration, and the final cavity pattern is shown in Figure 5.17. Comparing with the cavity pattern without the effective pressure, larger cavition volume can still be seen. This agrees with our expectation: the effective pressure term increases the cavity volume.

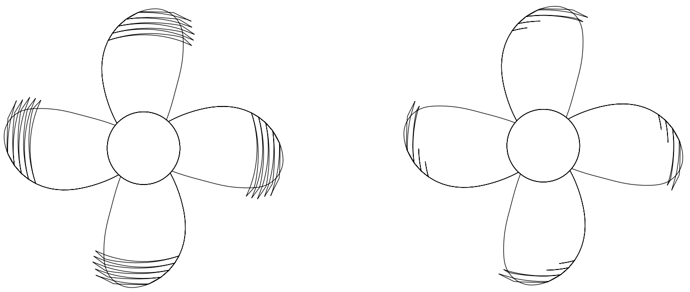

after 1st iteration

with effective pressure

without effective pressure

Figure 5.16: Cavitation at the 1st iteration with effective pressure model (left) and without effective pressure model (right).

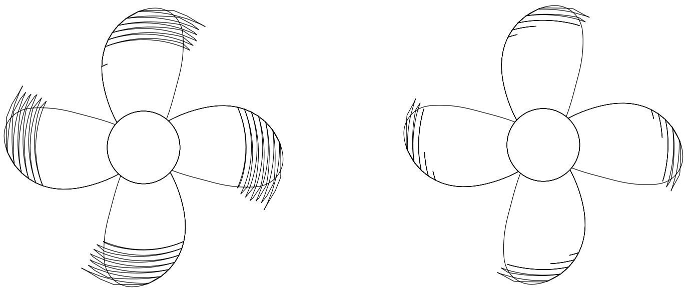

after 10 iterations

with effective pressure

without effective pressure

Figure 5.17: Cavitation at the 10th iteration with effective pressure model (left) and without effective pressure model (right).

Chapter 6

Verification with Other Methods

In the previous chapters, the current method applicable of modeling ducted propellers was introduced. In this chapter, the current method is verified through comparisons with available results from other numerical methods.

6.1 Verification of Bare Duct Cases

For bare duct cases, the propeller inside the duct is absent. Therefore, no iterations between GBFLOW and MPUF-3A are necessary. Results of bare duct cases are of value in the following aspects: (1) indications whether GBFLOW is reliable. (2) good check for grid quality. It is always recommended that a bare duct case be run before it is coupled with MPUF-3A. It will also be helpful in improving the grid quality and determining the artificial viscosity parameters.

6.1.1 Duct with NACA0015 Thickness Form

A duct section with zero camber and NACA0015 thickness distribution with an angle of attack for the section $\alpha = 0^o$ is subject to a uniform inflow, U. The duct section is similar to that in Figure 6.2, except that the angle of attack is different. There are 140 cells on the duct surface, and the total number of cells is $200 \times 75 =$

$15,000$.

A grid dependence study is performed at first. As we know, the analytical drag force should be zero since this is an ideal flow calculation. However, discretization error can not be totally eliminated. Therefore a numerical friction coefficient is defined based on the nondimensional surface of the duct $\bar{S}$, as follows:

$$C_{f,num} = \frac{2\bar{F}_x}{\bar{S}} \tag{6.1}$$

where the $\bar{F}_x$ is the nondimensional x component of the integrated pressure force. Notice the pressures are nondimensionalized as following in GBFLOW.

$$p = \frac{\tilde{p}}{\rho U^2} \tag{6.2}$$

where $\tilde{p}$, ρ and U are dimensional pressure, density and inflow velocity respectively.

The value of the numerical friction coefficient, $C_{f,num}$ is shown versus number of cells around the duct in Figure 6.1. The error is in the order of 10^{-3}, which is close to the value of the friction coefficient on a plate at high Reynolds numbers. The discretization error will decrease with an increase in the cell numbers.

A duct with a NACA0015 section and an angle of attack $\alpha = 10^o$ was analyzed in Kerwin et al. [1987]. The duct chord length is equal to the duct radius at the leading edge.

In the modeling of Kerwin et al. [1987], a potential based panel method was applied. Rectangular panels were distributed on the duct inner/outer surface. The chordwise panel numbers around the duct section ranged from 36 to 60, while the circumferential panel numbers ranged from 9 to 60.

x/c	-0.5	-0.4	-0.3	-0.2	-0.1	0.0
r_i/R	1.216	1.103	1.057	1.030	1.016	1.010
r_o/R	1.216	1.220	1.199	1.179	1.160	1.142
x/c	0.1	0.2	0.3	0.4	0.5	
r_i/R	1.010	1.016	1.026	1.037	1.050	
r_o/R	1.123	1.107	1.090	1.072	1.058	

Table 6.1: Coordinates of the inner and outer surfaces of the duct section of D15.

The grid of a center plane, together with contours of pressure, of the current method are shown in Figure 6.2. The predicted pressure distributions on the duct section from the current method (using both axisymmetric and 3-D versions) and the panel method by Kerwin et al. [1987] are compared in Figure 6.3. The pressure matches well on most parts of the section.

6.1.2 D15

D15 is one of the duct sections designed by Dyne [1973]. At the design stage, the duct was represented by placing ring-vortices and ring-sources upon a representative cylinder with constant diameter. The shape of the duct was then calculated from the law of continuity. The geometry coordinates are given in Table 6.1, where x is the axial coordinate, c is the chord length of the duct section. R is the radius of the propeller, r_i and r_o are the radial coordinates of the inner and outer surfaces respectively.

A C-type of grid is created for GBFLOW, as shown in Figure 6.4. The total grid size is 228×64, where 228 cells are placed along the ξ direction and 64 cells along the η direction (refer to Appendix A for details of the curvilinear coordinates

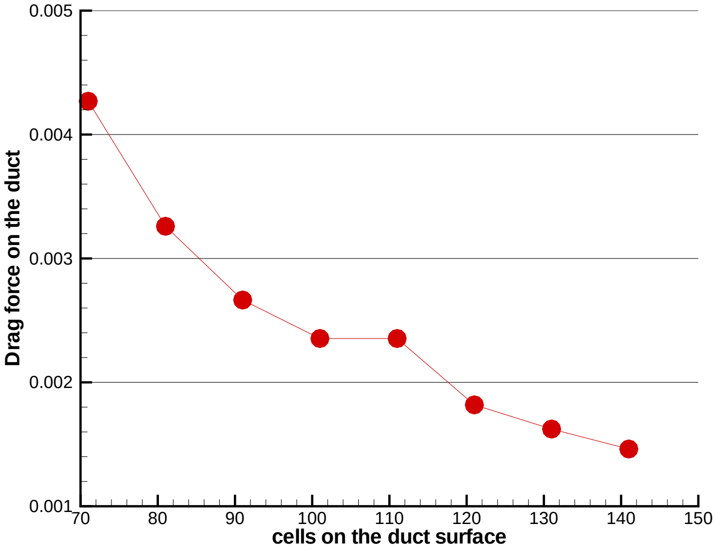

Figure 6.1: Integrated axial force, expressed as a frictional coefficient, $C_{f,num}$, vs. number of cells along the duct surface.

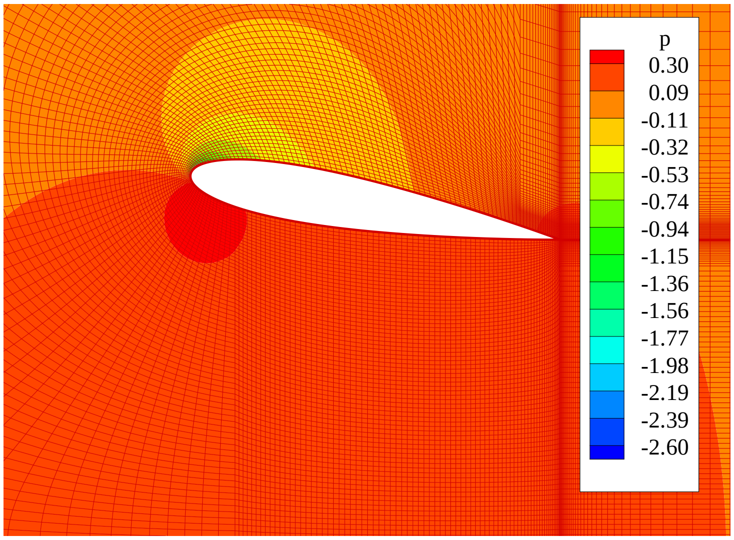

Figure 6.2: Grid around duct with NACA0015 thickness form, together with contours of pressure.

for C-type grid). There are totally 190 cells on the duct surface. The contours of axial velocity and the streamlines are shown in Figure 6.5.

To verify the numerical results from the current method, several different numerical tools are applied to the same bare duct.

The first tool is a commercial CFD code, FLUENT. The grid has a total size of $76,570$ cells, with a boundary layer consists of 10 layers of cells on the surface of the duct section. Finer grid is created in the vicinity of the duct and coarse triangle grid when far away from the duct. Such a grid is shown in Figure 6.6. A five equations Reynolds Stress model is applied for the viscous model. The pressure is discretized by a PRESTO! (PREssure STaggering Option) scheme, and pressure is coupled with velocity by a PISO (Pressure-Implicit with Splitting Operators) scheme. The momentum equation is discretized by a QUICK (Quadratic Upwind Interpolation for Convective Kinematics) scheme. The Reynolds number, based on the duct chord length, is $Re = 10^7$. The convergence criterion is that all errors reduce to below 10^{-5}.

The second tool is a potential based boundary element method developed at the University of Texas at Austin, named PROPCAV (PROpeller CAVitation analysis). The panels for duct D15 in PROPCAV are shown in Figure 6.7. There are 100 panels around the duct section and 81 cells along the circumferential direction for both sides. A straight wake is assumed after the duct trailing edge, and consists of 50 panels along the axial direction.

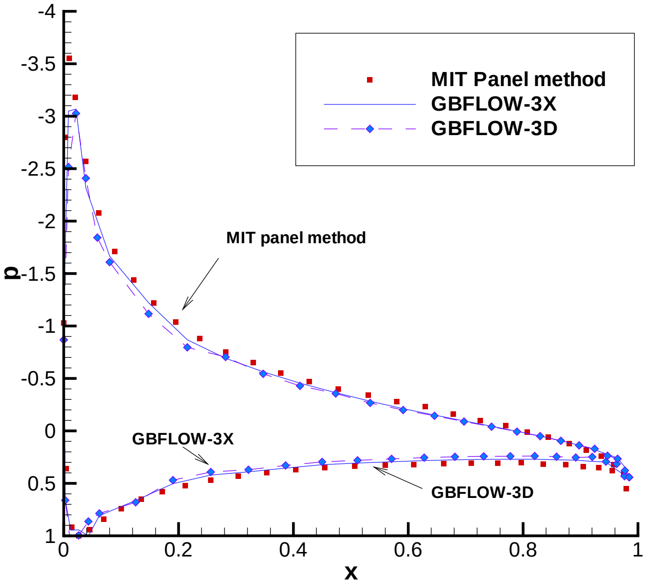

Figure 6.3: Pressure distributions predicted from the panel method of Kerwin et al. [1987] and the current method.

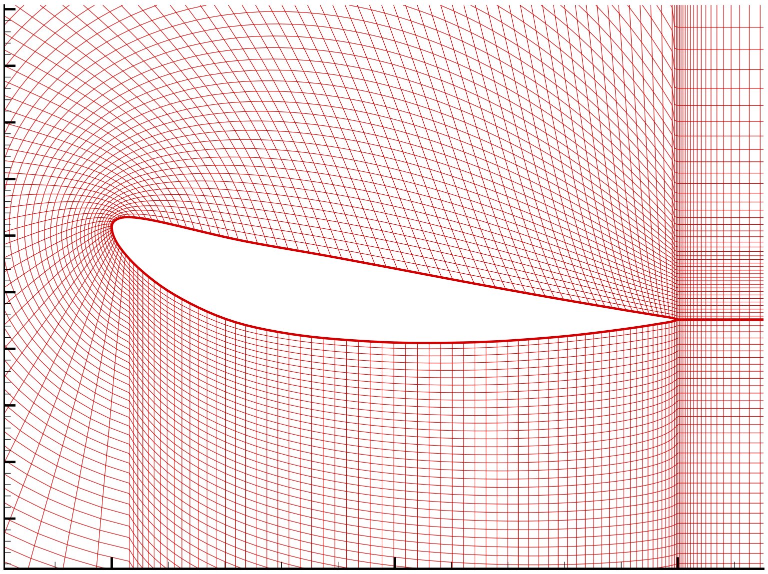

Figure 6.4: Grid of duct D15 in the vicinity of the duct for GBFLOW.

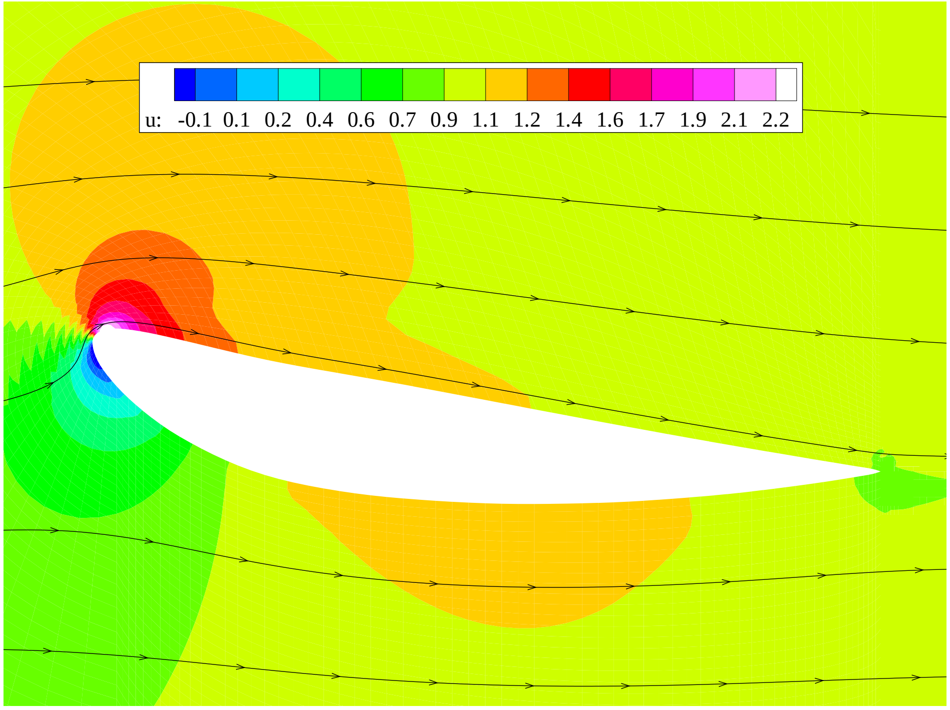

Figure 6.5: Contours of axial velocity and streamlines near the duct D15.

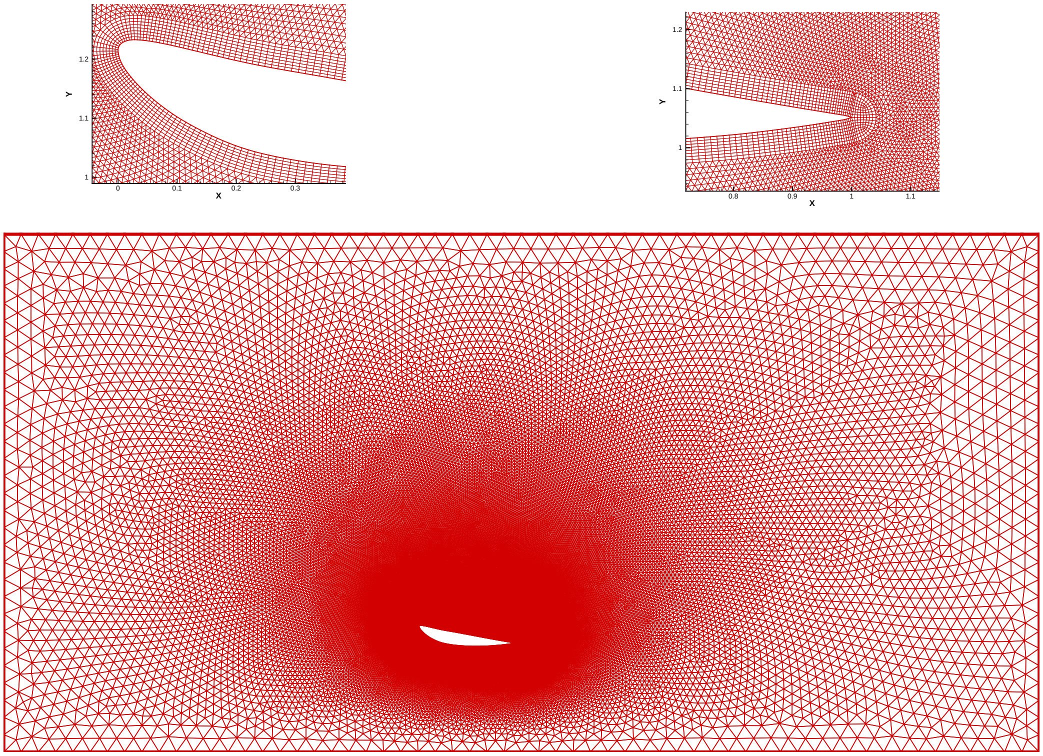

Figure 6.6: Grid in FLUENT, with boundary layers magnified at the leading edge and trailing edge of the duct section.

The pressure coefficient, defined as:

$$C_P = \frac{p - p_0}{\rho u_\infty^2} \tag{6.3}$$

is compared in Figure 6.8. Notice both viscous and inviscid results are included for the FLUENT runs. For all the methods, the pressure predictions are very close to each other.

6.2 Wetted Ducted Propeller

When a propeller is present, an iteration procedure between MPUF-3A and GBFLOW is necessary. Comparisons with other methods will give us guidance on the improvement of the current method.

6.2.1 Ducted propeller 3745

Ducted propeller DTMB 3745 was modeled in Kerwin et al. [1987]. The duct has a NACA 0.8 meanline distribution with $f_{max}/c = 0.04$ and a NACA 66 MOD thickness distribution with $t_{max}/c = 0.15$. The ducted propeller has a tip clearance of 4% of the propeller radius. The propeller has five blades with a non-zero chord at the tip. The grid and body force distribution at the center plane are shown in Figure 6.9. The axisymmetric solver GBFLOW3X is applied, and the body force are both time averaged and circumferentially averaged. The effective velocity is sought at a curved effective velocity plane in front of the propeller leading edge.

In the work of Kerwin et al. [1987], the problem of duct and hub were solved

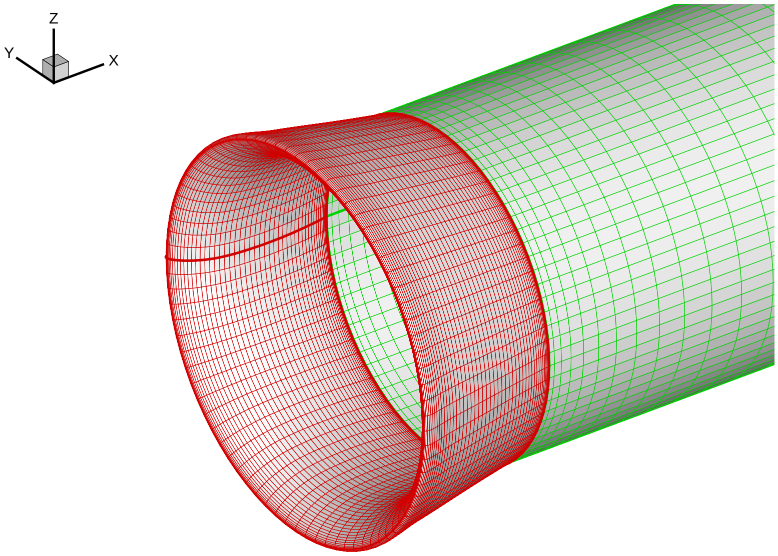

Figure 6.7: Panels on the duct and wake in PROPCAV.

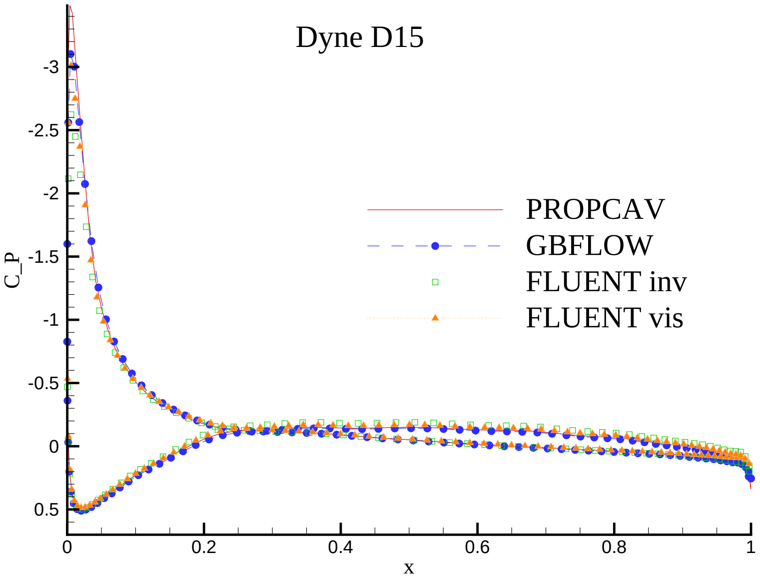

Figure 6.8: Pressure coefficients on the duct, compared among PROPCAV, GBFLOW, FLUENT viscous model and inviscid model.

by boundary element method, while the propeller problem was solved by the vortex lattice method. An iterative procedure between BEM and VLM was applied to solve the problem: The duct and hub were first solved under uniform inflow and the induced velocities at the blade control points were evaluated. Combining the induced velocity and inflow velocity, the propeller problem was then solved by requiring that the total normal velocity vanished at each control point. The induced velocity at the centroid of the each panels on the duct and hub was then calculated and used to modify the dipole strengths on the hub and duct, which in turn modified the induced velocities at blade control points. In this iterative way, the interaction between blade, hub and duct was included.

For fair comparison with the results in Kerwin et al. [1987], the gap model is not applied for this set of tests. The non-axisymmetric effect of the duct on the propeller is accounted for by the image model. The results from the current method for different number of panels in the spanwise direction are shown in Figure 6.10, where the circulation distribution predicted by Kerwin et al. [1987] is also shown. The circulation distribution predicted by the current method converges quickly with number of panels, and compares very well to that predicted by Kerwin et al. [1987].

For the case of zero tip, the circulation distribution for the current method are compared with the panel method for two different advance ratios in Figure 6.11. The circulation distributions for both Js match well between the two methods, except at the tip region. The discrepancy at the tip occurs because that the influence of duct on the propeller is represented by the induced velocity due to real panels on the duct in Kerwin et al. [1987], while an image model is applied to account for the

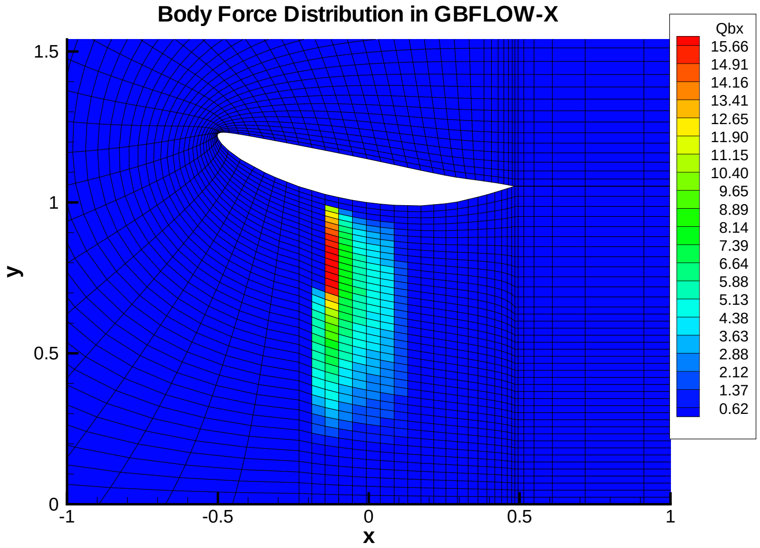

Figure 6.9: Grid and body force distribution in GBFLOW.

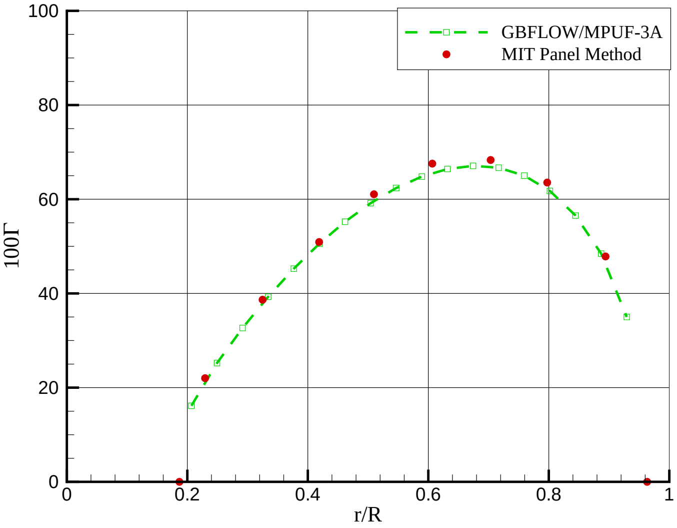

Figure 6.10: Circulation distribution for a 4% gap ducted DTMB 3745.

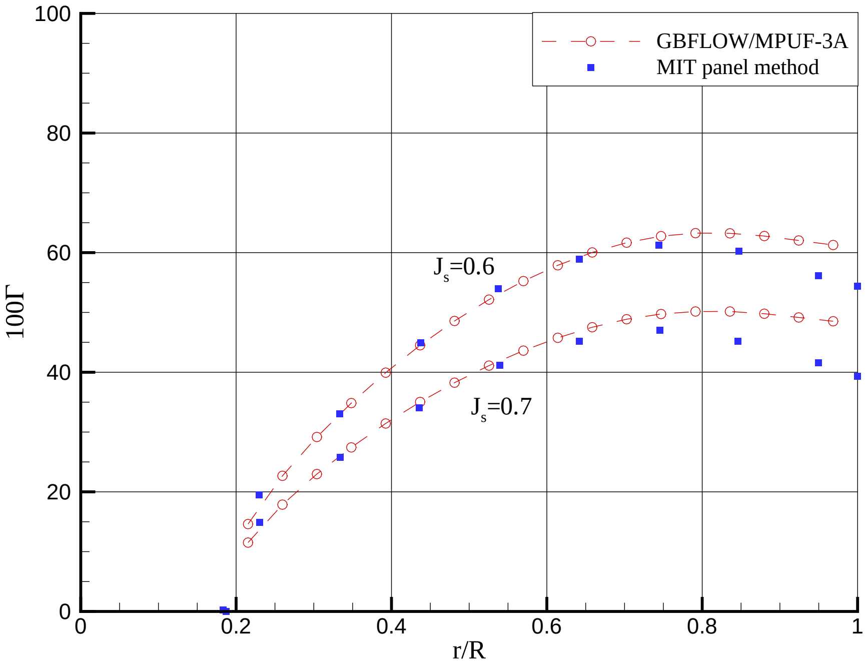

Figure 6.11: Circulation distribution for a 0% gap ducted DTMB 3745 for $J = 0.6$ and $J = 0.7$.

influence in the current method.

6.2.2 P1452 inside D15

Dyne [1973] designed the geometry of P1452 as the propeller to fit inside duct D15. The propeller is a four-bladed, right handed propeller. The mean line of the blade section is in the form of NACA $a = 0.8$ camber. The thickness form is NACA 16. The diameter of the propeller is $D = 189.6\ mm$ and the pitch ratio at $r = 0.7R$ is $P/D = 0.988$. The ducted propeller has the following geometric characteristics: the angle of attack of the duct section is $\alpha = 9.2^o$, and the maximum camber to chord ratio of the duct is 0.060. The radial clearance between the propeller tip and the duct inner surface is $1.0\ mm$. The calculated gap percentage is then 1.09%.

Grid dependence studies are carried out at advance ratio of 0.6. Along the ξ coordinator of the grid, the cell numbers are varied from 229 to 299, and along the η coordinator, the cells numbers are fixed to 65. The circulation distributions along the blade span are shown in Figure 6.12 and the pressure distributions are shown in Figure 6.13. The circulation distributions are more sensitive to the number of grids, but finally converge for the finest grid. The pressure distribution converges as well.

At an advance ratio $J_s = 0.6$, the ducted propeller is modeled by both the current method and CFD code FLUENT.

For the current method, a C type of grid with totally 228×64 cells in both grid curvilinear directions is created. There are about 150 cells located on the duct surface. The effective velocity is evaluated at the nearest curved plane in front of the blade LE. The propeller chord length at the tip is equal to *zero*, which leads to a varying gap ratio inside the gap. Thus the gap model is not applied when the propeller problem is solved in MPUF-3A.

For FLUENT calculation, a grid with more than 50,000 cells is created. Ten layers of boundary layer cells are created on the duct surface, and a region of quadrilateral cells are used in the propeller plane to fill in sources. These source terms are interpolated on the cells, and converted into dimensional unit, as

$$\hat{\vec{Q}} = \rho \frac{u^2}{\hat{R}} \vec{f} \tag{6.4}$$

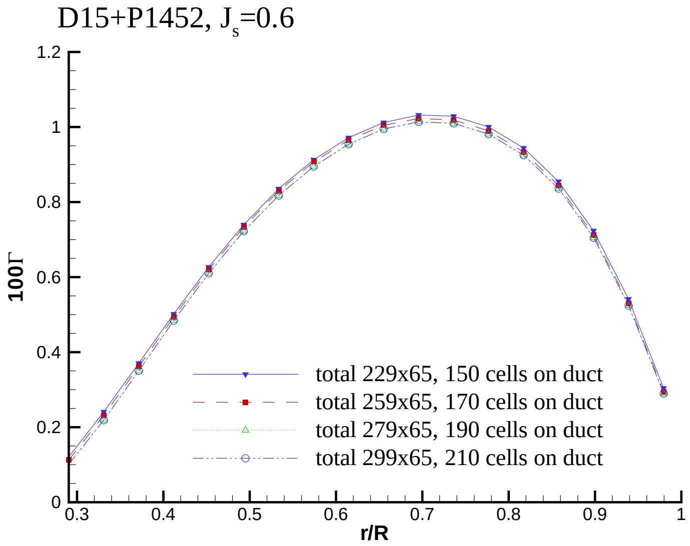

Figure 6.12: Convergence of circulation distributions on the blade of P1452 propeller, with different grids.

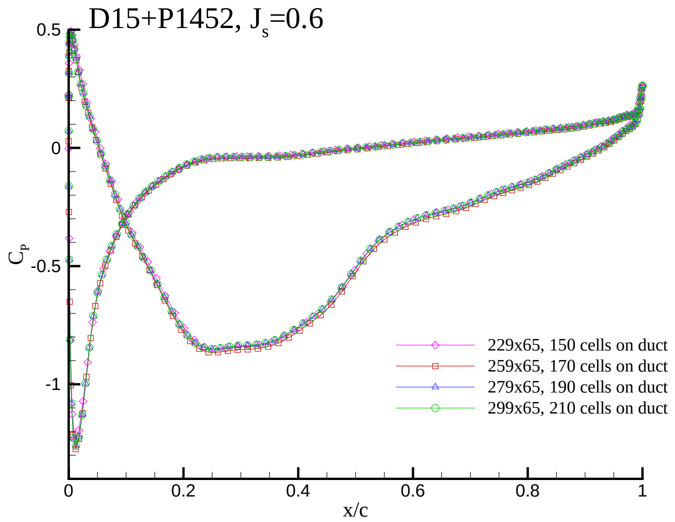

Figure 6.13: Convergence of pressure distributions on the duct D15, with different grids

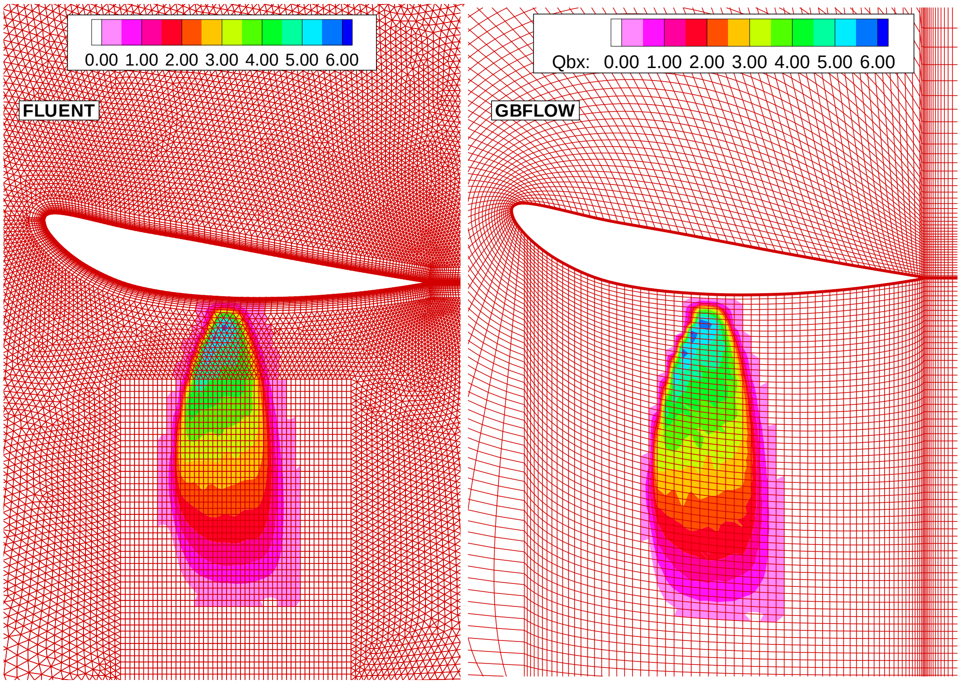

Figure 6.14: The body force distributions of P1452 propeller inside duct D15 in viscous FLUENT (left) and GBFLOW (right).

where ρ, u and $\hat{R}$ are dimensional density of fluid, inflow velocity and dimensional propeller radius respectively. $\hat{\vec{Q}}$ is the dimensional source term in FLUENT, with the unit $\frac{kg}{m^2s^2}$. The nondimensional interpolated source term in axial direction in FLUENT, together with the grid, is shown in Figure 6.14. Compared to the body force distribution inside GBFLOW solution, the source terms are interpolated in a correct way. A Spalart-Allmarras model is used as the viscous model in FLUENT. The inflow at the inflow boundary is $u = 10\ m/s$. The Reynolds number, based on the chord length of the duct section is $Re = 10^7$.

The converged swirl velocity in FLUENT is compared with that of GBFLOW in Figure 6.15, where some difference due to viscosity occurs in the middle span region. The pressure coefficients from GBFLOW is shown in Figure 6.16, together with the inviscid model from FLUENT and the viscous model from FLUENT. It is observed that the viscous effects in this case increases the pressure on the inner surface of the duct. The pressure prediction from the current method compares well with that of the inviscid FLUENT model, however, both of them overpredict the thrust on the duct, which is defined as:

$$KT_D = \frac{T_D}{\rho n^2 D^4} \tag{6.5}$$

where T_D is the dimensional thrust on the duct, and it is calculated through the integration of the pressure force in the axial direction, as

$$T_D = \int_A p\vec{n} \cdot \vec{x_u} dA \tag{6.6}$$

where p is the pressure, and $\vec{n}$ is the normal vector for dA and $\vec{x_u}$ is a unit vector in the axial direction, $i.\ e.$, $(1, 0, 0)$. A positive thrust is defined in the upstream direction, which is opposite to the flow direction. The difference in the thrust on the duct is shown in Table 6.2.

Ducted propeller P1452 inside D15 is also modeled by PROPCAV. The pressure on the duct and panels on propellers are shown in Figure 6.17. The pressure distribution on the duct and the circulation distribution are compared for $J_s = 0.6$ in Figures 6.18 and 6.19. The same comparison for a lower advance ratio at $J_s = 0.5$ are shown in Figures 6.20 and 6.21. The discrepancy on the pressure occurs mainly

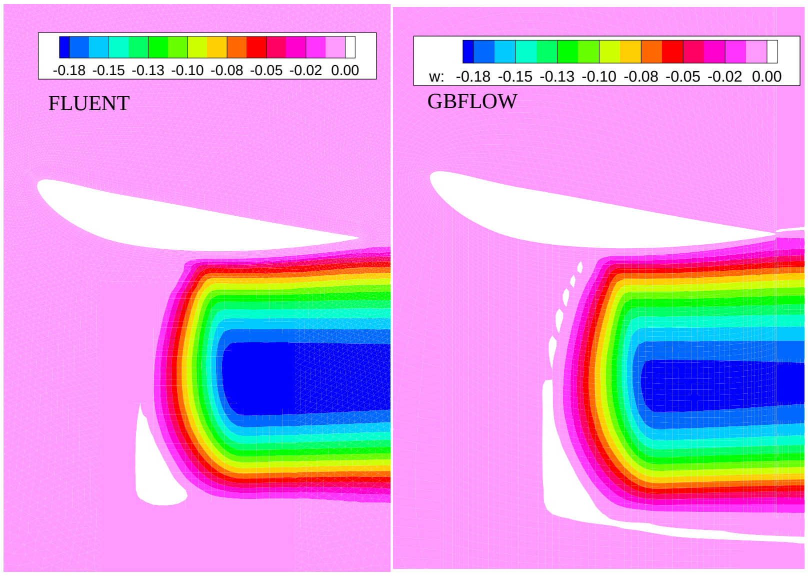

Figure 6.15: Contours of tangential velocity of P1452 propeller inside duct D15 in FLUENT (left) and GBFLOW (right).

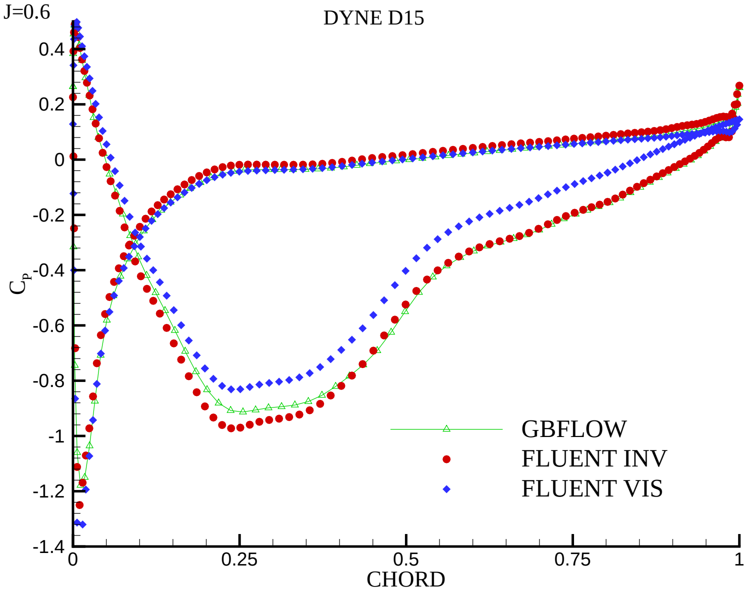

Figure 6.16: Pressure distribution on the duct D15, compared among GBFLOW, FLUENT viscous, FLUENT inviscid models.

Method	KT_D
GBFLOW	0.036
FLUENT (inviscid)	0.036
FLUENT (viscous)	0.028

Table 6.2: Thrust on the duct for ducted propeller 1452 inside duct D15, from GBFLOW, FLUENT inviscid and viscous methods.

on the inner surface of the duct and the leading edge. The major difference in the circulation occurs at the mid-span and tip region. The possible reason for the difference is the thickness effects of the blades.

6.3 Cavitating Ducted Propeller

The effective pressure term is included to satisfy the Bernoulli equation when the cavitating ducted propeller is modeled. This effective pressure modifies the ambient pressure close to the propeller, and thus modifies the cavity prediction in MPUF-3A.

6.3.1 DTMB 3745 inside Duct with NACA0015 Section

The coupling of MPUF-3A and GBFLOW is applied on cavitating DTMB 3745 ducted propeller, which was introduced in section 6.2.1. Even though the inflow is uniform, the hydrostatic effect is included by solving in an unsteady manner, without considering the time variation. An advance ratio of $J_s = 0.7$, a Froude number of $F_n = 2.0$ and a cavitation number $\sigma_n = 5.0$ are used. The gap size between duct inner surface and the blade tip is zero.

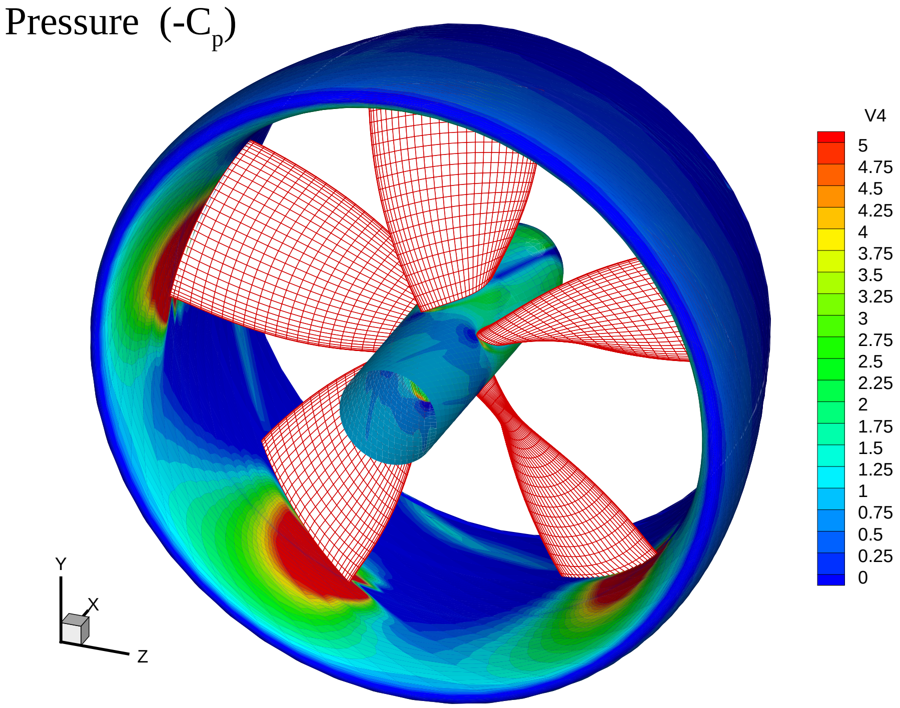

Figure 6.17: Pressure distribution on the duct, and panels on the blades in PROPCAV (Lee and Kinnas [2006])

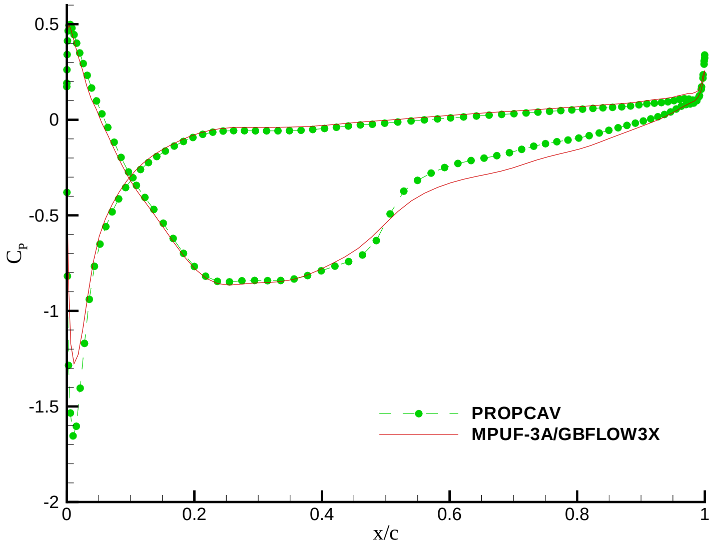

Figure 6.18: Pressure distribution on duct D15, for GBFLOW/MPUF-3A and PROPCAV (Lee and Kinnas [2006]), at $J_s = 0.6$.

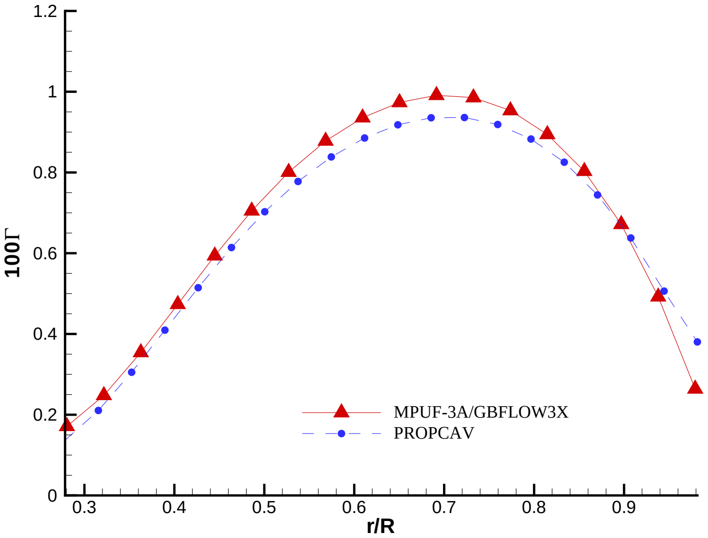

Figure 6.19: Circulation distribution on P1452 propeller, for GBFLOW/MPUF-3A and PROPCAV (Lee and Kinnas [2006]), at $J_s = 0.6$.

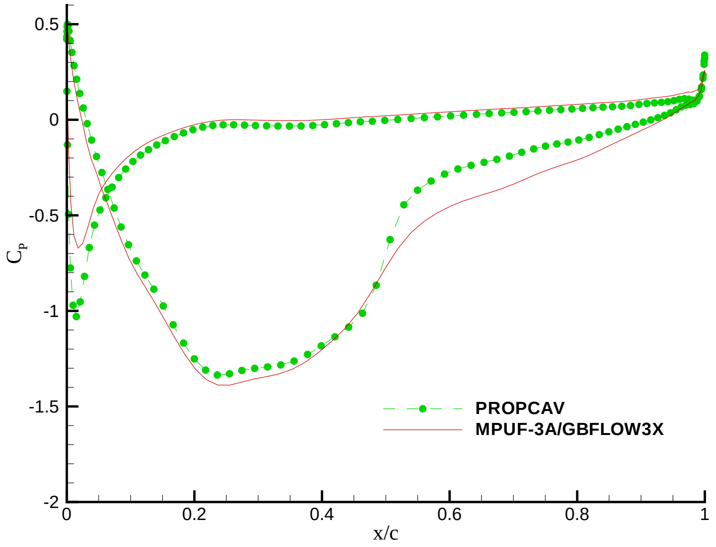

Figure 6.20: Pressure distribution on duct D15, for GBFLOW/MPUF-3A and PROPCAV (Lee and Kinnas [2006]), at $J_s = 0.5$.

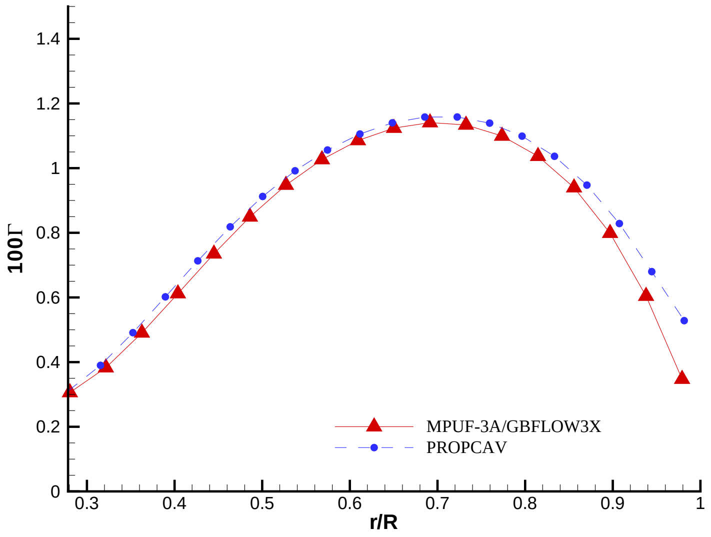

Figure 6.21: Circulation distribution on P1452 propeller, for GBFLOW/MPUF-3A and PROPCAV (Lee and Kinnas [2006]), at $J_s = 0.5$.

The body force distribution in GBFLOW is shown in Figure 6.22. The contours of tangential velocities are shown in Figure 6.23. The circulation distribution along the spanwise direction is compared with PROPCAV in Figure 6.24. The circulation from PROPCAV is larger than that of GBFLOW/MPUF-3A at the blade tip, and this difference causes discrepancy in the cavity shape as shown in Figure 6.25. The lower loading at the tip of blade from coupling of GBFLOW and MPUF-3A is associated with less cavitation at the tip and also reduces the cavity length on other spanwise strips.

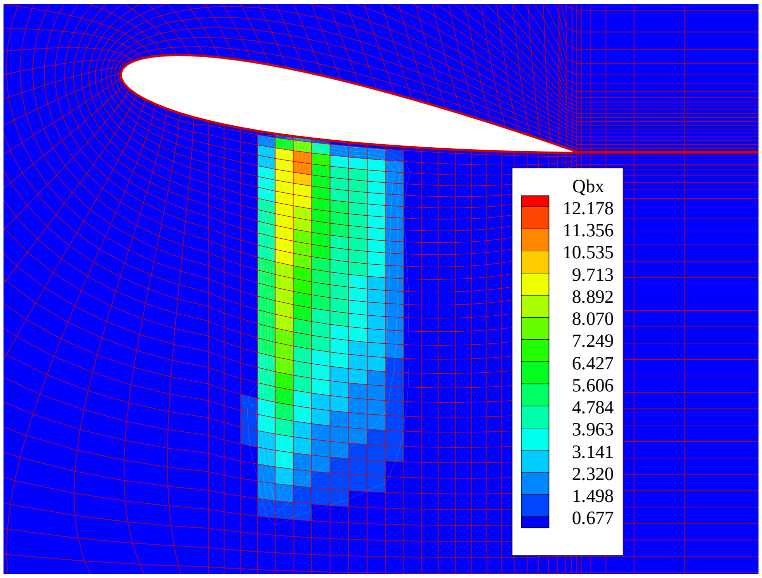

Figure 6.22: Body force distribution in GBFLOW, for DTMB 3745 inside a duct with NACA0015 section, at $J = 0.7$, $F_n = 2.0$, and $\sigma_n = 5.0$.

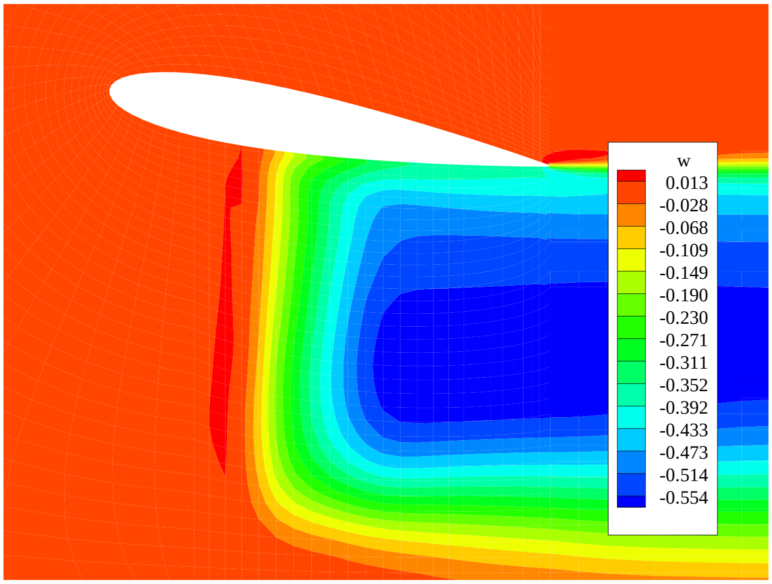

Figure 6.23: Contours of tangential velocities in GBFLOW, for DTMB 3745 inside a duct with NACA0015 section, for $J = 0.7$, $F_n = 2.0$, and $\sigma_n = 5.0$.

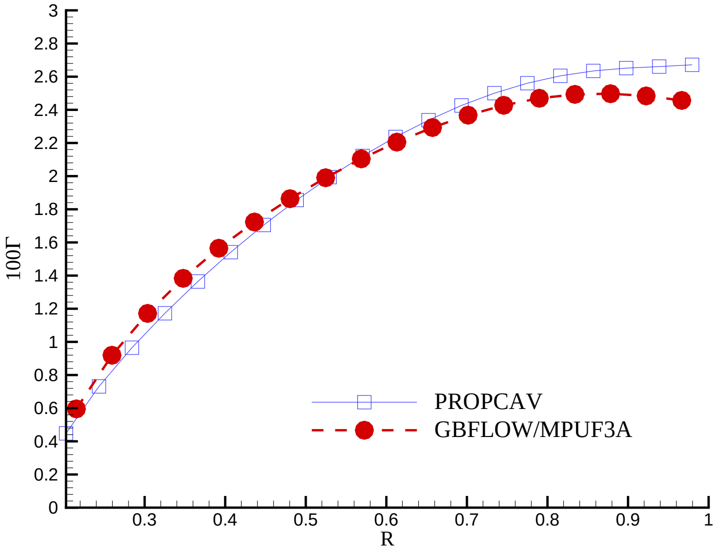

Figure 6.24: Comparison of circulation distributions predicted by the present method and PROPCAV (Lee and Kinnas [2006]), at $J = 0.7$, $F_n = 2.0$, and $\sigma_n = 5.0$.

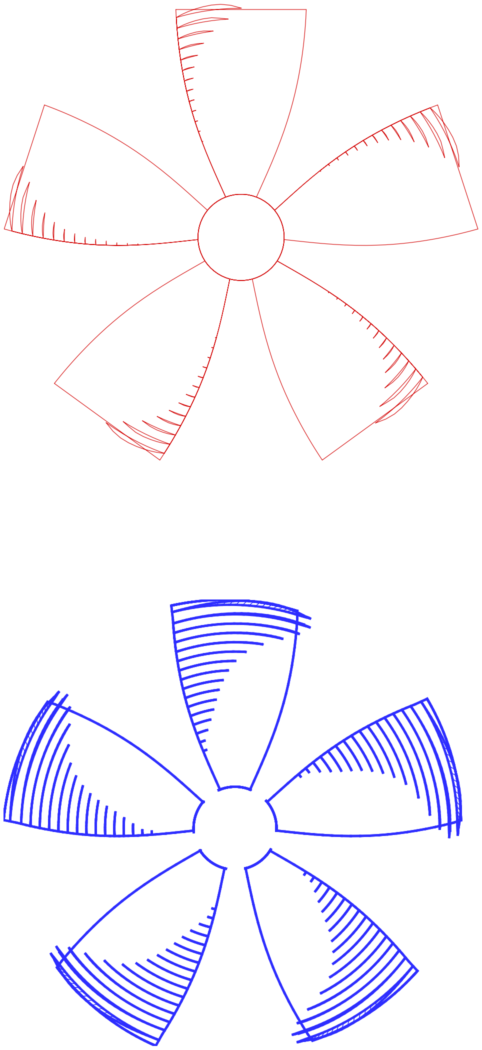

Figure 6.25: Cavity patterns predicted by the current method (top) and PROPCAV (bottom, Lee and Kinnas [2006]), at $J = 0.7$, $F_n = 2.0$ and $\sigma_n = 5.0$.

Chapter 7

Validations with Data from Existing Experiments

In this chapter, the current method is validated with limited number of experiments.

7.1 Duct II

Experiment data for duct II were provided in Morgan and Caster [1965]. This duct has a cross section of modified NACA 66 thickness distribution with thickness to chord ratio of $t_{max}/c = 0.10$ and a NACA $a = 0.8$ meanline with camber ratio $f_{max}/c = 0.04$. The angle of attack for duct section is zero and the ratio between the chord length and the duct radius at the leading edge is equal to 0.8. The pressures on the duct were measured for two different inflow angles: $\alpha_r = 0$ and $\alpha_r = 4$.

It is appropriate to use the 3-D version of GBFLOW to consider the inclination of inflow. Due to the axisymmetry of Duct II, a 2-D C type of grid surrounding the Duct II section is rotated along the x axis to create circumferential cells. The inflow with an inclination of 0^o or 4^o is set as the boundary condition at the inflow and the far field boundary.

Under uniform inflow at $\alpha_r = 0$, the predicted pressure contours together

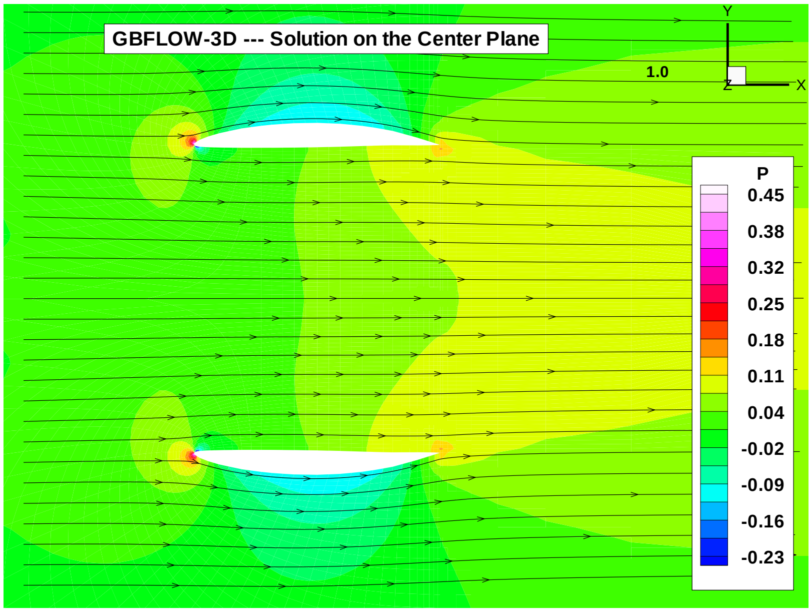

Figure 7.1: Pressure contours and streamlines around DUCT II at $\alpha_r = 0^o$.

with streamlines by GBFLOW are shown in Figure 7.1. The pressures on both sides of the duct agree well with those measured by Morgan and Caster [1965], as shown in Figure 7.2. When the uniform inflow is inclined at $\alpha_r = 4^o$, the pressure contour and streamlines by GBFLOW are shown in Figure 7.3. The predicted pressures are also close to the measurement, as shown in Figure 7.4.

7.2 Ka 4-70 inside Nozzle 19A

Systematic experiments on ducted propellers were conducted in the Netherlands Ship Model Basin (NSMB) by Oosterveld [1970]. Ducted propeller Ka 4-70 and nozzle 19A (the term 'nozzle' is used instead of 'duct' in accordance to that report) is chosen to validate the current method. The Ka 4-70 propeller has four

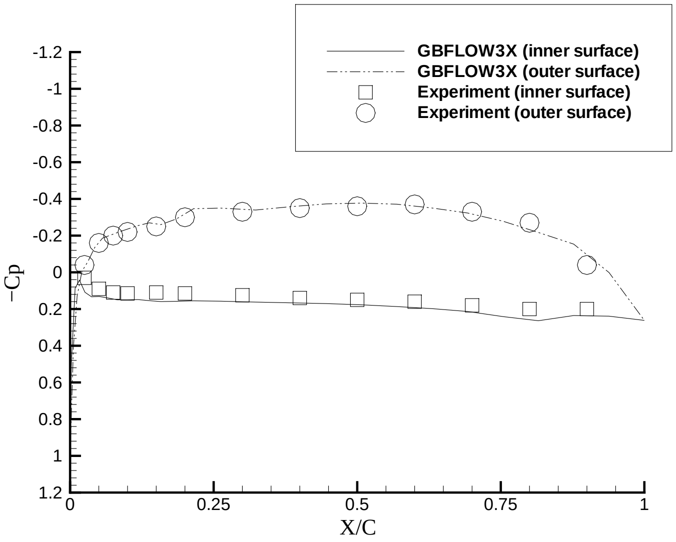

Figure 7.2: Predicted vs. measured pressures on Duct II; $\alpha_r = 0^o$.

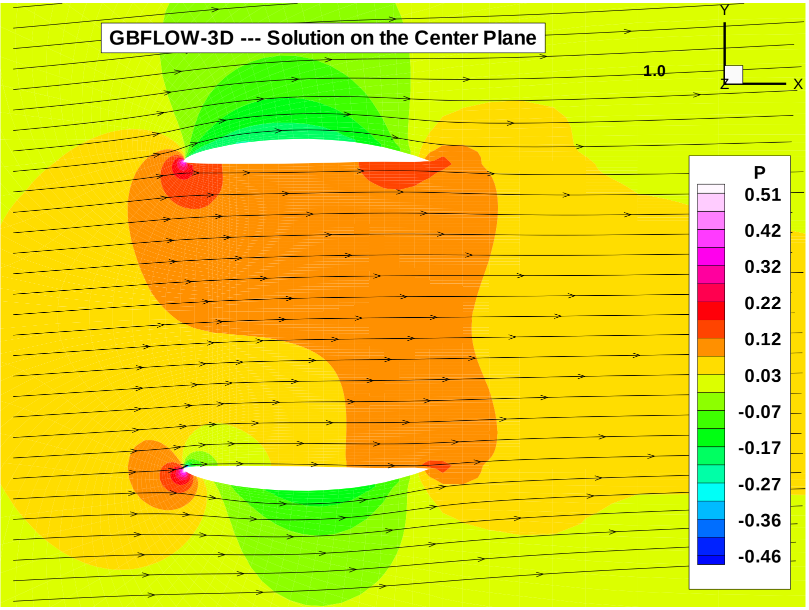

Figure 7.3: Pressure contours and streamlines around DUCT II at $\alpha_r = 4^o$.

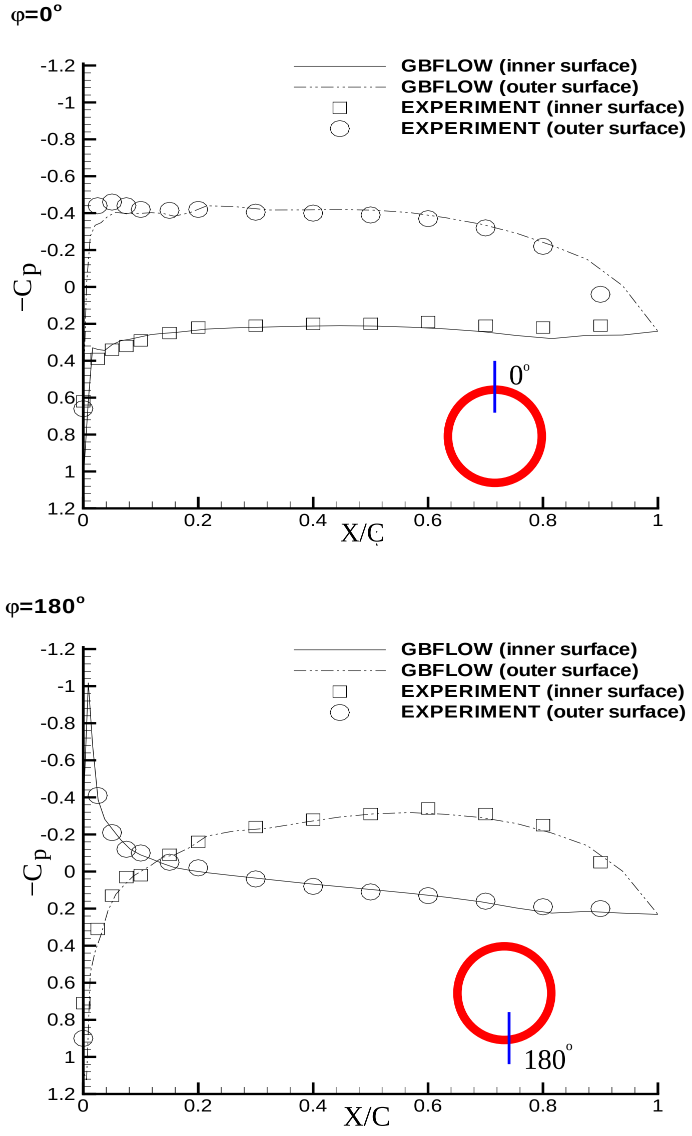

Figure 7.4: Duct II at $\alpha_r = 4^o$. Predicted (by GBFLOW-3D) vs. measured pressures, at $\phi = 0^o$ (top) at $\phi = 180^o$ (bottom).

blades of Kaplan type, and the chord at the blade tip is finite. The nozzle 19A has an axial cylindrical part as the inner side of the duct at the propeller location to adopt the propeller tip. The outside of the duct is made straight to simplify its manufacturing, and the trailing edge of the duct is round. The pitch ratio of the propeller at $r = 0.7R$ ranges from 0.8 to 1.4, and the design advance ratio is $J_s = 0.7$. The gap between the duct inner surface and the propeller tip is uniform and equal to 1 mm, which corresponds to 0.38% of the propeller radius.

The thrust of the nozzle is normalized as $KT_D = \frac{T_D}{\rho n^2 D^4}$, which is the same way as the propeller thrust is normalized. The frictional force on the duct is considered as follows:

$$K_{TD,fr} = C_f J_s^2 \bar{S}/8 \tag{7.1}$$

where C_f is a frictional coefficient taken as a function of the Reynolds number of the duct, J_s is the advance ratio, and $\bar{S}$ is the normalized surface area of the duct with respect to the square of the propeller radius. The value of C_f is determined using the ITTC formula, as

$$c_f = \frac{0.075}{(logRe - 2)^2} \tag{7.2}$$

where Re is the Reynolds number. The total thrust of the ducted propeller system is the combination of the blade thrust, the nozzle thrust and the frictional correction part, as follows:

$$K_{TT} = K_{TP} + K_{TD} - K_{Td,fr} \tag{7.3}$$

where K_{TP} is the propeller thrust.

The axisymmetric version of GBFLOW is applied to predict the flow in the whole fluid domain. For a Ka 4-70 propeller with a pitch ratio of $P/D = 1.0$, the method with gap model and the method without gap model are both applied to solve the propeller problem. The method without gap model has only image to account for the nonaxisymmetric duct wall effects. The method with gap model has gap panels implemented and orifice equation (4.11) with discharge coefficient $C_Q = 0.84$ satisfied inside the gap region. For the gap model, the contours of body forces, together with the grid, are shown in Figure 7.5. The swirl and streamlines in the predicted flow domain for the same case are shown in Figure 7.6. In Figure 7.7, the predicted forces with and without the gap model are shown for a range of advance ratios. It is observed that the gap model increases the total thrust, especially at high advance ratios, and also improves (in relation to the measurement) the predicted thrust on the nozzle. For Ka 4-70 propeller with a pitch ratio of $P/D = 1.2$ at all radii, the comparison is shown in Figure 7.8. The current method with gap model overpredicts the torque coefficients K_Q, while thrust coefficients K_{TT} and K_{TD} match well with experiment data . For Ka 4-70 propeller with a pitch ratio of $P/D = 1.3$ at $r = 0.7R$, both methods predict well with the measurement, as shown in Figure 7.9. For pitch ratio of $P/D = 0.7$ at $r = 0.7$, the ducted propeller have negative thrust after $J_S = 0.6$, so only numerical results at four advance ratios are carried on. The results are still acceptable, since the scale is quite small.

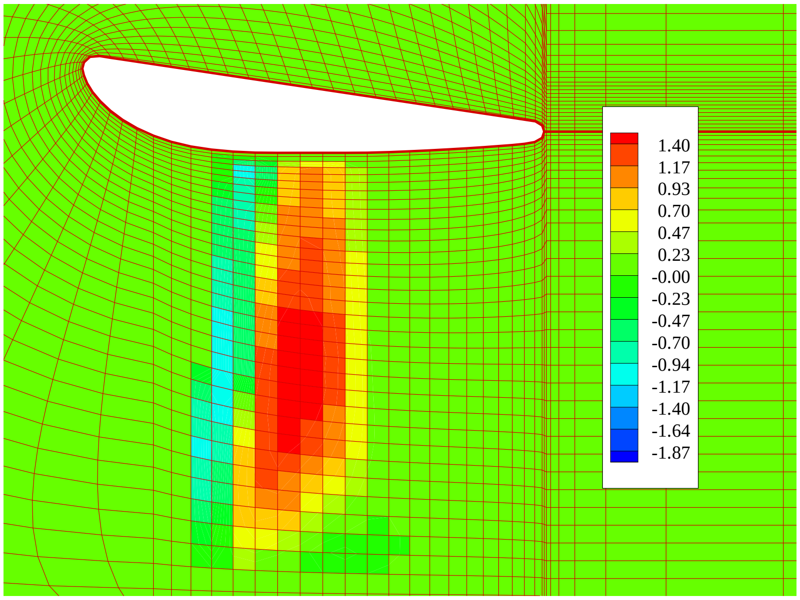

Figure 7.5: Body forces of Ka 4-70 inside nozzle 19A, $J_s = 0.8$

7.3 Propeller P1452 inside Duct D15

Ducted propeller P1452 inside duct D15 was introduced in section 6.2.2. In this section, the current method is compared to the experiment conducted by Dyne [1973].

The experiments were carried out in cavitating tunnel No 2. at Swedish State Shipbuilding Experimental Tank. In this test, the maximum water speed was $V_{max} = 23\,m/s$, and the minimum cavitation number σ_v was in the range of $0.06 - 0.15$. Maximum propeller shaft speed was $n_{max} = 6000\,rev/min$.

The cavitation number σ_v is defined as

$$\sigma_v = \frac{p - p_v}{1/2\,\rho {V_s}^2} \tag{7.4}$$

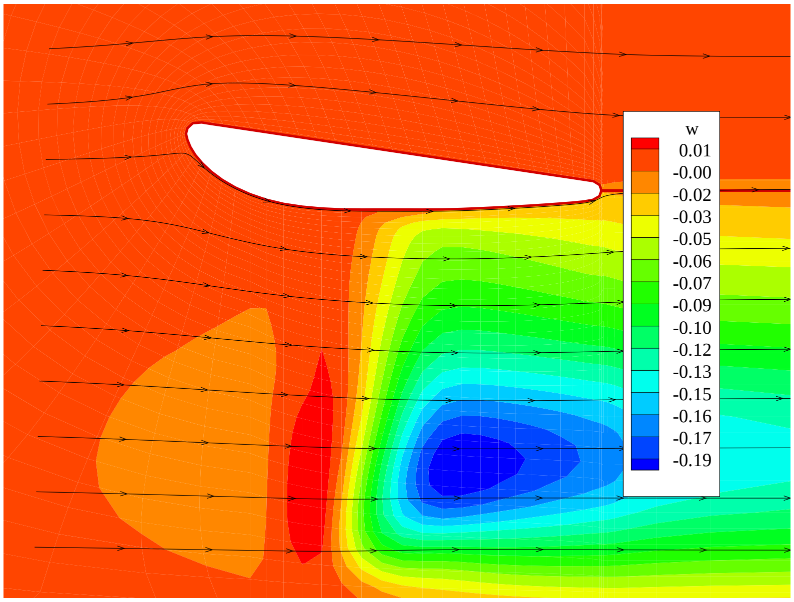

Figure 7.6: Swirl velocity contours and streamlines in the flow domain.

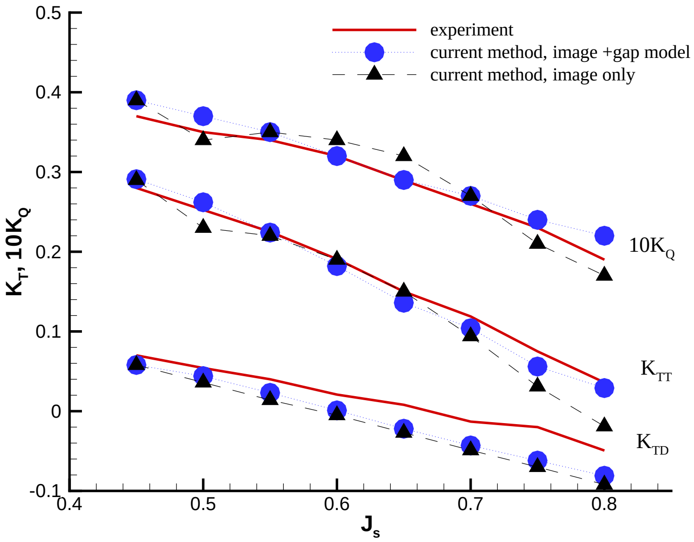

Figure 7.7: Comparison of thrust and torque coefficients measured in experiments and predicted by present method with gap model for Ka 4-70 propeller/Nozzle 19, when $P/D = 1.0$ at $r = 0.7R$.

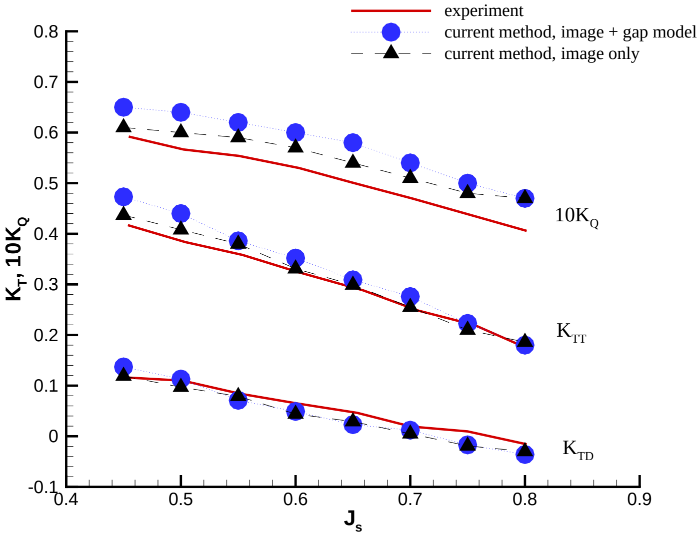

Figure 7.8: Comparison of thrust and torque coefficients measured in experiments and predicted by present method with gap model for Ka 4-70 propeller/Nozzle 19, when $P/D = 1.2$ at all radii.

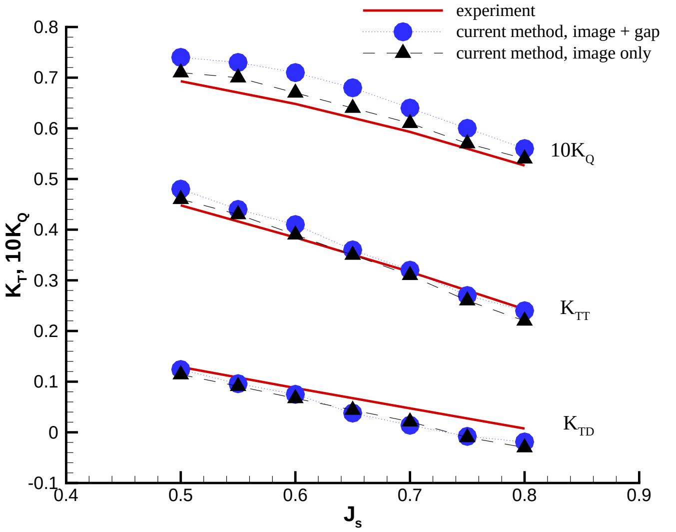

Figure 7.9: Comparison of thrust and torque coefficients measured in experiments and predicted by present method with gap model for Ka 4-70 propeller/Nozzle 19, when $P/D = 1.3$ at $r = 0.7R$.

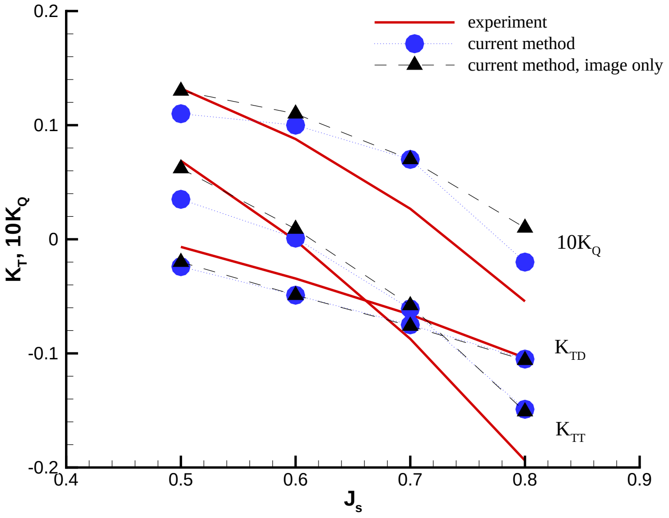

Figure 7.10: Comparison of thrust and torque coefficients measured in experiments and predicted by present method with gap model for Ka 4-70 propeller/Nozzle 19, when $P/D = 0.7$ at $r = 0.7R$.

The cavitation number used in MPUF-3A is based on the propeller rotational speed, as

$$\sigma_n = \frac{p - p_v}{1/2\ \rho n^2 D^2} \tag{7.5}$$

The following conversion from σ_v to σ_n is needed for MPUF-3A:

$$\sigma_n = \sigma_v \frac{{V_s}^2}{nD^2} = \sigma_v\ J_s^2 \tag{7.6}$$

Two methods are applied to calculate the thrusts and torques. The first method is is the effective wake evaluated at the curved plane ahead of the blade LE. The second method is that the effective velocity vectors are evaluated directly at blade control points.

The thrust and the torque of the propeller was determined with strain gauge balances inside the propeller housing. At low advance ratios, thrust break-down due to cavitation was observed. However, such a thrust break down is not that obvious in the numerical prediction of the current two methods. For $\sigma_v = 20$, the total thrust K_{TT}, the thrust on duct K_{TD} and the torque K_Q are compared with the results from experiments in Figure 7.11. It is observed that the torque is underpredicted on the whole range for the effective vector approach. The underestimation of blade torque implies the underestimation of propeller force. The sum of total thrust become acceptable only due to the cancellation of the underestimation of propeller force and the overprediction of the duct. For both methods, the total thrust and duct thrust are very close to each other along the whole range. As mentioned before, the computational effort for the effective vector method is much higher than the method of the curved effective velocity plane. It takes 1 hour and 49 minutes to finish a run

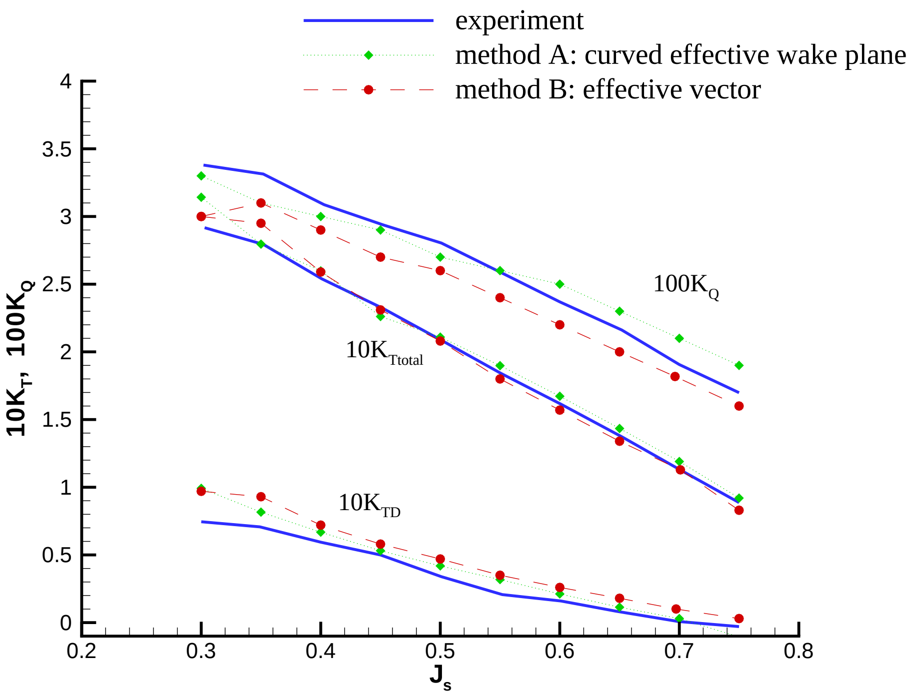

Figure 7.11: Comparison of thrust and torque coefficients measured in experiments and predicted by present two methods for 1452 inside D15, when $\sigma_v = 20$.

for an advance ratio by using the latter, while takes 10 hours and 15 minuted for the former.

Chapter 8

Tip Leakage Vortex Model

This chapter can be viewed as an accompanying chapter for the gap model. Even though the numerical results from the gap model is acceptable, we want to develop a more natural representation for the gap instead of the discharge coefficient imposed artificially in the gap model.

In this chapter, additional tip leakage vortex panels are implemented in the vortex lattice method (VLM). With a free wake relaxation algorithm, the geometry of the tip leakage vortices are aligned. The tip leakage vortices effectively increase the loading at the tip. In comparison to the gap model, the tip leakage vortex model is more natural, and is independent of any empirical assumptions. However, due to the lack of viscous tools to validate this tip leakage vortex model, it is still not clear whether the tip leakage vortex model should be used independently, or together with the gap model.

8.1 Review

For most ducted propellers, finite gaps between the duct and the tip of the propeller are required to avoid rubbing. The relative motion between the duct and the propeller, combined with the pressure difference across the gap, creates the gap

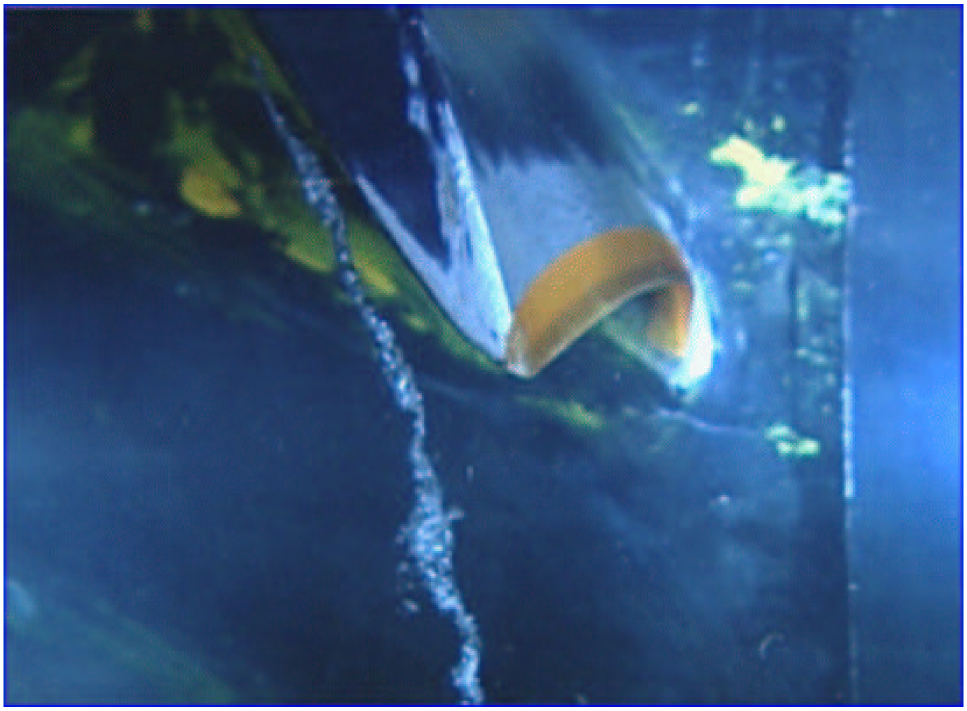

Figure 8.1: Tip leakage vortex on P5206. From Chesnakas and Jessup [2003]

flow. This flow is highly viscous due to boundary layer effects. Compared with those of open propellers, the loading of the propeller blades is higher due to the existence of the gap. The flow inside the gap could be very complex, since the gap flow is interacting with the flow over the surface of the blades. The resulting tip leakage vortex decreases the pressure and causes the inception of cavitations. These cavitations are carried through the leakage flow and will affect the performance of neighboring blades. Figure 8.1 shows the tip leakage vortex developed at the tip of P5206 propeller.

Experimental investigations on tip leakage vortices were carried out for an axial-flow pump at the Pennsylvania State University. Gearhart [1964] tried to cor-

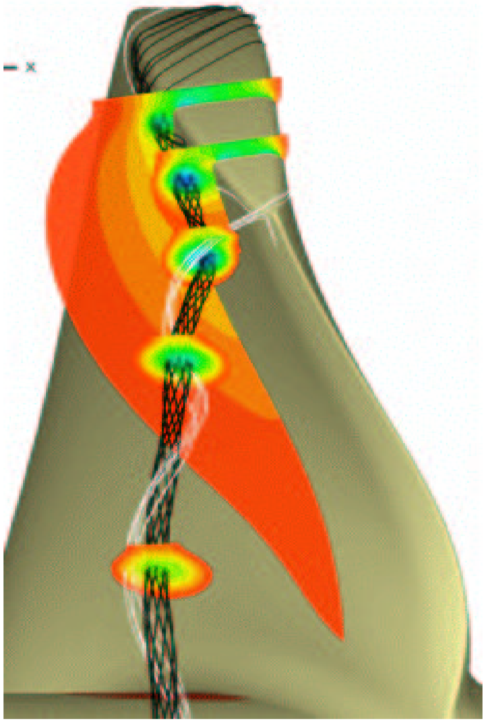

Figure 8.2: Tip leakage vortex on an Unstructured and Unsteady Navier Stokes solver U^2NCLE. From Brewer [2002]

relate the cavitation with ratio of blade tip thickness and tip clearance height, ratio of momentum thickness of the boundary layer to the tip clearance height, ratio of hydrodynamic tip loading to the tip speed and the gap configuration or shape. Farrel [1989] continued to identify the shed lift coefficient and the vortex core radius.

Numerical modeling of the gap flow and leakage vortex was done in Brewer [2002] by applying a 3-D unstructured and unsteady solver U^2NCLE for ducted propellers, as shown in Figure 8.2. Minimum pressure, circulation and axial/tangential velocities in the vortex core are also investigated.

Modeling of the tip leakage vortex can be considered as an extension of the modeling of the tip vortex with additional wall effects, with regard to both images and viscosity, included. Some related studies on numerical modeling of the tip vortex are given below.

Greeley [1982] developed a tip vortex model based on the lifting surface theory. In his work, the problem was decomposed into a global and a local analysis. The global analysis solved for the spanwise vortex strengths of the whole blade vortex lattices, requiring free slip at the kinematic boundary condition points. The local analysis included the roll up of a free vortex lattice, which was cut from the tip part of the original blade vortex lattice. A correlation between normal velocities and leading edge suction force (developed from a viscous analysis) was built and used as boundary conditions at the leading edge control points to determine the strength of free vortices. The free vortices would roll up, and their spatial location was determined by requiring the local vorticity vectors be parallel to the local velocity vector everywhere on the vortex sheet so that the free vortices are force free.

Lee [2002] modeled the tip vortex by a potential based panel method. In his work, a cylindrical tube was placed at the end of the propeller tip as the initial condition. Boundary condition $\frac{\partial \phi}{\partial n} = -\vec{u} \cdot \vec{n}$ was applied on the cylindrical tube control points in order to satisfy the force free condition for the tip vortices. The vortex core radii were then modified to satisfy the above boundary conditions and new tip vortex spatial location and geometry were updated. A schematic of his method is shown in Fig. 8.3.

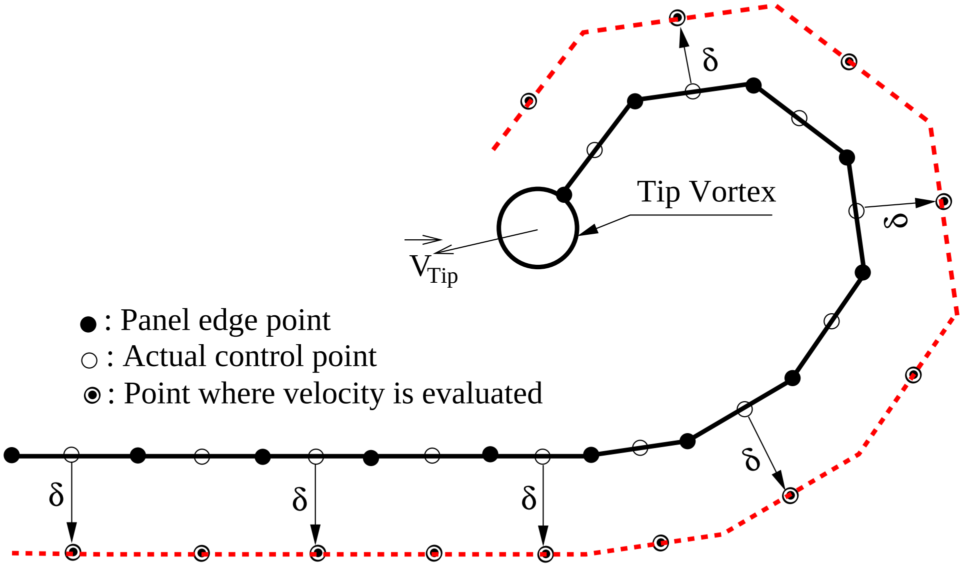

Figure 8.3: Schematic of modeling tip vortex core. From Lee [2002]

8.2 Numerical modeling

In the work of Lee [1979], a vortex sheet separation from the tip was included for a propeller operating in a heavily loaded condition. In principle, the exact position of the separated vortex sheet, can be found by an iterative alignment with local streamlines. However, this iterative procedure is not guaranteed to find the exact location. Therefore Lee [1979] applied an idealized separated tip vortex model, where the geometry of tip vortex was fixed and no alignment was applied. The separated tip vortices originated from the LE of the blade tip panels, and finally concentrated after a collecting point and convected downstreams.

The work of Lee [1979] and Greeley [1982] built the foundation for the tip leakage vortex modeling. The tip leakage vortices can be modeled with initial tip vortex setting, as Lee [1979], and wake alignment algorithm, as Greeley [1982], with consideration of wall effects.

In the vortex lattice method, the following groups of singularities are included: (1) blade bounded and free vortices (2) transition wake shed and trailing vortices (3) ultimate wake vortices (4) blade and cavity sources. Besides these, the tip leakage vortex model consists of two additional groups of singularities: (5) tip leakage vortices (the separated vortices at the tip) (6) concentrated tip leakage vortices (rolling up vortices after the collecting point). Such a tip leakage vortex model is shown in Figure 8.4.

The initial geometry of the tip leakage vortex is determined by parameters d_n and d_r, which define the displacement of the collecting points in normal and radial direction from the blade surface, as shown in Figure 8.5. The geometry of the initial tip leakage vortices is shown in Figure 8.6 for propeller DTMB 3745, at advance ratio $J_s = 0.1$. Different from the blade horseshoe structure in Figure 4.12, a blade with a tip leakage vortex model has additional tip horseshoes, as shown in Figure 8.7.

The initial geometry of the tip leakage vortex in Figure 8.6 modifies the distribution of load at the blade. For propeller DTMB 3745 at $J_s = 0.1$, the loading is highly increased, as shown in Figure 8.8. In the same figure, results of a convergence test on panel numbers for tip leakage vortex case is also shown. In addition, the effect of the initial guess of d_n on the blade loading is shown in Figure 8.9. When the tip vortex geometry is not aligned, a larger d_n corresponds to a higher loading at the tip. The differences in the loading with different initial geometries are expected to decrease when an alignment of the tip leakage vortices is implemented.

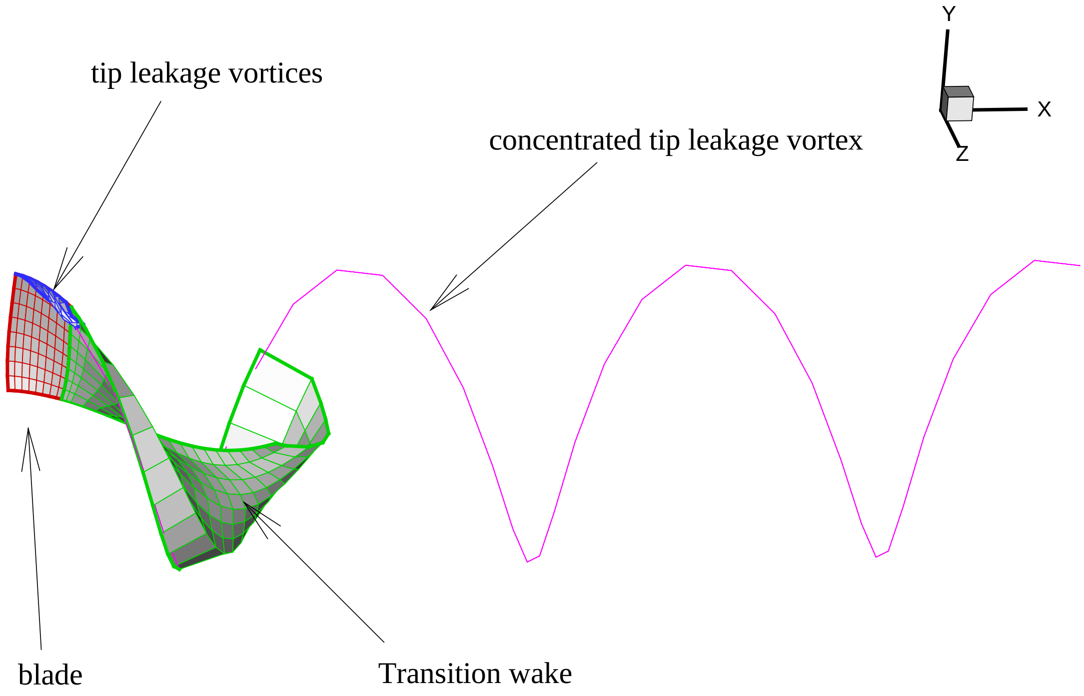

Figure 8.4: Discretization of vortices with the tip leakage vortex model in MPUF-3A.

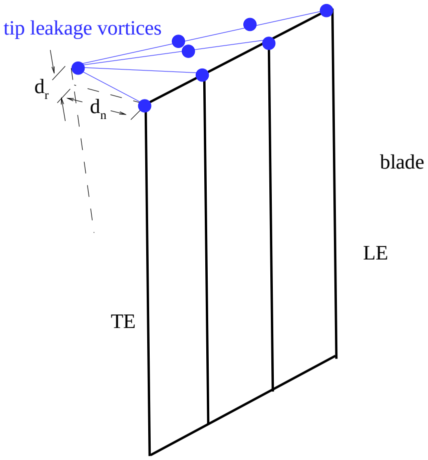

Figure 8.5: Parameters defining the initial geometry of the tip leakage vortices.

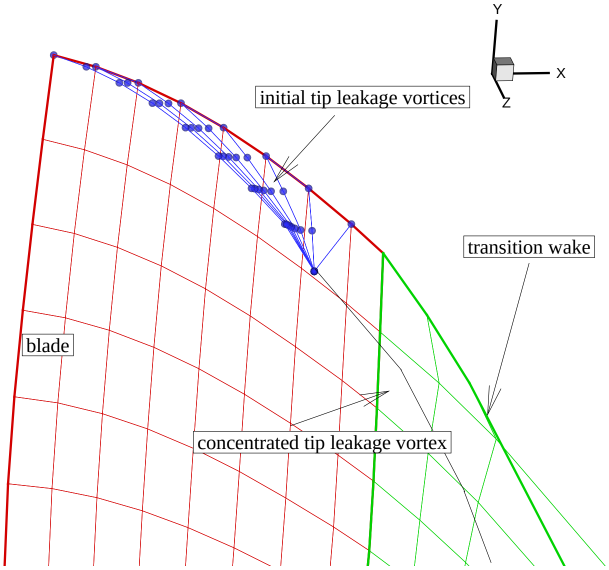

Figure 8.6: The initial geometry of the tip leakage vortices of DTMB 3745 propeller.

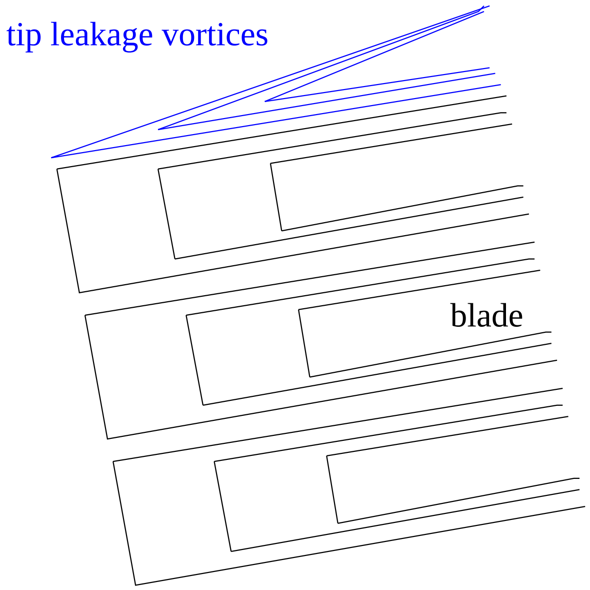

Figure 8.7: Typical blade horseshoe loops on the blade when tip leakage vortex model is implemented.

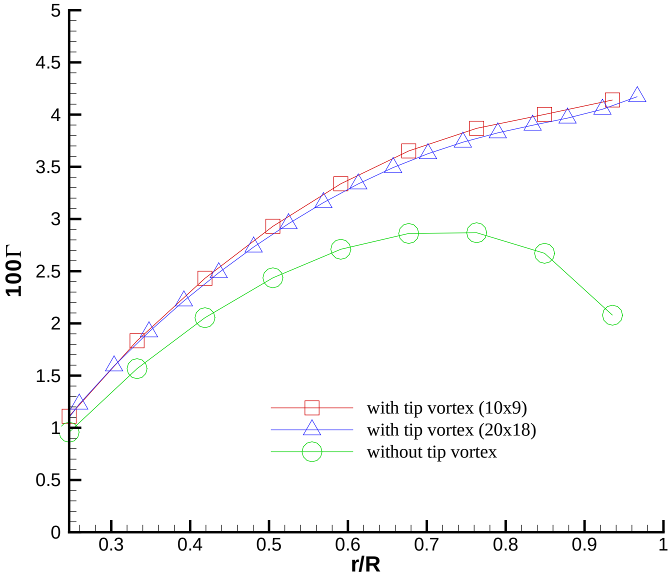

Figure 8.8: Circulation distribution when tip leakage vortex is NOT aligned. The initial d_n is 0.1.

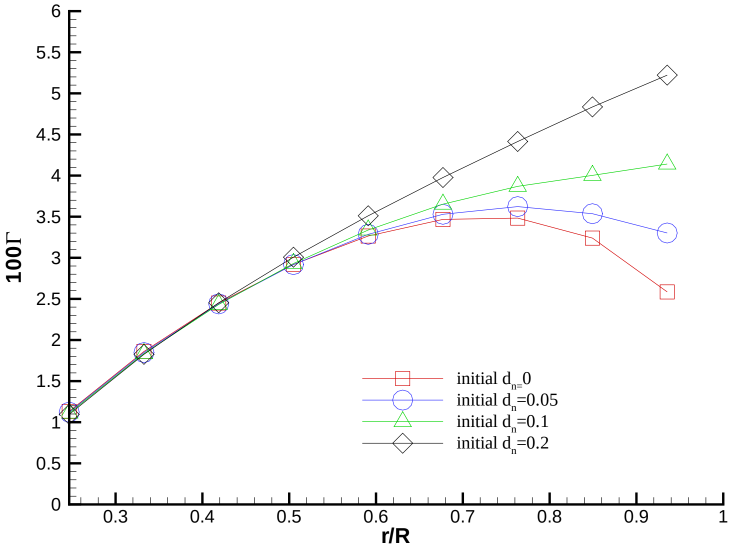

Figure 8.9: Effects of initial d_n on the circulation distribution. The tip leakage vortex is NOT aligned.

The alignment of tip leakage vortex is very similar to that of the trailing wake. It is worthwhile presenting the alignment procedure for the trailing wake first, and then continuing with the alignment of the tip leakage vortices.

The geometry of the trailing wake greatly affects the evaluation of the induced velocities on the blade, and hence affects the loading on the blade. On the other hand, the blade loading can also influence the geometry of the trailing wake. A correct pitch distribution of the transition wake is needed to keep the wake being force-free.

It is possible, yet more time consuming, to get the dual effects solved at the same time. In MPUF-3A, a correct transition wake geometry is solved at the first stage, then the loading and cavity extents are evaluated with the fixed wake geometry at the second stage.

The goal of the first stage is to find the correct wake pitch. According to the measurements at the MIT water tunnel, the wake pitch varies smoothly in the downstream direction. Therefore, an effort-saving and reasonable approach is to determine the correct wake pitch at a limited number of points and assume a smooth variation of pitch in the rest of points. In MPUF-3A, the selected points are at a location just after the tailing edge (called “near field”) and a location close to 70% of the trailing wake length (called “far field”). An iterative procedure is required to get the correct pitch, as following:

(a) A steady problem of equation (3.7) with an assumed trailing wake is solved on a 8x8 vortex lattice. A constant wake pitch is used to generate the assumed wake. The strengths of line vortices on the blade are determined.

(b) Using the strengths of the line vortices on the blade, the induced velocities at near and far field are calculated. A third order polynomial is applied to interpolate the velocities between near and far field. The blade pitch corresponding to the interpolated velocities is calculated and the wake geometry is aligned to maintain the force free characteristic.

(c) The steady problem using the updated wake geometry is resolved and vorticity distribution is determined. The iteration between step (a) and (b) continues until the induced velocities at near field and far field converge.

At the second stage, the blade is discretized as NN (chordwise) $\times MM$ (spanwise) panels. The wake geometry from the previous stage is interpolated to have finer panels. The steady/unsteady wetted/cavitating problem is carried out to solve the strengths of line vortex loops and cavity sources.

The implementation of tip leakage vortices will have influence on both stages above. At both stages, the following modifications are carried out:

(a) Add the effects of the horseshoes (Figure 8.7) with initial geometry settings (Figure 8.6) into the influence coefficients.

(b) Solve equation (4.12) to find out the unknown strengths. The strengths of tip leakage vortices (TLV) and their concentration (CTLV) become known.

(c) Evaluate the induced velocities $\vec{q}_{ind}$ at the vertices of TLV and CTLV, including the self induced velocities from connecting line vortices at these vertices.

(d) Sum the induced velocity $\vec{q}_{ind}$ with local inflow velocity $\vec{q}_i$ to get the total velocity $\vec{q}_t$.

(e) Update the locations of the TLV and CTLV using a Free Wake Relaxation method. For the first stage, an Euler scheme is good enough since only steady problem is solved:

$$\vec{x}_{i+1} = \vec{x}_i + \vec{q}_t(\vec{x}_i)\delta t \tag{8.1}$$

where $\vec{x}_i$ is the location of TLV/CTLV at the ith node, and $\vec{x}_{i+1}$ is the one following the ith node. δt is the time step size, and is determined from the angular increment of the discretized wake sheet $\delta\theta$.

$$\delta t = \frac{\delta\theta}{\omega} = \frac{\delta\theta}{2\pi n} \tag{8.2}$$

where ω is the propeller rotational speed, with unit of radian per second. For the second stage, a predictor-corrector scheme might be necessary since unsteady problem is solved:

$$\begin{aligned} predictor \quad \vec{x}^0_{i+1} &= \vec{x}_i + \vec{q}_t(\vec{x}_i)\delta t && (8.3) \\ corrector \quad \vec{x}_{i+1} &= \vec{x}_i + \frac{\vec{q}_t(\vec{x}_i) + \vec{q}_t(\vec{x}^0_{i+1})}{2}\delta t && (8.4) \end{aligned}$$

(f) Update the influence coefficients with aligned geometries, and carry out the solution again.

(g) Iterate between (c) and (f) until the end of the solution.

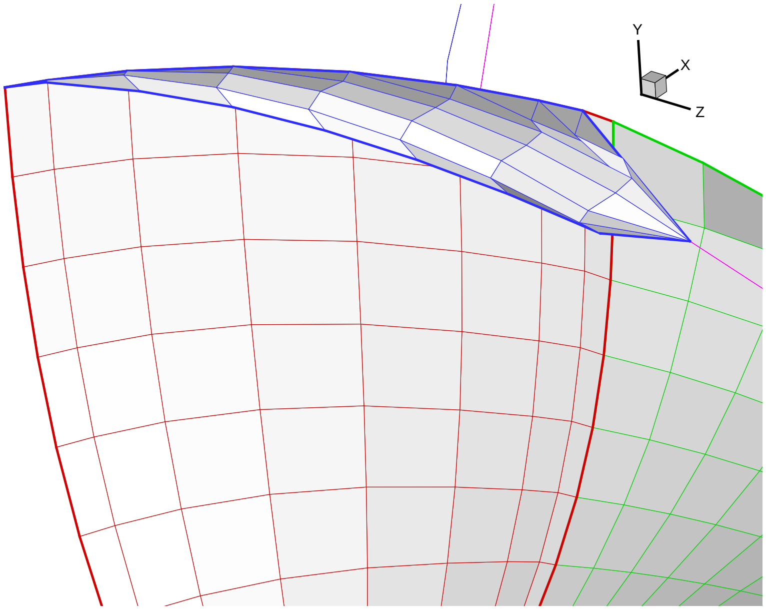

Figure 8.10: Side view of converged geometry of tip leakage vortices for DTMB 3745 propeller, at $J_s = 0.5$.

8.3 Numerical Results

The tip leakage vortex model has the following problems: (a) difficulties in convergence for low advance ratios. (b) possible penetration of the duct wall and transition wake. (c) works only for chordwise panel number $NN < 16$.

8.3.1 Open propeller DTMB 3745

Due to the difficulties in convergence for low advance ratios, open propeller DTMB 3745 with advance ratio of $J_s = 0.5$ is used as the first example. It should be noticed that for such a middle advance ratio, the tip vortex is not physical. However, it is still of value to show the geometry of tip vortex and some characteristics of the model.

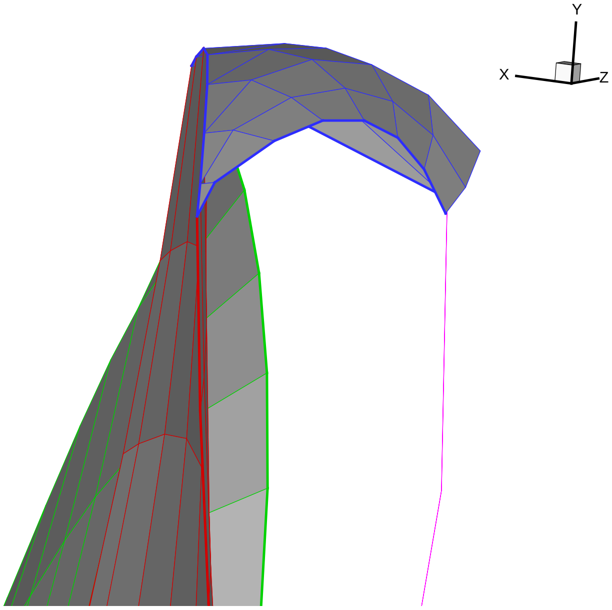

Figure 8.11: Front view of converged geometry of tip leakage vortices for DTMB 3745 propeller, at $J_s = 0.5$.

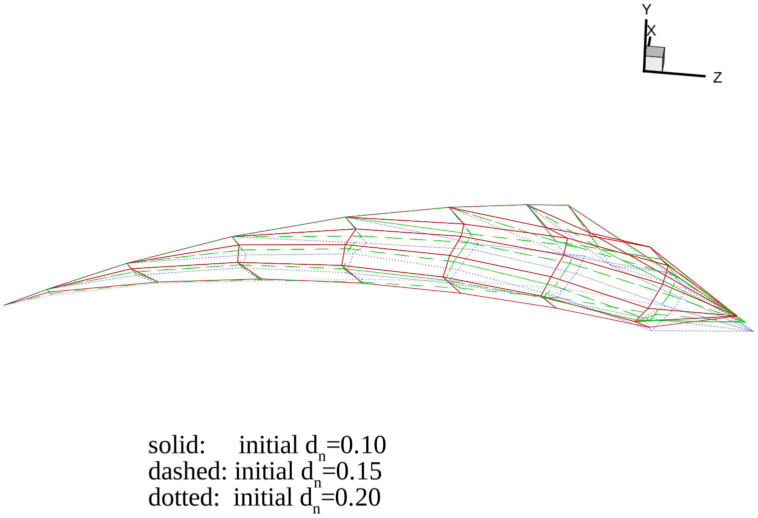

Figure 8.12: Variations in the geometry of tip leakage vortices corresponding to different initial d_ns.

Given the initial parameters $d_n = 0.1$ and $d_r = 0.01$, the converged tip leakage vortex geometry is shown in Figures 8.10 and 8.11. The roll up from the leading edge of the blade is strong, and the final converged geometry is quite smooth. The converged geometry of tip leakage vortices for varying d_n, and the circulation distributions are shown in Figures 8.12 and 8.13 respectively. When comparing Figure 8.13 with Figure 8.9, it can be noticed that the initial guess of d_n does not affect much on the converged geometry.

8.3.2 DTMB 3745 propeller inside a Straight Tunnel

For a ducted propeller, the induced velocities at the tip leakage vertices should include the components from the images due to the duct wall. It is expected that some of the velocities will be canceled in the tip region.

A DTMB 3745 propeller inside a straight tunnel is the second example. The gap percentage is 1%, and the advance ratio is $J_s = 1.1$. The converged geometry of tip leakage vortices is shown in Figure 8.14. Notice that the overview with duct is shown in the top corner, while the tip leakage vortices are magnified without the duct geometry in the main portion of the figure. The velocity cancellation can be observed in this case, and the tip leakage vortices are much weaker compared to the previous open propeller case. Convergence studies were carried out with different numbers of chordwise panels and spanwise panels. Figures 8.15 and 8.16 show the convergences of circulation distributions with varying chordwise and spanwise number of panels, respectively.

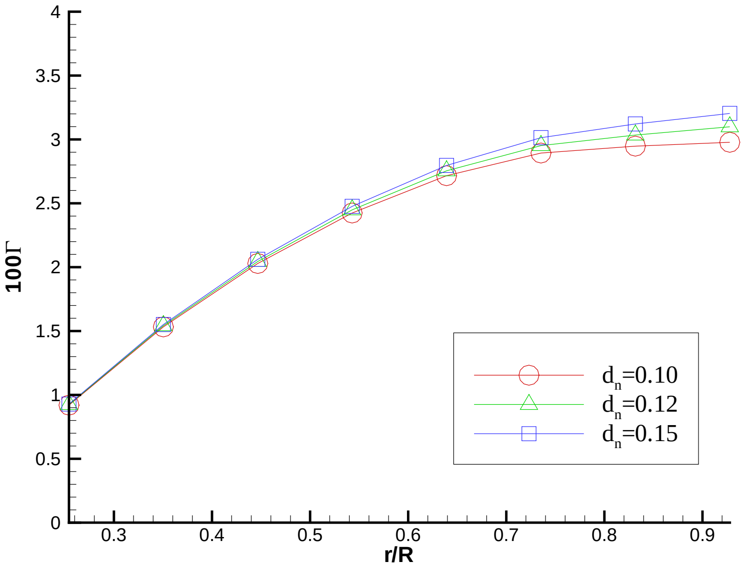

Figure 8.13: Variations in the distribution of circulation, corresponding to different initial d_n.

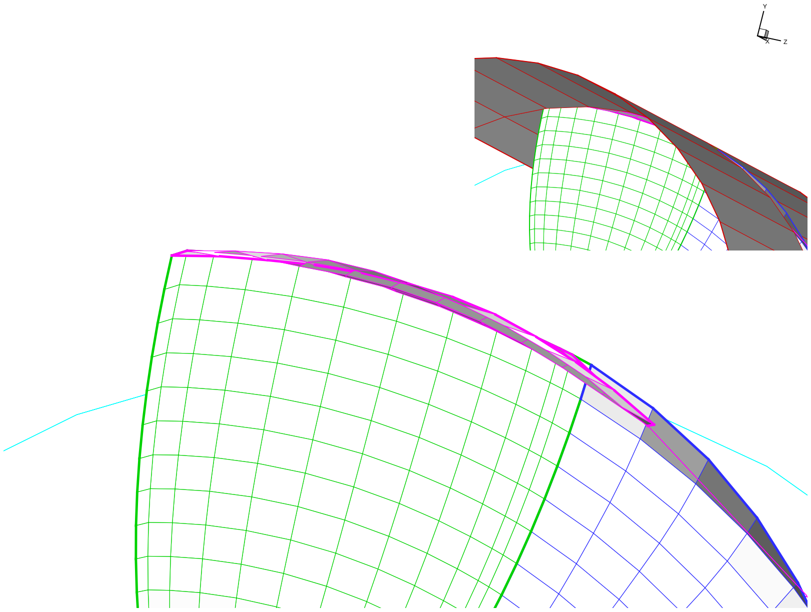

Figure 8.14: Geometry of tip leakage vortices of DTMB 3745 propeller inside a straight tunnel, gap percentage 1%, at $J_s = 1.1$.

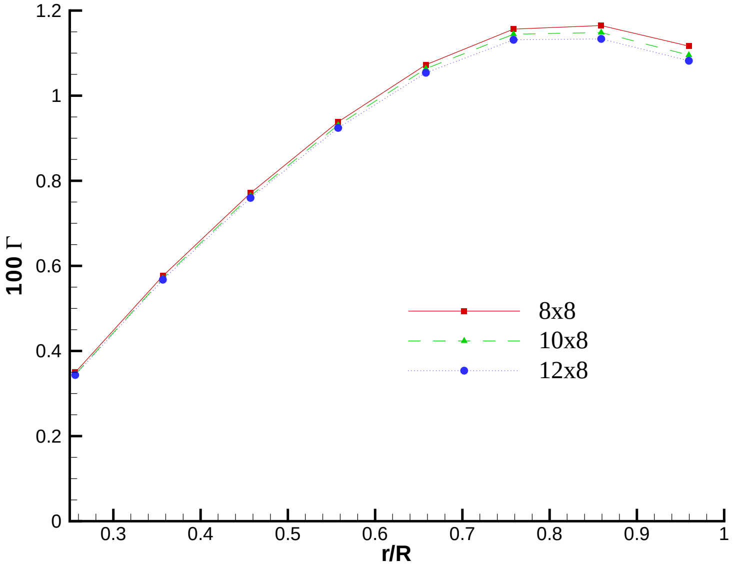

Figure 8.15: Circulation distribution with different spanwise discretizations with fixed spanwise panel numbers

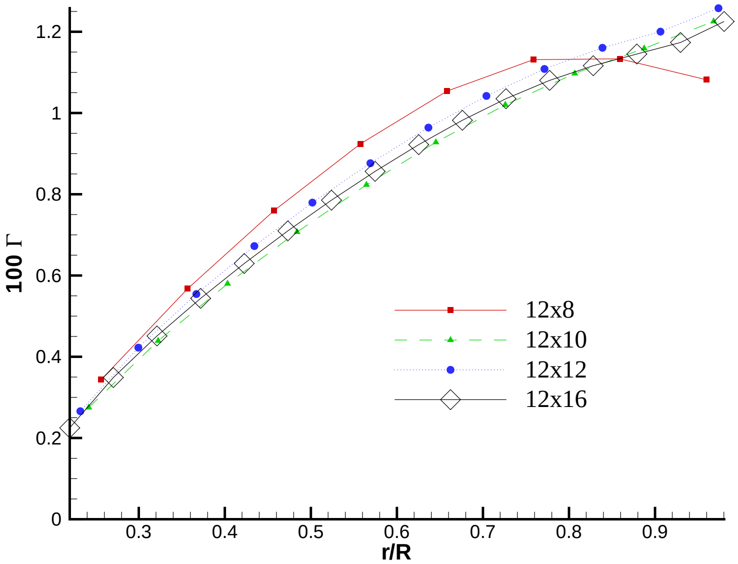

Figure 8.16: Circulation distribution with different spanwise discretizations with fixed chordwise panel numbers

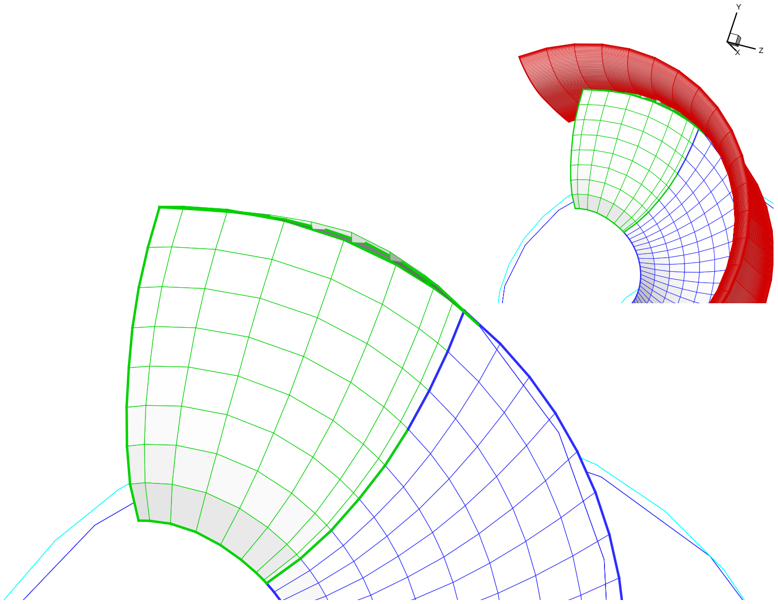

Figure 8.17: Tip leakage vortices at the tip of Ka 4-70 propeller inside nozzle 19A.

8.3.3 Ducted propeller Ka 4-70 inside Nozzle 19A

A Ka 4-70 propeller inside nozzle 19A is used as the third example. The geometries of the duct and propeller are shown in Figure 4.26. Using initial parameters $d_n = 0.1$ and $d_r = 0.01$, the converged tip leakage vortices are shown in Figure 8.17. With different initial parameters d_n, the geometry of initial tip leakage vortices are shown in Figure 8.18. The geometry finally converges, as shown in Figure 8.19 and the circulation distribution also converges, as shown in Figure 8.20.

As a conclusion of this chapter, the comparison of image model, gap model and tip leakage vortex model is shown in Figure 8.21. Both the gap model (with discharge coefficient $C_Q = 0.85$) and the tip leakage vortex model increase the

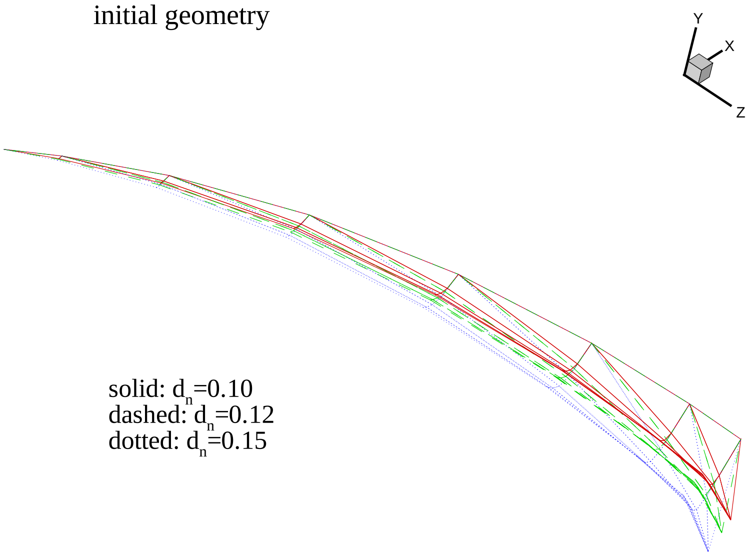

Figure 8.18: Variations in the initial geometries of tip leakage vortices with different initial d_n.

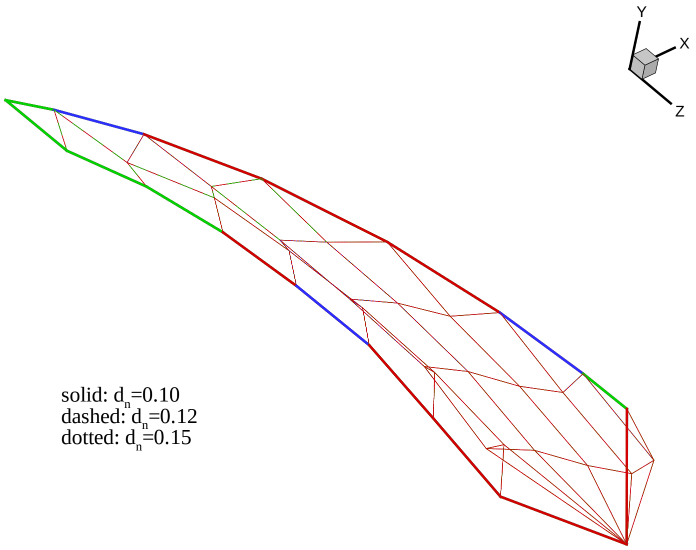

Figure 8.19: Converged geometries of tip leakage vortices with different initial d_n.

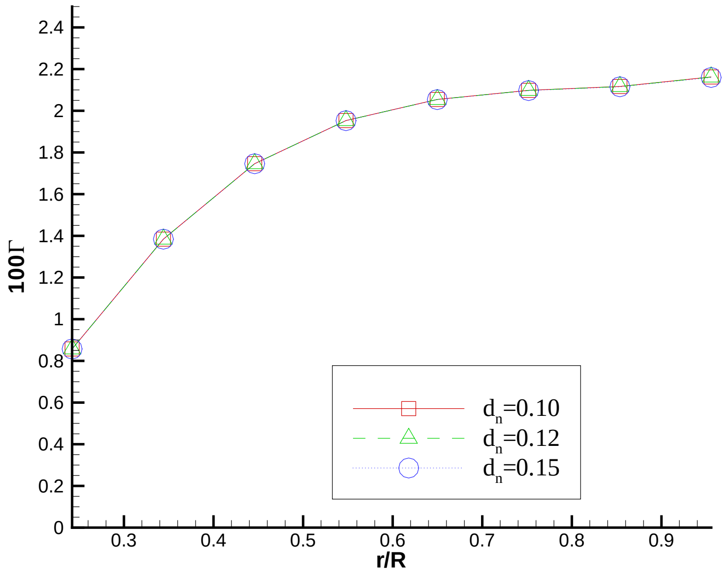

Figure 8.20: Converged circulation for different initial geometries of tip leakage vortices.

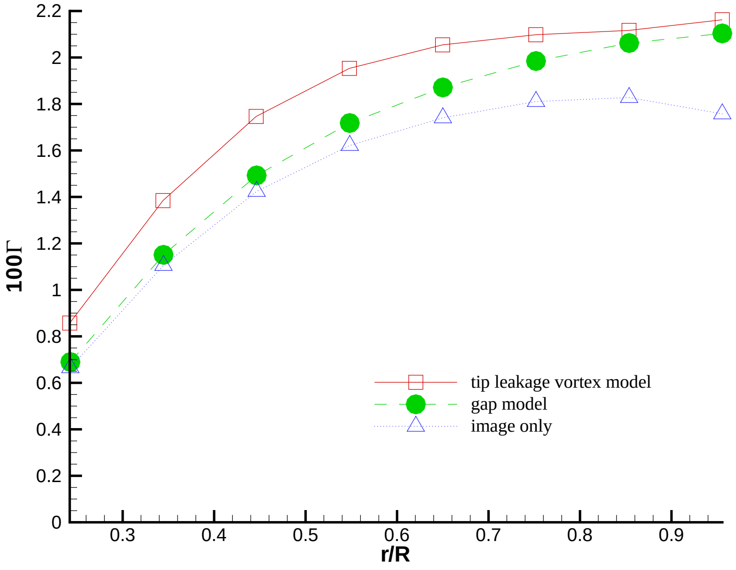

Figure 8.21: Comparison of circulation distribution between image model, gap model and tip leakage vortex model.

loading at the tip. However, tip leakage vortex model affects the circulation from the root to the tip. The combination of tip leakage vortex and gap model still is difficult, since the singularities inside the gap region are very close to each other during the alignment. A judgment on which model is more appropriate is still too early at this stage. As left for the future work, the extensive studies using the viscous solvers such as $FLUENT$ and U^2NCLE may give us better guidance on the numerical modeling of gap flows.

Chapter 9

Conclusions

9.1 Summary

The complexity of marine propulsor has grown with the marine industry's increasing demand for efficiency. Robust, and reliable CFD tools are sought to model the propulsors with complex geometries and flow conditions. The current method is an effort towards meeting this requirement.

In this work, MPUF-3A, a vortex lattice method program, is coupled with GBFLOW, a finite volume based Euler solver, to model the flow in the vicinity of the ducted propeller and predict its hydrodynamic performance. The interaction between the propeller and the surrounding duct is captured by the coupling procedure in an iterative manner.

The iterative procedure is initiated by running MPUF-3A which solves the flow around a propeller subject to nominal inflow. MPUF-3A solves the potential problem in the vicinity of the propeller. Line vortices are distributed on the blade camber surface to represent the velocity jump across the blade. Line sources are distributed on the same surface to represent the thickness effects due to blade and cavity. Kinematic boundary condition, which requires the normal velocities to vanish, is satisfied at the blade control points. The solved line vortices and sources determine the unique potential solution around the propeller. The propeller induced velocities are directly calculated from the prescribed potential field at certain field points. The pressures on the face side and back side are evaluated using the Bernoulli's equation.

The pressure differences across the camber surface are averaged in time, and converted to body forces as input for GBFLOW. For axisymmetric cases, the body forces are also circumferentially averaged. The body forces are interpolated and placed into cells at the propeller plane in GBFLOW grid. The duct is modeled as a solid wall inside the fluid domain. A free slip wall boundary condition is applied on the walls. Euler equations are solved and the total velocity inside the domain is uniquely determined with the following conditions: (a) wall boundary conditions on the duct, (b) body forces at the propeller plane, and (c) nominal velocity distribution on the inflow boundary. The effective velocity, the real velocity that the propeller is subject to, is evaluated by subtracting the induced velocity from the total velocity at certain field points.

The effective velocity is used as the updated inflow for MPUF-3A, and the potential problem around the propeller is solved again. The distributions of line vortices and sources are updated and a new potential solutions are determined. The pressure distributions on both sides of the propeller and the induced velocity distributions at field points are modified. As a result, the body force distributions in GBFLOW are modified and that changes the total flow field prediction. A new effective velocity distribution is determined. This iteration procedure is carried on until the thrust and torque on the propeller converge.

The local flow problem around the propeller and global flow problem in the total fluid field are solved in turn by the iterative procedure discussed above. The interaction between the duct and the propeller is correctly incorporated with the iterative procedure. This iterative procedure is a very general approach which can be easily extended to model the flows around complex propulsor systems such as waterjet, and multi-component ducted propellers.

Besides the general procedure discussed above, some specific treatments for the ducted propellers are implemented in the current method. These specific treatments are the main contribution of the present work.

A general image model is implemented for the non-axisymmetric effects between blades, and accounts for the duct wall effects and hub wall effects. With a nonzero gap, however, the image model cannot correctly predict the finite loading at the tip region. Two approaches are proposed to predict the finite loading at the tip.

- The first approach is the gap model. The gap model has been successfully implemented in the panel method before. However, it is the first application to the vortex lattice method, to the author's knowledge. In this method, the flow rate inside the tip clearance is linked with the pressure difference, as governed by the empirical orifice equation. Additional panels are built inside the small clearance between the duct inner surface and the blade tip, and the orifice equations is satisfied at the control points of the gap panels. The pressure inside the gap is first extrapolated from the blade, and then interpolated at the control points to evaluate the pressure difference. The system of equations is expanded to solve for the strengths of the gap vortices. The gap model improves the thrust predictions on the duct, and predicts well the total thrust of the ducted propeller system. It is a proper way to add the influence of the small gap to the overall prediction of the propeller. However, some doubts exist whether the overall characteristic of the gap can be determined with a simple parameter – the discharge coefficient C_Q. To answer the question, a fully viscous solution is sought inside the gap region of 3D rudder like foils. The assessment of discharge coefficient indicates that a varying C_Q may be a better approach for the gap model.

- In order to avoid the use of the artificially imposed discharge coefficient, the tip leakage vortex is proposed as the second approach. In this method, a separated vortex sheet is implemented as the initial geometry of tip leakage vortices. The induced velocities are evaluated at the tip leakage vertices at each time step, including the image part due to the duct wall. A free wake relaxation scheme is applied to update the location of these vortices during iterations. An iterative process is necessary since the vorticity distribution on the blade affects the aligned geometry of the tip leakage vortices, while the tip leakage vortices, in a dual way, modify the vorticity distribution on the blade. Some convergence and parametric studies are performed and the tip leakage vortex model seems to work well. The tip leakage vortex model does not need any empirical coefficients like C_Q of the gap model. However, it assumes that the tip leakage vortices always start from the leading edge.

> This assumption is a limitation for this model, since the local flow in the gap is needed to determine the accurate location where the vortices start. At this stage, the tip leakage vortex model has not been fully validated. However, it is an alternative way of getting a finite loading at the tip. It is hoped that the planned viscous flow runs on ducted propellers will shed some light as to which, the orifice equation model, the tip leakage vortex model, or a combination of the two methods, would best represent the actual flow.

The flow inside the duct can have a large velocity gradient. To predict the effective velocity accurately, some new approaches are used. The first approach is to evaluate the effective vectors at the blade control points directly. The total velocities in GBFLOW domain are interpolated to get the values at the control points. The induced velocities are also calculated at these points. Finally, the effective velocity vectors are evaluated by subtracting the induced velocities from the total velocities at these control points. At this stage, the error of this approach hinders this method from application to ducted propellers. The second approach is to evaluate the effective velocity at the nearest plane to the blade leading edge. For most cases, this plane is a cell in the front of the blade leading edge, and forms a curved plane due to the shape of the blade leading edge. Besides the effective velocity, an effective pressure is implemented to satisfy the Bernoulli equation in the case of the ducted propellers.

Numerical verification and validation are done for the following cases: bare ducts, wetted ducted propellers, and cavitating ducted propellers. Generally, the current method predicts correctly the total thrust, torque and pressure on the duct, and the circulation distribution, compared to those of inviscid methods. However, discrepancies exist, especially in the case of cavitating propeller performance and cavity shapes, between the current method and other methods and measurements from experiments.

Relative efficiency of the current methods are summarized as below: For 6 to 7 advance ratios, it is estimated to use 10 hours for the curved effective velocity plane method in a single processor, and about 30 hours for the effective vector method. At the other hand, it takes about 48 hours to run RANS for one advance ratio by using multi processor. So the current methods are relative fast and efficient for design and analysis purpose.

9.2 Recommendations for Future Work

The following may be included to improve the current numerical scheme:

- Artificial viscosities are applied to improve the stability of the finite volume method base Euler solver, GBFLOW. For most of applications in Choi [2000], the second order artificial viscosity coefficient, σ_2 is set to zero, and the fourth order artificial viscosity coefficient, σ_4 is selected to have a minimum value. However, for ducted propellers, a higher σ_2 and σ_4 are needed to get convergence. It was found that higher artificial viscosity tends to predict the wrong stagnation points on the duct. A higher artificial viscosity will also introduce over-dissipation. It was found that a nonuniform wake at the inflow plane was dissipated before reaching the propeller plane when high artificial viscosity coefficients were applied. Schemes to reduce the artificial viscosity coefficient in the future should include: (1) use artificial viscosity coefficient only in cells close to duct section; (2) improve the smoothness of the geometry in the grid generation procedure, especially reduce the number of cells with large aspect ratios; (3) modify the Ni's Lax-Wendroff method for pseudo-time discretization.

- More validation studies are needed for induced velocity evaluation at low advance ratios. At present, two methods are implemented to evaluate the induced velocity. A routine, called *PFPP*, evaluates the potential field due to vortices and sources on the blade and wake. The other routine, called *RPAN*, evaluates the potential and velocities in field points due to sources and normal dipoles over quadrilateral panels on blade and wake. The induced velocities predicted from both methods are close to each other, and *RPAN* has better prediction when the field points are close to the singularities. However, errors exist when they are applied to predict the induced velocity at low advance ratios. If this problem is solved, the current overestimation at low advance ratios could be fixed.

- As discussed before, it is appropriate to implement a varying discharge coefficient along the gap. A systematic investigation on the discharge coefficient, based on blade geometries, the gap percentages and the Reynolds numbers, is necessary. The current investigation is just the beginning of such a work.

In the future, with U^2NCLE, it may be possible to validate the gap model in the following steps:

1 Evaluate discharge coefficients inside the gap clearance between propeller tip and duct inner surface in U^2NCLE, in a similar way as done in $FLUENT$.

2 Use the varying discharge coefficients along the gap in the gap model in MPUF-3A.

3 Compare the circulation, the pressure distributions, thrusts and torques between MPUF-3A and U^2NCLE.

- Comparisons between the tip leakage vortex model and U^2NCLE are needed. The geometry of tip leakage vortices, the circulation and the pressure distributions are important indicators showing whether the tip leakage vortex model is appropriate. More investigation is needed for the convergence difficulties when the advance ratio is low. It is also important that the tip leakage vortex model works when the chordwise number of panels exceeds 16. The validation of the tip leakage vortex model will also help us to determine which numerical model, the gap or the tip leakage vortex model, or a combination of the two, is most appropriate.

- More extensive verification and validation studies are required for the current method. Further verification with other methods and validations with measurements from experiments are required. It would be valuable for the prediction of the current methods to be compared with the measurements of ducted propellers subject to non-uniform inflow. However, at this stage, the experiments of ducted propellers in non-uniform inflows and unsteady force measurements are not available.

- Extension of the current method for modeling of waterjets and multi-component ducted propellers. For waterjets, the current method is more appropriate to study the part of the tunnel where the impellers are located. For multi-component ducted propeller, the interactions between each component and/or between component and duct wall are needed. This problem can be easily treated as an iteration between two MPUF-3A runs for both components and a GBFLOW run for the whole flow domain.

Appendix

Appendix A

Grid Generation

In order to solve the governing Euler equation, a finite volume method (FVM) is applied, as detailed in Chapter 3.4. The computational domain are coincident with the physical domain in the FVM, while the grid generation of FVM still can follow the way that grids are prepared for the partial difference method

The type of the grid generator needs to be of the same form as the governing equation, as discussed by Hoffman [1989]. Due to potential flow property of Euler equations, an elliptic generator is used to create the grids.

As in 2-D, a set of body-fitted coordinate system with ξ and η coordinate lines is created. ξ lines are aligned with the surface along the streamwise direction, and the η lines are normal to the surface. The relations between the physical and computational spaces are:

$$\xi = \xi(x, y) \tag{A.1}$$

$$\eta = \eta(x, y) \tag{A.2}$$

A system of elliptic equations in the forms of a Laplace equation is solved for the coordinates of grid points in the physical domain, as

$$\xi_{xx} + \xi_{yy} = 0 \tag{A.3}$$

$$\eta_{xx} + \eta_{yy} = 0 \tag{A.4}$$

The system of elliptic equations (A.3 and A.4) can be solved by partial difference method, see Hoffman [1989] for details. The grid point locations in the physical space (x, y) are provided by the solutions of (ξ, η) in computational domain.

When the duct is placed inside the fluid domain, as in Figure 3.14, the region is not reducible any more. Such a domain is classified as a doubly-connected domain. A branch cut, line AC, is introduced to render the doubly-connected region to a simply-connected domain, as shown in Figure A.1. B1 is the duct section, B2 is the outer boundary. B3 and B4 are surfaces created after the cut.

The doubly-connected region is unwrapped by the cut and a simply-connected region is created, as shown in Figure A.2

The computational domain is then stretched and deformed to create a rectangular domain, as shown in Figure A.3.

The final grid topology for the duct is shown in Figure A.4. The cut is named as “repeat boundary”. The ξ coordinate lines surround the duct section in a counter-clockwise manner, and η lines point towards the duct from the outer boundaries.

A 3D grid can be created by rotating along the bottom boundary of the 2D grid in the tangential ζ direction, as shown in Figure A.5.

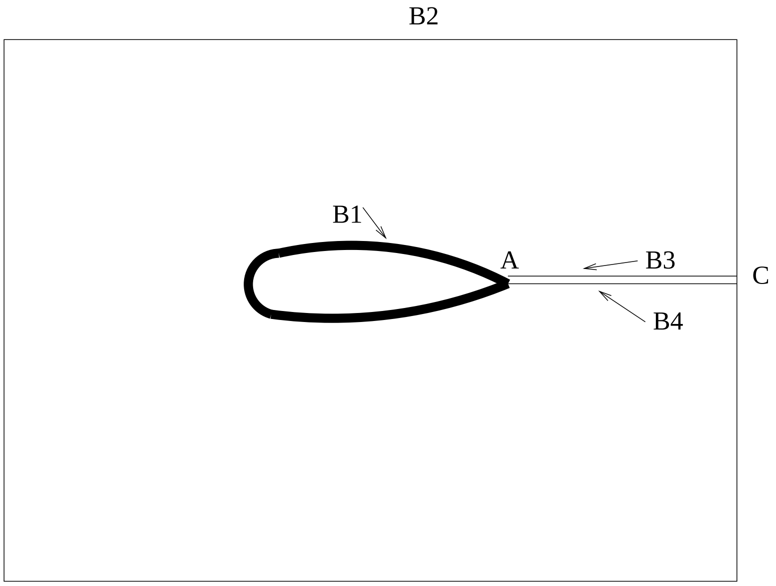

Figure A.1: A cut is introduced to make the domain simply-connected. Adopted from Hoffman [1989]

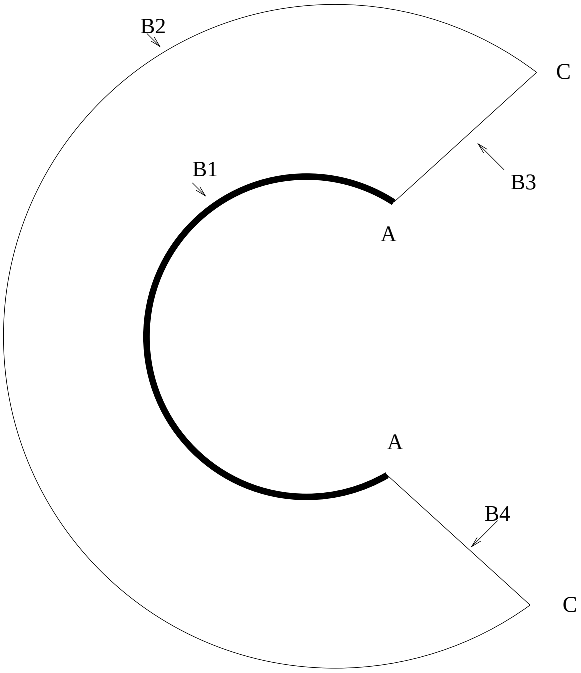

Figure A.2: Unwrapping the doubly connected region. Adopted from Hoffman [1989]

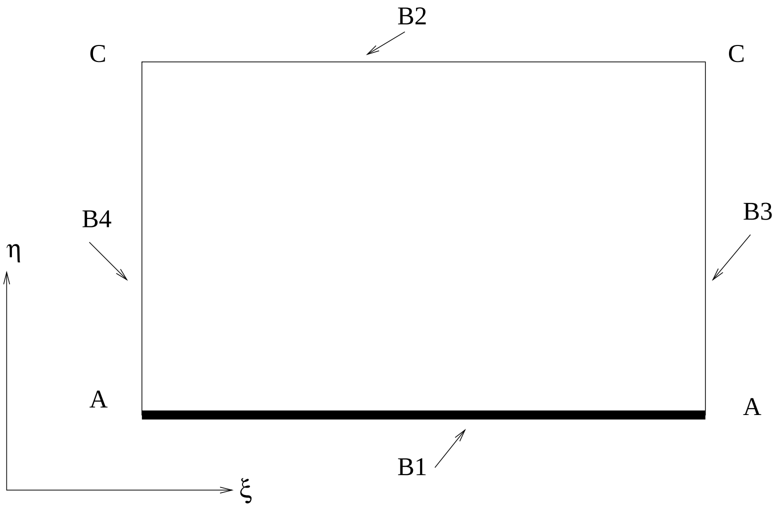

Figure A.3: A rectangular domain after deformation. Adopted from Hoffman [1989]

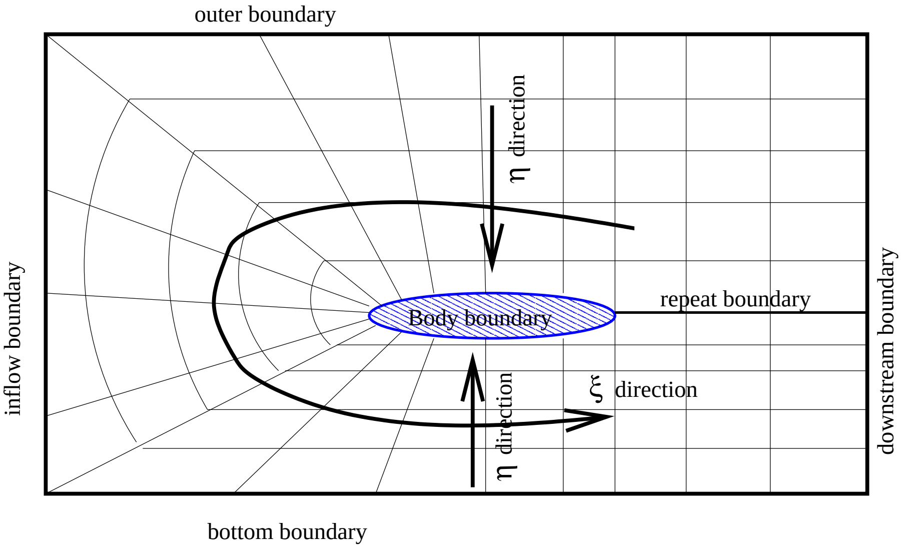

Figure A.4: Topology of 2D grid for duct.

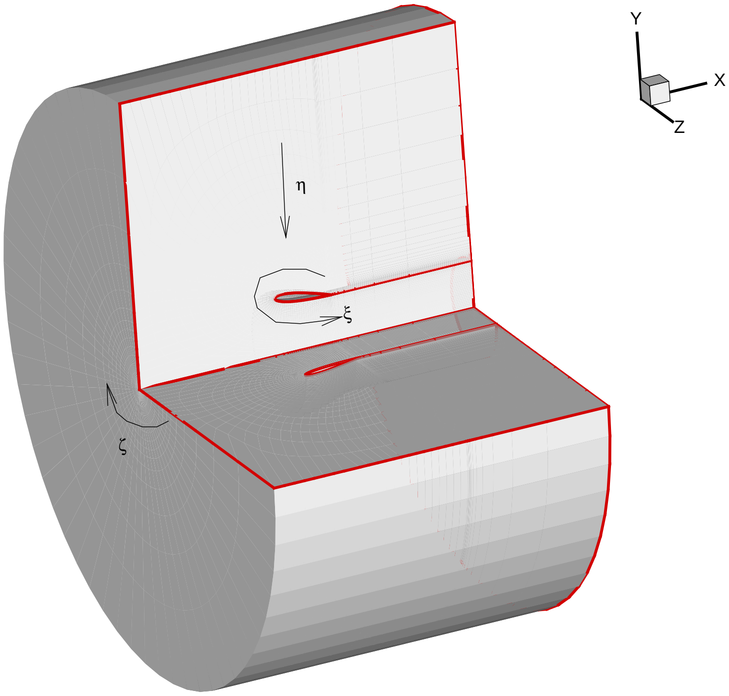

Figure A.5: Topology of 3D grid for duct.

Bibliography

Abdel-Maksoud, M. and Heinke, H. J. (2002). Scale effects on ducted propellers. In *Twenty-Fourth Symposium on Naval Hydrodynamics*, Fukuoka, Japan.

Breslin, J. P., Van Houten, R. J., Kerwin, J. E., and Johnsson, C.-A. (1982). Theoretical and experimental propeller-induced hull pressures arising from intermittent blade cavitation, loading, and thickness. *Trans. of Society of Naval Architects & Marine Engineers*, 90:111–151.

Brewer, W. H. (2002). *On simulating Tip-Leakage Vortex Flow to Study the Nature of Cavitation Inception*. PhD thesis, The Mississippi State University.

Brewer, W. H., Newman, J. C., Burgreen, G. W., and Burg, C. O. E. (2003). A design method for investigating cavitation delay. In *The 8th International Conference on Numerical Ship Hydrodynamics*, Busan, Korea.

Brockett, T. E. (1999). Interaction of ducted propulsor and stern for an axisymmetric hull. *International Shipbuilding Progress*, vol 46(445):pp. 61–89.

Carlton, J. S. (1994). *Marine Propellers and Propulsion*. Butterworth Heinemann, 1st edition.

Chen, B. and Stern, F. (1999). Computational fluid dynamics of four-quadrant marine-propulsor flow. *Journal of Ship Research*, vol 43(4):pp.218–228.

Chen, B., Stern, F., and Kim, W. (1994). Computation of unsteady viscous marine propulsor blade and wake flow. In *Twentieth Symposium on Naval Hydrodynamics*, University of California, Santa Barbara.

Chesnakas, C. and Jessup, S. D. (2003). Tip-vortex induced cavitation on a ducted propulsor. In *International Symposium on Cavitation Inception*, Honolulu. American Society of Mechanical Engineering (ASME) Fluid Engineering Division (FED) Summer Meeting.

Choi, J.-K. (2000). *Vortical Inflow – Propeller Interaction Using Unsteady Three-Dimensional Euler Solver*. PhD thesis, Department of Civil Engineering, The University of Texas at Austin.

Choi, J.-K. and Kinnas, S. (2001a). Prediction of non-axisymmetric effective wake by a three-dimensional eular solver. *Journal of Ship Research*, 45(1):pp.13–33.

Choi, J.-K. and Kinnas, S. A. (1998). A 3-D Euler solver and its application on the analysis of cavitating propellers. In *Proceedings of the 25th ATTC*, Iowa City, Iowa. American Towing Tank Conference.

Choi, J.-K. and Kinnas, S. A. (2000a). Non-axisymmetric effective wake prediction by using an unsteady three-dimensional Euler solver. In *Propellers/Shafting ’00 Symposium*, Virginia Beach, Virginia. Society of Naval Architecture & Marine Engineering.

Choi, J.-K. and Kinnas, S. A. (2000b). An unsteady 3-D Euler solver coupled with a cavitating propeller analysis method. In *23rd Symposium on Naval Hydrodynamics*, Val de Reuil, France.

Choi, J.-K. and Kinnas, S. A. (2001b). Prediction of non-axisymmetric effective wake by a three-dimensional eular solver. *Journal of Ship Research*, 45(1):pp.13–33.

Choi, J.-K. and Kinnas, S. A. (2003). Prediction of unsteady effective wake by a euler solver/vortex-lattice coupled method. *Journal of Ship Research*, 47(2):pp. 131–144.

Chorin, A. J. (1967). A numerical method for solving incompressible viscous flow problems. *Journal of Computational Physics*, 2:pp.12–26.

Courant, R., Friedrichs, K., and Lewy, H. (1967). On the partial difference equations of mathematical physics. *IBM Journal*, 11:pp. 215–234.

Dyne, G. (1973). Systematic studies of accelerating ducted propellers in axial and incline flows. In *Proceedings of the Symposium on Ducted Propellers*, Teddington, England. Royal Institute of Naval Architects.

Falcão de Campos, J. (1983). On the calculation of ducted propeller performance in axisymmetric flows. Technical Report 696, Netherlands Ship Model Basin, Wageningen, The Netherlands.

Farrel, K. J. (1989). An investigation of end-wall vortex cavitation in a high reynolds number axial-flow pump. Master's thesis, The Pennsylvania State University.

Gearhart, W. S. (1964). Tip clearance flow in turbomachines. Master's thesis, The Pennsylvania State University.

Gibson, I. S. and Lewis, R. I. (1973). Ducted propeller analysis by surface vorticity and actuator disk theory. In *Proceedings of the Symposium on Ducted Propellers*, Teddington, England. Royal Institute of Naval Architects.

Glover, E. J. and Ryan, P. G. (1973). A comparison of the theoretical and experimental performance of a ducted propeller system. In *Proceedings of the Symposium on Ducted Propellers*, Teddington, England. The Royal Institution of Naval Architects.

Greeley, D. S. (1982). *Marine Propeller Blade Tip Flow*. PhD thesis, Department of Ocean Engineering, Massachusetts Institute of Technology.

Greeley, D. S. and Kerwin, J. E. (1982). Numerical methods for propeller design and analysis in steady flow. *Trans. of Society of Naval Architects & Marine Engineers*, 90:415–453.

Hoffman, K. (1989). *Computational Fluid Dynamics for Engineers*. Engineering Education System, 1st edition.

Hsiao, C.-T. and Chahine, G. L. (2004). Numerical study of cavitation inception due to vortex/vortex interaction in a ducted propulsor. In *The 25th Symposium on Naval Hydrodynamics*, St. John's, Newfoundland and Labrador, Canada.

Huang, T.-T. and Groves, N. C. (1980). Effective wake : Theory and experiment. In *13th Symposium on Naval Hydrodynamics*, Tokyo, Japan.

Hughes, M. (1993). *Analysis of Multi-component Ducted Propulsors in Unsteady Flow*. PhD thesis, Department of Ocean Engineering, Massachusetts Institute of Technology.

Hughes, M. J. (1997). Impementation of a special procedure for modeling the tip clearance flow in a panel method for ducted propulsors. In *Propellers/Shafting '97 Symposium*, Virginia Beach, Virginia.

Hughes, M. J. and Kinnas, S. A. (1993). Unsteady flows around multi-component integrated propulsors. In *Forum on Unsteady Flows, Fluid Engineering Division (FED) vol. 157*. American Society of Mechanical Engineering (ASME).

Hughes, M. J., Kinnas, S. A., and Kerwin, J. E. (1992). Experimental validation of a ducted propeller analysis method. *Journal of Fluids Engineering*, 114(2):pp. 214–219.

Kerwin, J. E., Keenan, D. P., Black, S. D., and Diggs, J. G. (1994). A coupled viscous/potential flow design method for wake adapted multi-stage, ducted propulsors using generalized geometry. *Trans. of Society of Naval Architecture & Marine Engineering*, 102.

Kerwin, J. E., Kinnas, S. A., Lee, J.-T., and Shih, W.-Z. (1987). A surface panel method for the hydrodynamic analysis of ducted propellers. *Trans. of Society of Naval Architecture & Marine Engineering*, 95.

Kerwin, J. E. and Lee, C.-S. (1978). Prediction of steady and unsteady marine propeller performance by numerical lifting-surface theory. *Trans. of Society of Naval Architecture & Marine Engineering*, 86.

Kerwin, J. E., Taylor, T. E., Black, S. D., and McHugh, G. P. (1997). A coupled lifting-surface analysis technique for marine propulsors in steady flow. In *Propellers/Shafting '97 Symposium*, Virginia Beach, Virginia. Society of Naval Architecture & Marine Engineering.

Kinnas, S. A. (1991). Leading-edge corrections to the linear theory of partially cavitating hydrofoils. *Journal of Ship Research*, 35(1):pp. 15–27.

Kinnas, S. A. (1992). A general theory for the coupling between thickness and loading for wings and propellers. *Journal of Ship Research*, 36(1):59–68.

Kinnas, S. A. (2006). A note on bernoulli equation for propeller flows: The effective pressure. *Journal of Ship Research*, 43(1):accepted.

Kinnas, S. A. ((editor) 1999). University/Navy/Industry Consortium on Cavitation Performance of High Speed Propulsors - Presentations and Progress Reports - 11th Steering Committee Meeting. Department. of Civil Engineering, University of Texas at Austin.

Kinnas, S. A., Choi, J.-K., Kakar, K., and Gu, H. (2001). A general computational technique for the prediction of cavitation on two-stage propulsors. In *The 26th American Towing Tank Conference*, Glen Cove, NY.

Kinnas, S. A., Choi, J.-K., Lee, H. S., and Young, Y. L. (2000). Numerical cavitation tunnel. In *NCT50, International Conference on Propeller Cavitation*, pages 137–157, Newcastle upon Tyne, England.

Kinnas, S. A., Choi, J.-K., Lee, H. S., Young, Y. L., Gu, H., Kakar, K., and Natarajan, S. (2002). Prediction of cavitation performance of single/multi-component propulsors and their interaction with the hull. *Trans. of Society of Naval Architects & Marine Engineers*.

Kinnas, S. A. and Coney, W. B. (1992). The generalized image model - an application to the design of ducted propellers. *Journal of Ship Research*, 36(3):197–209.

Kinnas, S. A. and Fine, N. E. (1989). Theoretical prediction of the midchord and face unsteady propeller sheet cavitation. In *Fifth International Conference on Numerical Ship Hydrodynamics*, Hiroshima, Japan.

Kinnas, S. A., Griffin, P. E., Choi, J.-K., and Kosal, E. M. (1998). Automated design of propulsor blades for high-speed ocean vehicle applications. *Trans. of Society of Naval Architects & Marine Engineers*, 106:213–240.

Kinnas, S. A. and Pyo, S. (1999). Cavitating propeller analysis including the effects of wake alignment. *Journal of Ship Research*, 43(1):38–47.

Kudo, T. and Kinnas, S. A. (1995). Application of unsteady vortex/source lattice method on supercavitating propellers. In *24th American Towing Tank Conference*, pages 33–40, College Station, Texas.

Lee, C. (1979). *Prediction of Steady and Unsteady Performance of Marine Propellers with or without Cavitation by Numerical Lifting Surface Theory*. PhD thesis, Department of Ocean Engineering, Massachusetts Institute of Technology.

Lee, H. S. (2002). *Modeling of Unsteady Wake Alignment and Developed Tip Vortex Cavitation*. PhD thesis, Department of Civil Engineering, The University of Texas at Austin.

Lee, H. S. and Kinnas, S. A. (2006). Prediction of cavitating performance of ducted propeller. In *CAV2006: Sixth International Symposium on Cavitation*, Wageningen, The Netherlands.

Lee, Y.-T., Feng, J., Merkle, C., and Tse, M. (1998). Effects of tip-clearance flows. In *Twenty-Second Symposium on Naval Hydrodynamics*, Washington DC.

Manen, J. D. (1966). The choice of the propeller. In *Marine Technology*.

Moon, I.-S., Kim, K.-S., and Lee, C.-S. (2002). Blade tip gap flow model for performance analysis of waterjet propulsors. In *International Association for Boundary Element Methods*, Austin, Texas.

Morgan, W. and Caster, E. (1965). Prediction of the aerodtnamics characteristics of annular airfoils. Technical Report Report 1830, David Taylor Model Basin.

Natarajan, S. (2003). Computational modeling of rudder cavitation and propeller/rudder interaction. Master's thesis, Department of Civil Engineering, The University of Texas at Austin.

Ni, R.-H. (1982). A multiple-grid scheme for solving the Euler equations. *AIAA Journal*, 20(11):pp.1565–1571.

Oosterveld, W. C. (1970). Wake adapted ducted propellers. Technical Report No. 345, Netherlands Ship Model Basin, Wageningen, Netherlands.

Sanchez-Caja, A., Rautaheimo, P., and Siikonen, T. (2000). Simulation of incompressible viscous flow around a ducted propeller using a rans equation solver. In *Twenty-Third Symposium on Naval Hydrodynamics*, Valde Reuil, France.

Shepard, D. (1968). A two dimensional interpolation function for irregularly spaced data. In *Proceedings of 23 rd National Conference of ACM*, New York. Assocation for Computing Mechinery (ACM).

Shih, W. Z. (1988). *A Combined Euler Equation/Surface Panel Solution to the shear Interaction Problem of An Open or Ducted Propeller*. PhD thesis, Department of Ocean Engineering, Massachusetts Institute of Technology.

Srivastava, R. (1996). Time-marching euler analysis of ducted-propellers. *Journal of Propulsion and Power*, 12(1):pp. 134–138.

Stanier, M. J. (1998). The application of RANS code to investigate propeller scale effects. In *22nd Symposium on Naval Hydrodynamics*, Washington, D.C.

Stern, F., Kim, H.-T., Patel, V. C., and Chen, H.-C. (1988a). Computation of viscous flow around propeller-shaft configurations. *Journal of Ship Research*, 32(4):pp.263–284.

Stern, F., Kim, H.-T., Patel, V. C., and Chen, H.-C. (1988b). A viscous-flow approach to the computation of propeller- hull interaction. *Journal of Ship Research*, 32(4):pp. 246–262.

Stern, F., Zhang, D., Chen, B., Kim, H., and Jessup, S. (1994). Computation of viscous marine propulsor blade and wake flow. In *Twentieth Symposium on Naval Hydrodynamics*, Santa Barbara, California.

Van Houten, R. (1986). Analysis of ducted propellers in steady flow. Technical Report 4.76-1, Airflow Research and Manufacturing Corp., Watertown, Massachusetts.

Warren, C. L., Taylor, T. E., and Kerwin, J. E. (2000). A coupled viscous/potential-flow method for the prediction of propulsor-induced maneuvering forces. In *Propellers/Shafting ’00 Symposium*, Virginia Beach, Virginia. Society of Naval Architecture & Marine Engineering.

Weems, K. M. and Korpus, R. A. (1993). A RANS based propeller/hull interaction analysis system. Technical Report SAIC-93/1068, Science Applications International Corporations.

White, F. (1986). *Fluid Mechanics*. Mcgraw-Hill Book Company, 2nd edition.

VITA

Hua Gu was born in Nantong city, Jiangsu Province, China on February 18, 1975, the son of Jinlin Gu and Jifang Yuan. He graduated from the First High School, Nantong in June 1993 and subsequently entered the Department of Naval Architecture and Ocean Engineering at Huazhong University of Science and Technology, Wuhan, Hubei. After he received his Bachelor of Science degree in Naval Architecture in June 1997, he entered the graduate school in September 1997 to continue his study in Shipbuilding and Design and received a Master of Science degree in June 2000. He started his doctoral program in the ocean engineering group, Department of Civil, Environmental, and Architecture Engineering at the University of Texas at Austin in September, 2000.

Permanent address: No 152, 7th Group, Zhangsheng Cottage
Rengang Street, Nantong, Jiangsu
People's Republic of China

This dissertation was typeset with LaTeX[†] by the author.

[†] LaTeX is a document preparation system developed by Leslie Lamport as a special version of Donald Knuth's TeX Program.